Investigations of A=34 Nuclei Through Fusion Evaporation Using the GALILEO Spectrometer

by

Isaiah Aditya Djianto

B.Sc., University of Waterloo, 2017

Thesis Submitted in Partial Fulfillment of the
Requirements for the Degree of
Master of Science

in the
Department of Chemistry
Faculty of Science

SIMON FRASER UNIVERSITY
Fall 2021

Declaration of Committee

Name: **Isaiah Aditya Djianto**

Degree: **Master of Science**

Thesis title: **Investigations of A=34 Nuclei Through Fusion Evaporation Using the GALILEO Spectrometer**

Committee: **Chair:** Hogan Yu
Professor, Chemistry

Corina Andreoiu
Supervisor
Professor, Chemistry

Gary Leach
Committee Member
Associate Professor, Chemistry

Greg Hackman
Committee Member
Research Scientist
TRIUMF

Loren Kaake
Examiner
Associate Professor, Chemistry

Abstract

The nuclear shell model has accurately predicted many experimental trends in the atomic mass region of A=20-60 and beyond. One way to examine this model is by studying mirror nuclei–which have exchanged numbers of protons and neutrons. Differences between the analogue nuclear energy levels and their decay patterns in mirror nuclei are key in quantifying isospin symmetry in the nuclear force. Of particular interest is studying the neutron deficient ^{34}Ar and compare its structure to its mirror nucleus ^{34}S. Whilst ^{34}S has been extensively studied, ^{34}Ar has only been studied at comparatively low energies. In addition, shell model calculations of mirror energies for A=34 Ar-Cl-S seem to disagree with available experimental data.

A fusion evaporation experiment was conducted at the Laboratori Nazionali Legnaro (LNL – INFN) in 2015 using a ^{12}C beam to bombard a stationary ^{24}Mg target. The intent was to observe ^{34}Ar in high spin states by observing the 2 neutron channel. Other stronger channels were opened in this reaction which produce a high background, making observing the ^{34}Ar spectrum difficult. Gamma rays were detected by the GALILEO array composed of 25 High Purity Germanium (HPGe) detectors. The EUCLIDES charged particle detector associates charged particles being evaporated, whilst the neutron wall array tagged neutrons. Coincident events between the charged particles, neutrons, and gamma rays are used to create spectra of specific nuclei.

The 2*p* reaction channel, associated with ^{34}S, and *pn* reaction channel, associated with ^{34}Cl, are analyzed and verified against known transitions in both nuclei. Contamination from other reaction channels complicated the analysis, as transitions from competing channels often overlapped. The ^{34}Ar nucleus was not found in sufficient quantities to be detected, with the experimental reaction cross section calculated to be less than 91 μb.

Keywords: Fusion Evaporation; Gamma-ray Spectroscopy

Dedication

A Haiku:

Target and a beam

Fusion Evaporation

Where is my argon

Acknowledgements

thank you to Sydney and my family for understanding

⋮

minimalism aside i would formally like to thank a list of people and bring closure to my time. this will be pretentious.

Supervisor

Corina Andreoiu	Simon Fraser University

thank you for guiding me from start to finish. there's nothing i can say that will fully encapsulate the amount of help i've received. i often got in trouble for not looking like i was doing this project on my own, and that is very much true: thanks for keeping the forward momentum of this project going throughout the many stumbling blocks.

Committee

Greg Hackman	TRIUMF
Gary Leach	Simon Fraser University

thank you to my committee for constantly setting a trajectory for me. thanks for keeping me honest. thanks for helping me stay in touch with what was important about the project. lastly, it might seem disingenuous, but i honestly thank you for suggesting i take a quantum mechanics course, it really is something i enjoy, and it was a dream to reconnect with the basics.

Experiment

Fatima H. Garcia	Simon Fraser University	Barbara Melon	INFN Firenze
Jennifer L. Pore		Adriana Nannini	
Pietro Spagnoletti		Marco Rocchini	
Dino Bazzacco	LNL INFN	Giovanna Benzoni	INFN Milano
Alain Goasduff		Beyhan Bastin	GANIL
Kasia Hadynska-Klek		Francois de Oliviera	
Grześ Jaworski		Yannen Jaganathen	
Daniel Napoli		Andres Gadea	Instituto de Física Corpuscular
Marco Siciliano			
Dmitry Testov		Jurek Grebosz	IFJ PAN
Jose Javier Valiente-Dobòn		Roby Austin	Saint Mary's University
Alberto Boso	INFN Padova	Costel Petrache	Université Paris-Saclay
Philipp Rudolf John		Eda Sahin	Universitetet i Oslo
Silvia Lenzi			
Roberto Menegazzo			
Daniele Mengoni			
Francesco Recchia			

thank you. this is for everyone who contributed a line of code, sat on shift, or otherwise contributed amply to the analysis in one way or another. thanks in particular to alain and pietro for being the round-the-clock tech support for everything legnaro related. thanks to fatima, jen, and corina for representing `sfu` during the experiment.

Office

Jonathan Williams	TRIUMF
Kevin Ortner	Simon Fraser University
Frank Wu	
Melanie Gascoine	-
Kurtis Raymond	
Kenneth Whitmore	

thanks for helping me develop my ideas, there really is no breakthrough without having someone stare at you while you say stupid stuff. also thanks for responding to my emails even after leaving `sfu`. obviously some overlap with some people credited before (e.g. fatima “baker in chief” garcia). shoutout to kris, who I only ever meet in the washroom in the last year i was there.

as i wind down, thanks to all my old friends and new friends, those who played games with me when i was trying to avoid work and those who i met at work. thank you for coming out to my defence in what could only be described in my subjective eyes as “record numbers”.

thanks to corina for inspiring me to turn this section from a blank empty page into a self-indulgent rant.

and for symmetry and sincerity:

⋮

thank you to my family and Sydney for understanding

Table of Contents

List of Tables

List of Figures

Chapter 1

Introduction

Nuclei are one of the most fundamental building blocks in our universe: as chemists, we describe every compound and atom based on the nuclei that form our molecules. As such, understanding what nuclei are made of and how they behave are paramount. The design of experiments probing an atomic nucleus is made complicated by the strength of the nuclear force binding the protons and neutrons together. Yet because the nucleus is bound by the nuclear force, studying nuclei is one of the most common and bountiful ways to try and understand the aforementioned nuclear force. It is thus vitally important to study atomic nuclei and their behaviour to explore one of the driving forces of our universe.

From a chemistry perspective, the atom is usually discussed from the context of the behaviour of its electrons. However, the atomic nucleus found at the core of the atom contains the bulk of its mass, and poses its own interesting set of questions [3]. A depiction of a deuterium atom - not to scale - is shown in Figure 1.1, where it should be noted that the nuclear radius is actually five orders of magnitude smaller than the atomic radius.

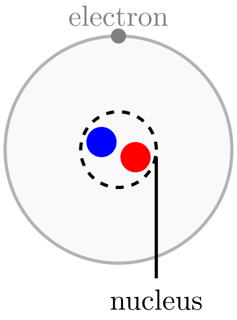

Figure 1.1: Schematic of a deuterium atom, whose nucleus is composed of a proton and neutron. This sketch is not to scale and serves only as an illustration.

Describing the nucleus requires theoretical context for what is being observed in experiment, and we will discuss the nucleus through the shell model for this work.

Our current description of the nucleus starts from its composition of protons and neutrons. If we ignore the proton's charge, both these particles are nearly identical in mass and may be conveniently described as two states of the same particle: the nucleon. We can observe a nucleus, so it must be a bound state. With this in mind we may say that there is a nuclear force that serves to bind the nucleons together, counteracting the repulsive electric force from the positively charged protons. Our treatment of the nuclear force assumes that it acts equally on protons and neutrons, which we call charge independence. The otherwise equal nucleons are differentiated by what we call the isospin projections: $t_3 = 1/2$ for the neutron and $t_3 = -1/2$ for the proton. Note that this is a similar case to treating spin up and spin down electrons, hence the term "isospin". Because of this charge independence, the structure and energies associated with forming a nucleus should only be dependent on the total number of nucleons; a nucleus of Z protons and N neutrons and its "mirror nucleus" of N protons and Z neutrons should be identical in structure and energies. However, it is also important to consider the electrical Coulomb force that exists between protons.

This symmetry is reflected in the chart of nuclides shown in Figure 1.2, where the red N = Z line of equal proton and neutron numbers follow the stable nuclides up until around an atomic mass of 40. Beyond this point, the addition of more protons increases the strength of the Coulomb force, and more neutrons are required to spatially isolate the positive charges, and the nuclei tend towards higher neutron numbers compared to proton numbers.

It is here we note that the mathematical treatment of nuclei and atoms are very similar in principle. That is to say, you can get an energy spectrum from a nucleus' orbitals just like an atom's orbitals. Thus, we can compare the different spectra (which are called level schemes) of mirror nuclei and observe if they are indeed identical or not. Practically speaking, we see mirror nuclei where the level schemes are similar to a good degree as well as mirror nuclei with different level schemes between the species. Describing why the level schemes are similar or not helps us understand how nuclei work and their underlying structure.

In this specific case, studying one pair of mirror nuclei ^{34}Ar and ^{34}S serves a unique challenge; although ^{34}S is extensively studied to high angular momentum states, the neutron deficient ^{34}Ar has barely been studied beyond several of its low lying states. This led to an experiment conducted in 2015 at the Laboratori Nazionali di Legnaro in Legnaro, Italy to probe high angular momentum states in ^{34}Ar using γ-ray spectroscopy.

This work will start by examining the shell model for nuclei in Chapter 1, before discussing the underlying mechanisms underpinning the fusion evaporation experiment conducted in Chapter 2. Chapter 3 will explore previous work done in the mass region $A = 34$ around the $N = Z$ line to compare the setup and equipment with what was used in the present work. Chapter 4 will explore the experimental setup used to produce and observe ^{34}Ar,

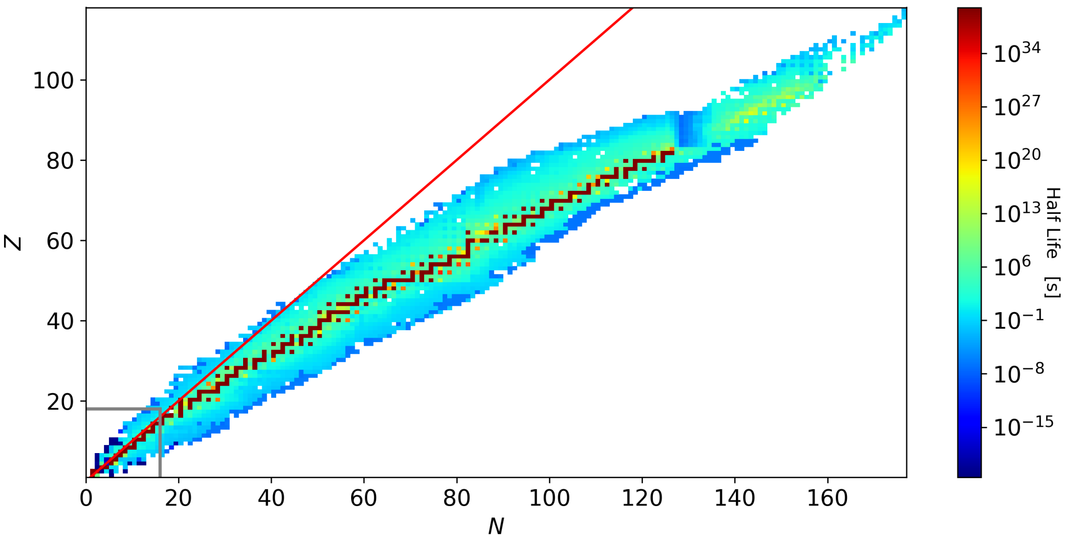

Figure 1.2: The chart of nuclides with the half lives of each nucleus shown. The N = Z line is shown in red to reflect equal proton and neutron numbers, and the tendency for heavier nuclei to require more neutrons than protons due to the positive charges being repulsive. The gray lines intersect at the location of the proton rich ^{34}Ar nucleus discussed in this work. The lack of neutrons in the nucleus make ^{34}Ar less stable than ^{34}S, its mirror nucleus. All half life values are taken from the NNDC [4].

while Chapter 5 will take a look at the analysis of the data set. Finally, Chapter 6 will summarize the results and act as a conclusion for the 2015 experiment at Legnaro.

1.1 The Shell Model in Atoms

We can introduce γ-ray spectroscopy by examining the energy levels of nuclei. To do so, a brief examination of the nuclear shell model can be utilized as a useful tool to visualize how these energy levels are formed. The atomic nucleus is a quantum system comprised of fermions. Therefore, it has a shell structure. Within this structure, a closed shell is formed when the next available orbital or shell is well separated in energy. Before examining this in greater detail, we will briefly examine the atom and its treatment with a shell model.

To study the energy levels of atoms, we can use a Hamiltonian with a potential that reflects the observed system. As an example, the Hamiltonian for an atom with Z protons and a single electron is reflected in Equation 1.1.

$$\hat{H}(\vec{r}) = -\frac{\hbar^2}{2\mu}\nabla^2 - \frac{Ze^2}{4\pi\varepsilon_0 r}, \tag{1.1}$$

where e is the charge of an electron, ε_0 is the vacuum permitivity, μ is the reduced mass of the nucleus and electron, $\hbar$ is the reduced Planck constant, and $\vec{r}$ is the vector from the nucleus to the position of the electron. Completing the calculation based on the Hamiltonian results in the discrete energy levels of a hydrogen-like atom that are given in Equation 1.2, with $n \in \mathbb{N}$ being the principal quantum number [5].

$$E = -13.6\,\mathrm{eV}(Z^2/n^2) \tag{1.2}$$

Although the basic layout of a Hamiltonian with a Coulomb potential can be used for all atoms, the specific potential differs based on the charge of the nucleus as well as the number of electrons interacting with the nucleus, or each other. These electrons then fill up the discrete energy levels to form electron shells, where the energy levels being populated are close in energy. The next electron shell would be comparatively well separated in energy from the previous shell.

Although the fundamental interactions are the same, the discrete energy levels of each atom do not follow the same trend as in hydrogen as we add more electrons. We can observe some of this behaviour using the first ionization potential, shown in Figure 1.3, which is associated with the energy required to remove one electron from the atom. One notable trend with first ionization potentials manifests in large spikes around certain elements, $Z = 2, 10, 18, 36, 54,$ and 86. The large spikes can be interpreted as a dramatic increase in the stability of the element from losing electrons, arising in "magic numbers" associated with these atomic numbers. In fact, these numbers correspond with the closure of electron shells, where the filled electron shells correspond with the inert noble gases. The properties of the elements are often dictated only by the valence electrons, or the electrons just beyond the last closed electron shell [3]. As such, the idea of closed electron shells conferring stability to atoms with the valence electrons dictating the overall behavioural trends can be thought of as an atomic shell model.

1.2 A Brief Introduction to the Nuclear Shell Model

A description of the nucleus often utilized is the nuclear shell model, which describes the nucleons orbiting within a central potential created by the nucleons interacting with each other. The shell model is aptly named thanks to the nucleon orbitals being divided by neat and sizable energy gaps to form the eponymous "shells". The shell gaps correspond with specific nucleon numbers $N, Z = 2, 8, 20, 28, 50, 82$ as well as $N = 126$. These so-called "magic numbers" are supported by a wealth of experimental evidence. As an example, neutron and proton separation energies, or the energy required to remove a proton or neutron from its nucleus dramatically changes after a magic number. The success of the

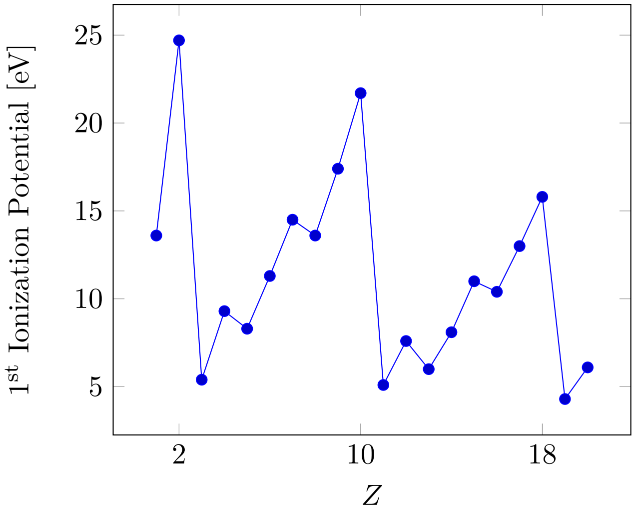

Figure 1.3: Ionization potentials are plotted as a function of atomic number, highlighting the dramatic drop in energy above closed electron shells. Values obtained from Ref. [3].

shell model reproducing these magic numbers is one of the most prominent characteristics of the model [6].

The shell model is built on a Hamiltonian with a central potential, and a first order approximation can be made utilizing a simple harmonic oscillator as the central potential as shown in Equation 1.3.

$$V_{HO}(r) = \frac{1}{2}m\omega^2 r^2, \tag{1.3}$$

where m and ω being the mass and angular frequency of the nucleons respectively, whilst r is the distance to the center of the nucleus. The resulting energy levels of the simple harmonic oscillator in three dimensions is given in Equation 1.4.

$$E_n = \hbar\omega\left(2(n-1) + l + \frac{3}{2}\right), \tag{1.4}$$

where n is a non-zero positive integer, and l is the orbital angular momentum. As nucleons are fermions that obey the Pauli exclusion principle, the resulting degeneracy of each distinct combination of n and l is equal to $2(2l+1)$, where l is the orbital angular momentum of the nucleon. This central potential produces a degeneracy between various combination of n and l. For example, the $2s$ and $1d$ orbitals share the same energy, thus succesfully reproducing the magic numbers $2, 8$, and 20. Further corrections can be applied to get the rest of the magic numbers, namely the introduction of a spin orbit coupling term, V_{SO}, to the potential which is shown in Equation 1.5.

$$V_{SO}(r) = -\frac{2}{\hbar^2} U_{ls} \frac{1}{r} \frac{\mathrm{d}V_C(r)}{\mathrm{d}r} \hat{l} \cdot \hat{s}, \tag{1.5}$$

where U_{ls} is some term that is proportional to the central potential $V_C(r)$, which in this case would be the simple harmonic oscillator. Notably, the spin orbit term, $\hat{l} \cdot \hat{s}$, lifts the degeneracy of each orbital angular momentum and splits them into two new levels based on whether l and s are aligned or anti-aligned. The new levels can be defined by their total angular momentum $j = l \pm \frac{1}{2}$, and have a degeneracy of $2j + 1$. The result of the splitting, where the larger j energy level is by convention assigned to the lower energy, allows the energy levels to organize themselves into distinctive groups that successfully reproduce the magic numbers as shown in Figure 1.4. The spin orbit coupling term also introduces intruder orbitals, where certain energy levels are changed to a degree that they "intrude" into an adjacent shell. These orbitals are usually marked by having parity opposite to other orbitals within the shell.

Changes can be made for the central potential to more accurately represent physical arguments of the nucleus. This is necessary given the fact that the harmonic oscillator has an infinitely high wall where nucleons are always bound, as well as the quadratic nature of the potential well being much too gradual a curve to represent the "skin" of the nucleus [6]. The introduction of a potential with an intermediate form between square well and harmonic oscillator potentials allow for some of these physical arguments to manifest. This potential, known as the Woods-Saxon potential, is shown in Equation 1.6, where V_0 is the depth of the well, R is the average radius of the nucleus, and a is the skin thickness of the nucleus.

$$V_{WS}(r) = -\frac{V_0}{1 + \exp[(r - R)/a]} \tag{1.6}$$

The average radius, R, is given as $R = 1.25A^{\frac{1}{3}}$ fm where A is the atomic mass number. The definition of a is also written as the distance between the well depths $-0.9V_0$ and $-0.1V_0$, which is equivalent to $4a \ln 3$. Typical values for a are $\sim 0.5\,\mathrm{fm}$ whilst a typical well depth is $\sim 50\,\mathrm{MeV}$ [6]. The shape of the Woods-Saxon potential is compared with the harmonic oscillator in Figure 1.5.

The Woods-Saxon potential retains the "well" shape of the simple harmonic oscillator, but has a few notable differences. Firstly, the problem of the infinitely high wall is resolved, as the new potential tends to 0 outside of the radius of the nucleus. Secondly, the center of the well is much more flat and thus tightly bound, as in the case of nucleons trapped in the center of the nucleus. The last difference is the "skin" of the nucleus, where the walls of the potential well are much steeper than a harmonic oscillator for nucleons on the surface.

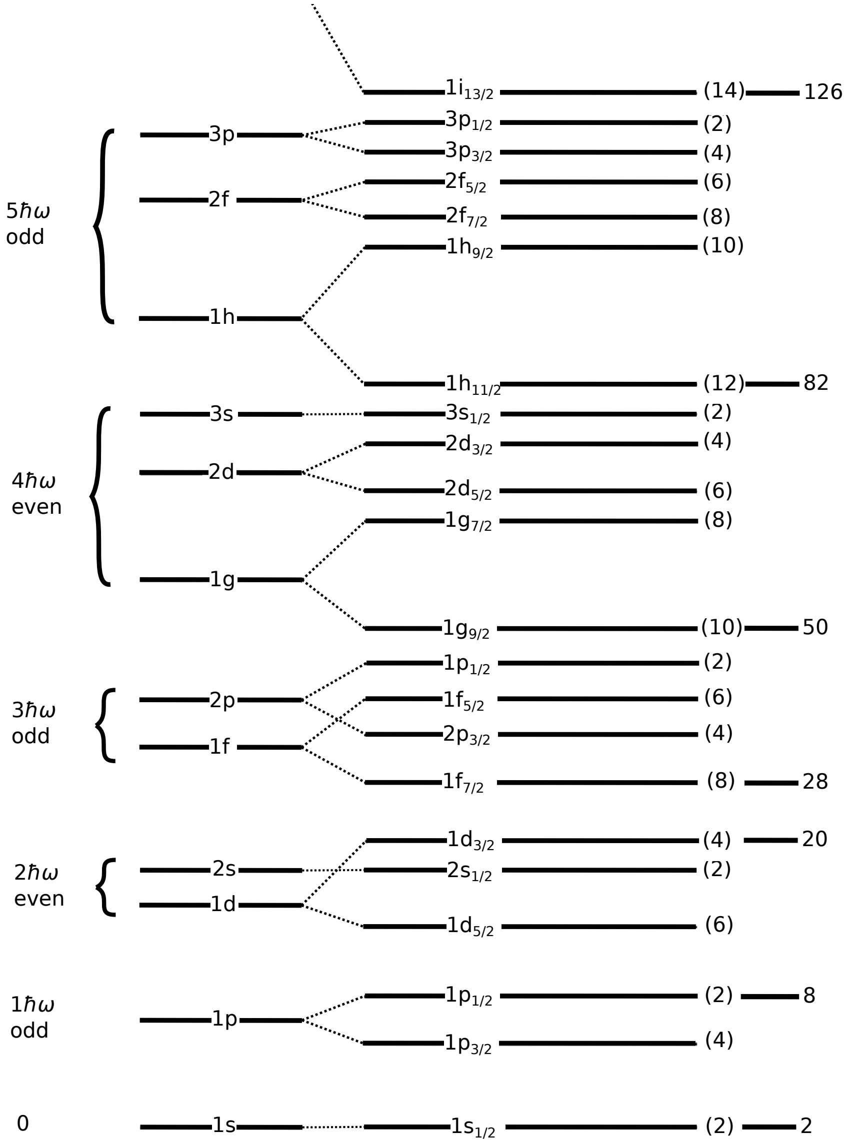

Figure 1.4: Energy levels are shown from the simple harmonic oscillator potential on the left, as well as the final energy levels after considering the spin orbit interaction on the right. The cumulative population of the nucleons is shown on the far right, highlighting the magic numbers for every shell closure. Figure adapted from Ref. [7]

The last distinction to be made would be to differentiate the potential well of protons as well as that of neutrons. The Coulomb repulsion decreases the depth of the well, as well as adding a non-zero positive potential proportional to $1/r$ as r goes to infinity [8]. The contributions of the Coulomb potential are highlighted in Figures 1.5 and 1.6. The effects are minor, and mostly serve to increase the energy levels of protons at higher occupation numbers, resulting in a deviation from the $N = Z$ line, an imaginary line on the chart of

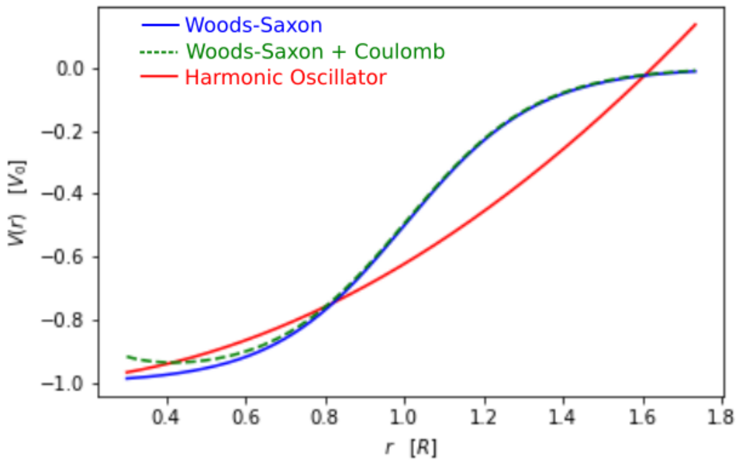

Figure 1.5: The Harmonic Oscillator potential, Woods-Saxon potential, and Woods-Saxon + Coulomb potential are plotted to highlight their differences. Compared with the harmonic oscillator potential, the Woods-Saxon potential is notable for its steeper walls and flat center. Most importantly the Woods-Saxon potential is finite as $r \to \infty$. When looking at the Woods-Saxon + Coulomb potential, we see it is more weakly bound compared to a Woods-Saxon potential as $r \to 0$.

nuclei so called as it demarcates where the number of protons are equal to the number of neutrons, for occupying nucleons.

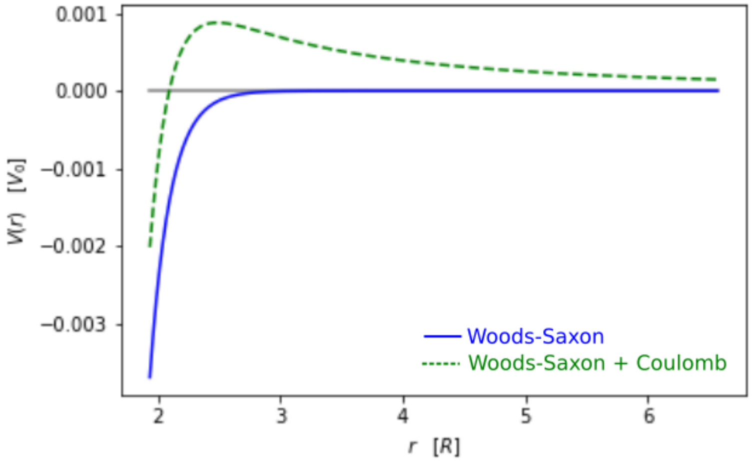

Figure 1.6: The Woods-Saxon potential and Woods-Saxon + Coulomb potential are plotted to highlight their differences. The Woods-Saxon + Coulomb potential has a positive and hence repulsive contribution compared to a pure Woods-Saxon potential. The former potential decays slowly as $\propto \frac{1}{r}$ when $r \to \infty$.

This serves as the basis for a description of the protons and neutrons inside a nucleus in the shell model: the orbitals within a nucleus are populated by protons and neutrons until said orbital is filled, whereupon the next available orbital separated in energy is filled. The picture for nuclei near shell closures is thus simply an inert core of nucleons, and observing the interaction of the particles in the valence shell determines the properties of the nuclei. Energy levels and transitions can also be associated with nucleons exciting from a filled shell to a higher energy level, leaving behind a “hole”. The description of nuclei with an inert core and some valence nucleons does have its limits: the motion of numerous nucleons in heavier and more complex nuclei make the valence space computationally taxing to account for, resulting in the necessity for alternatives to the shell model.

1.3 Angular Momentum and Isospin of Nuclei

The nucleus is composed of two main particles: the proton and the neutron, as shown in Figure 1.1. These two subatomic particles are actually remarkably similar, with the proton having a rest mass of 938.3 MeV compared to the neutron’s 939.6 MeV. As such, it is convenient to call both of them nucleons, and are only differentiated by the proton’s electrical charge when dealing with electromagnetic interactions [9].

Both the proton and neutron are fermions. As spin - 1/2 particles, the nucleons, and by extension, the nucleus, obey the Pauli exclusion principle. As a result, the wavefunction of a nucleus is overall anti-symmetric upon the exchange of any two particles. The individual nucleons have both an orbital angular momentum, $\vec{l}$, as well as a spin angular momentum, $\vec{s}$, that sum to a total angular momentum, $\vec{j}$, as in Equation 1.7.

$$\vec{j} = \vec{l} + \vec{s} \tag{1.7}$$

The single particle total angular momentum and orbital angular momentum are used as quantum numbers to label single particle orbitals as demonstrated in Figure 1.4. These labels follow the form nl_j, where n is the primary quantum number, l is the orbital angular momentum, and j is the total angular momentum. The overall angular momentum of a nucleus, $\vec{J}$, is shown in Equation 1.8 as a sum of the individual angular momenta and spins from A nucleon within the nucleus.

$$\vec{J} = \sum_{i}^{A} \vec{j_i} \tag{1.8}$$

The energy levels of a nucleus are associated with the total angular momentum $\vec{J}$, and are used as quantum numbers to label energy levels for nuclei starting in Section 3.2. The convention for labelling each nuclear energy level follows the pattern of J^{π}, where we have the total angular momentum as well as a label for the parity of the state, with the parity $\pi = (-1)^L$, where L is the total orbital angular momentum.

Nuclear orbitals can also be assigned an isospin T. Isospin is named thanks to its mathematical similarity to the treatment of electron spins: they are vector quantities that go up in integer amounts, and there is a T_3 component demarcated for individual nucleons as $T_3 = +1/2$ for neutrons, and $T_3 = -1/2$ for protons. Just like electrons, isospin sum with each other as an addition of vectors, and a nucleus' total isospin is the sum of the individual nucleon's isospin. Equations 1.9 and 1.10 summarise the isospin of a nucleus, where $T^{(i)}$ are the individual isospins of each nucleon, N being the number of neutrons in the nucleus, and Z is the atomic number of the nucleus.

$$\vec{T} = \sum_i \vec{T}^{(i)} \tag{1.9}$$

$$\begin{aligned}\vec{T_3} &= \sum_i \vec{T}_3^{(i)} \\ &= \frac{N-Z}{2}\end{aligned} \tag{1.10}$$

It is here we can define the mirror of a given nucleus as one with the same number of nucleons, but with the number of protons and neutrons exchanged. As an example, the mirror nucleus of ^{34}Ar, which has $Z = 18$ and $N = 16$, would be ^{34}S with $Z = 16$ and $N = 18$.

The effect of nuclear force on protons is identical to the force's effect on neutrons [10]. In practice, this means mirror nuclei can have similar analogue states that are very similar in energy when considering only the nuclear force.

At the very basic level, the symmetry of the nuclear force is broken by the electromagnetic force, where the latter is around two orders of magnitude weaker than the former relatively speaking. Regardless, the concept of analogue states between mirror nuclei is still used to infer the spin and parity of energy levels [2].

In addition to assigning spins and parities, comparing analogue states is often done in order to quantify the forces within the nucleus. This is usually done using the Mirror Energy Difference (MED) demonstrated in Equation 1.11.

$$MED(J) = E_{Z>N}(-T_3, J^\pi) - E_{N<Z}(+T_3, J^\pi) \tag{1.11}$$

The MED is defined as the energy analogue state J of the proton rich species with a negative T_3 component subtracted by the energy of its neutron rich mirror. The difference in energy is then characterized by contributions of the electromagnetic and nuclear forces. The differences in energy tend to be minor, and MED is then useful as a demonstration of

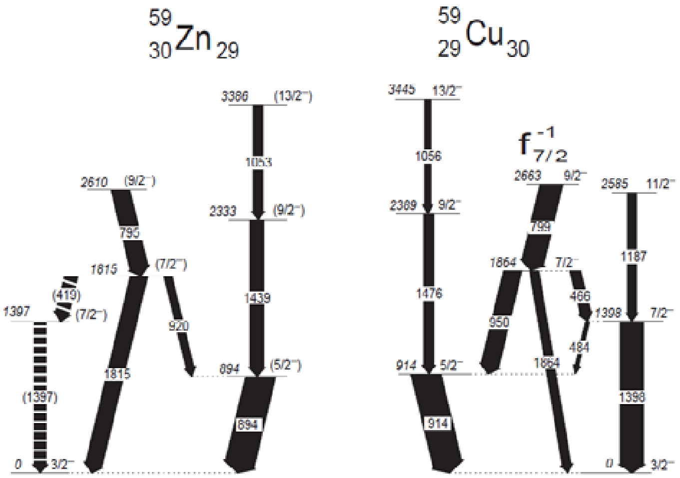

Figure 1.7: Partial level scheme of the mirror nuclei ^{59}Zn and ^{59}Cu with analogue states studied shown. Nuclear energy level schemes are shown using arrows labelled with the transition energy typically shown in keV. The width of the arrows give information on the intensity of the transition, where thickness scales with intensity. The feeding pattern of γ-ray transitions observed as well as the energies of the transitions are all very similar between the two nuclei, highlighting the usefulness of charge symmetry to describe such systems. Used with permission from Ref. [13].

the charge symmetry of the nuclear force, where the substitution of protons and neutrons, $n-n \iff p-p$ would not affect the nuclear interaction energy [11]. The symmetry between analogue states is often highlighted in mirror nuclei studies, where the energy levels between two nuclei are often very close in energy, as in Figure 1.7. Larger MED thus usually reflect unusual behaviour. For example, the work of Ekman *et al.* [12], shown in Figure 1.8, found that the large MED of the 13/2$^-$ between ^{35}Ar and ^{35}Cl came from a monopole Coulomb contribution - specifically an electromagnetic spin-orbit coupling term that was not considered prior.

Another common property for study of analogue states is the Triplet Energy Difference (TED), which examines nuclei with the same number of nucleons as well as $T = 1$ and compares their energies as in Equation 1.12.

$$TED(J) = E(T_3 = -1, T = 1, J^{\pi}) + E(T_3 = +1, T = 1, J^{\pi}) - 2E(T_3 = 0, T = 1, J^{\pi}) \quad (1.12)$$

The excitation energies compared are usually the ground state or the lowest state of the same T for each nucleus in the isospin triplet [15]. The TED also presents an opportunity to demonstrate the charge independence of the nuclear force, which stipulates $n-n \iff p-$

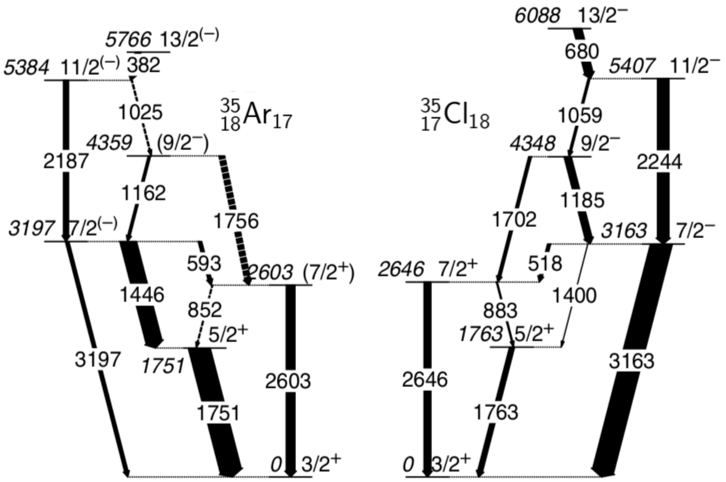

Figure 1.8: Partial level scheme of the mirror nuclei ^{35}Ar and ^{35}Cl with analogue states studied shown. The intensities of γ-ray transitions observed are notably different in the $7/2^- \rightarrow 5/2^+ \rightarrow 3/2^+$ and $7/2^- \rightarrow 3/2^+$ cascades. In addition, the large MED of the 13/2$^-$ state is attributed to a monopole Coulomb contribution that was previously not considered; an example where the description of charge symmetry is not sufficient to describe two mirror nuclei. Used with permission from Ref. [14].

$p \Longleftrightarrow n-p$ interactions are equal in energy. Note that the condition of charge independence is much more stringent than charge symmetry [11].

Both the MED and TED are useful tools to compare nuclei, but are not explicitly used in this work due to a lack data on ^{34}Ar discussed later on.

Chapter 2

Mechanisms and Interactions of Fusion Evaporation Experiments

This chapter compiles the most relevant phenomena when discussing fusion evaporation experiments, and primarily the ones relevant to the analysis of the experiment discussed in this work. This includes covering: the interactions of matter with electromagnetic radiation and charged particles, discussing the decay of high energy electromagnetic radiation known as γ rays, as well as the mechanism of a fusion evaporation experiment and quantifying its products using reaction cross sections.

2.1 Interaction of Electromagnetic Radiation with Matter

Electromagnetic radiation can interact with matter in three main processes: photoelectric absorption, Compton scattering, and pair production. A short summary over the dominance of the effects over γ-ray energies are highlighted in Figure 2.1.

The photoelectric effect is the absorption total energy of a photon which is then transferred to an atomic electron, which can break free of its atom [17]. This electron is called a photoelectron, which has a kinetic energy, E_e, shown in Equation 2.1.

$$E_e = E_\gamma - E_e^{(bind)}, \tag{2.1}$$

where E_γ is the energy of the γ ray and $E_e^{(bind)}$ is the binding energy of the electron within the atom.

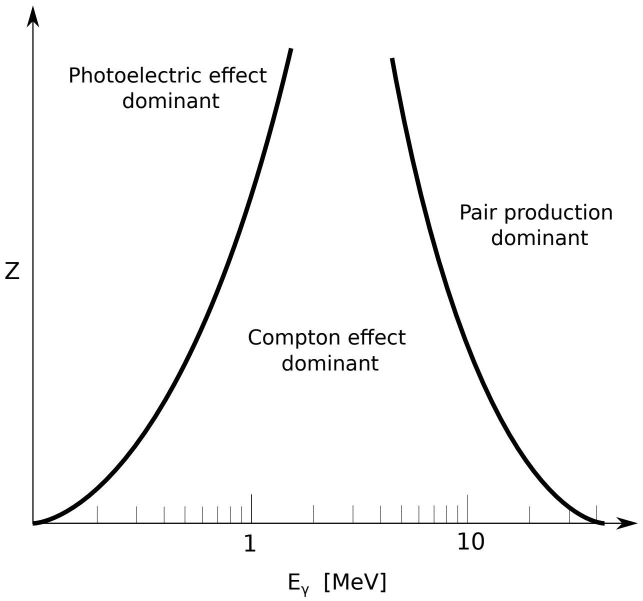

Figure 2.1: The relative importance of the three major types of γ-ray interaction across a variety of Z and energies E$_\gamma$. In general, the dominant interaction tends towards pair production at higher energies, whilst higher Z material lessens the Compton effect. The lines show the values of Z and E$_\gamma$ for which the two neighbouring effects are just equal. Adapted from Ref. [16].

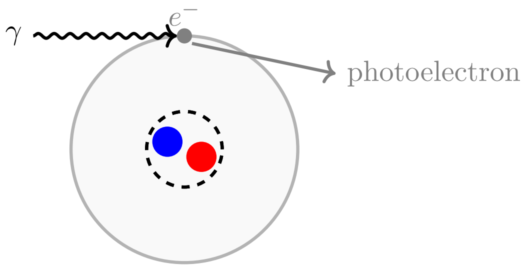

Figure 2.2: A representation of the photoelectric effect: a γ ray is absorbed by an electron that then escapes the atom as a photoelectron. The energy of the electron is given as the energy of the γ ray subtracted by the binding energy of the electron inside the atom.

Notably the photoelectric effect is more significant around 0.1 MeV and decreases at higher energies. The cross section of such events for a single atom is given as an approximation in Equation 2.2.

$$\sigma \propto \frac{Z^4}{E_\gamma^3} \tag{2.2}$$

The dependence on the absorbing materials atomic number Z plays an important role in detector setups, where higher-Z material are preferred to lower ones [9]. This is especially apparent in γ-ray detectors setup with germanium ($Z = 32$) detectors instead of silicon ($Z = 14$).

Compton scattering is an inelastic scattering of incident photons with electrons that tends to occur between 0.1 and 10 MeV [17]. The incident γ ray is scattered by an electron into a different direction. The resulting photons' angular distribution is given by the Klein-Nishina formula for the differential scattering cross section $\mathrm{d}\sigma/\mathrm{d}\Omega$ as shown in Equation 2.3.

$$\frac{\mathrm{d}\sigma}{\mathrm{d}\Omega} = Zr_0^2 \left(\frac{1}{1+\alpha(1-\cos\theta)}\right)^2 \left(\frac{1+\cos^2\theta}{2}\right) \left(1 + \frac{\alpha^2(1-\cos\theta)^2}{(1+\cos^2\theta)[1+\alpha(1-\cos\theta)]}\right) \tag{2.3}$$

Here, $\alpha \equiv h\nu/m_0c^2$ and r_0 is the classical electron charge radius of 2.82×10^{-15} m. This equation notably depends on the atomic number of the material [18]. As a result of the energy lost to the electron, the photon's new energy is dependent on its scattering angle and is given by the Compton scattering formula:

$$E'_\gamma = \frac{E_\gamma}{1 + (1-\cos\theta)\left(\frac{E_\gamma}{mc^2}\right)} \tag{2.4}$$

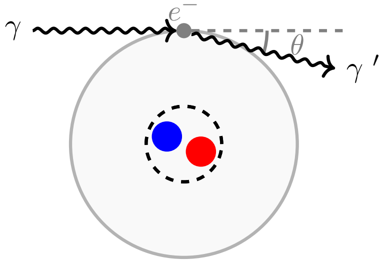

Figure 2.3: A representation of Compton scattering: a γ ray is scattered by an atom's electrons, deflecting the photon by an angle θ, as well as attenuating the latter's energy.

Compton scattering gives rise to the Compton continuum, where the energy of a single peak is distributed and washed out over energies until it effectively serves as background to the spectrum. The maximum energy transferred to the electron, corresponding with a full backscatter, is called the Compton edge, as the Compton continuum abruptly ends just before the full photo-peak. The γ ray can also be scattered before the detector itself, resulting in a backscatter peak that is typically found below 0.25 MeV [17].

Finally, pair production occurs when a γ ray with energy more than 1022 keV forms an electron-positron pair. The 1022-keV cutoff for pair production is derived from the energy required to make an electron-positron pair near a nucleus. As the positron travels through the detector material and loses energy, it will eventually bind with an electron to form positronium and the two will annihilate. Two 511-keV photons are emitted at an angle $\sim 180°$ from each other. From a spectroscopy perspective, it is important to note that the annihilation photons do not necessarily stay within the detector itself. If one of the photons escapes the detector, the recorded energy is the original incident photon energy minus 511 keV. The peak formed from this effect is called a single-escape peak. If both photons escape, the peak is formed at the original energy minus 1022 keV and is called a double-escape peak. The presence of escape peaks complicates analysis as it adds peaks that are effectively contaminants, and must be treated with care to avoid misidentifying transitions and their origins.

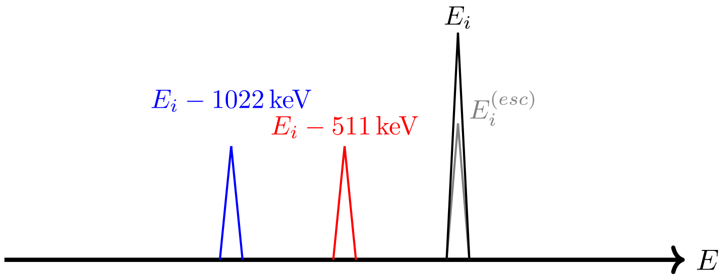

Figure 2.4: Schematic highlighting the effects of pair production on the original full energy peak E_i. The relative positions of the escape peaks are coloured in to highlight the single escape peak and the double escape peak. The counts of the original peak would be reduced as demonstrated by $E_i^{(esc)}$ as some of the counts are lost to the escape peaks.

The reaction cross section for pair production for a single nucleus is given in Equation 2.5 [16].

$$\sigma = \alpha r_0^2 Z^2 P(E, Z) \tag{2.5}$$

Where $\alpha = 1/137$ is the fine structure constant, r_0 is the classical electron radius of 2.82×10^{-15} m, and $P(E, Z)$ is a complex function that can broadly be defined to scale with the energy of the γ ray. As pair production dominates mostly at higher energies, the limited efficiency of the GALILEO γ-ray detectors utilized in the experiment at Legnaro limits the observation of escape peaks and simplifies analysis.

2.2 Interaction of Heavy Charged Particles and Matter

In the discussion of charged particles, such as α particles, their interaction with detectors can succinctly be attributed primarily to the electromagnetic force. Namely, the particles' positive charge interacts with the electrons in the absorbing material. The broad summary of the process involves the charged particle gradually being slowed through exciting and ionizing the absorbing material it interacts with before the charged particle comes to a rest [17]. The linear stopping power, S, which describes the capacity of an absorber to slow and stop a given charged particle is described by the Bethe-Bloch formula shown in Equation 2.6.

$$S = -\frac{\mathrm{d}E}{\mathrm{d}x} = \frac{4\pi}{m_e c^2}\frac{nZ^2}{\beta^2}\left(\frac{e^2}{4\pi\varepsilon_0}\right)^2\left[\ln\left(\frac{2m_e c^2\beta^2}{I(1-\beta^2)}\right) - \beta^2\right] \tag{2.6}$$

The stopping power is defined as the loss of energy for a given length inside the absorber, where m_e is the mass of the electron, β is a ratio of the charged particle's velocity as a fraction of the speed of light, I is the average excitation and ionization potential of absorber, n being the electron density of the absorber, Z being the charge of the stopping particle in units of electron charge e, and ε_0 being the vacuum permittivity. Through the electron density, n, the stopping power scales with the density and atomic number of the target where heavier and denser targets have greater stopping powers. Similarly, the dependence on the electric charge of the stopping particle, Z, means heavier particles like α particles slow down faster than lighter particles like protons.

Within thin absorbers and detectors, the energy loss can be calculated based off an averaged stopping power value as shown in Equation 2.7.

$$\Delta E = -\left(\frac{\mathrm{d}E}{\mathrm{d}x}\right)_{avg}\delta_{target} \tag{2.7}$$

Where $(\mathrm{d}E/\mathrm{d}x)_{avg}$ is the average stopping power of the particle within the thin target while δ_{target} is the thickness of the target. The process is more complex if the particle is slower and significantly slowed down within the thin layer as the stopping power rises.

For the purposes of the Legnaro experiment and its detectors, the process of excitation is equally important to measure the energy of heavy charged particles. As in the case with the GALILEO detector array, the EUCLIDES array is composed of semiconductor detectors, meaning a strong reverse bias is placed on the silicon to accelerate the signal carrying electrons and holes towards the edge of the semiconductor where they are collected by electrodes. Further discussion on the reverse bias places is found in Section 4.1.

2.3 γ-ray Decay

The decay of a γ ray between two states in a nucleus can be defined by both the photon's energy, $E\gamma$, as well as its angular momentum, L. The angular momentum of the photon is restricted based off the initial and final angular momentum of the nuclear states, J, according to Equation 2.8.

$$|J_f - J_i| \leq L \leq J_f + J_i \tag{2.8}$$

In addition, L is restricted to having no monopole ($L = 0$) transitions for single photons. This immediately restricts $0 \rightarrow 0$ transitions within nuclei.

It is possible to define the parity of γ-ray radiation based on the angular momentum of the photon L as represented in Equation 2.9 for magnetic multipole transitions denoted by ML, and Equation 2.10 for electric multipole transitions denoted by EL [9].

$$\pi(ML) = (-1)^{L+1} \tag{2.9}$$

$$\pi(EL) = (-1)^{L} \tag{2.10}$$

The parity rules also suggest that we can divide up transitions into two categories summarised in Equation 2.11: transitions that allow a change in parity betweein J_i and J_f and those that do not.

$$\begin{aligned} \Delta\pi &= \text{yes} \qquad & EL(\text{odd}), ML(\text{even}) \\ \Delta\pi &= \text{no} \qquad & EL(\text{even}), ML(\text{odd}) \end{aligned} \tag{2.11}$$

The probability of a photon being emitted is given in Equation 2.12.

$$\lambda(\sigma L) = \frac{2(L+1)}{\epsilon_0 \hbar L[(2L+1)!!]^2} \left(\frac{\omega}{c}\right)^{2L+1} |\langle\psi_f| (\sigma L) |\psi_i\rangle|^2 \tag{2.12}$$

The probability of γ-ray decay is heavily dependent on the matrix element, $|\langle\psi_f| (\sigma L) |\psi_i\rangle|$, which itself varies with the multipolarity of the transition, σL. Depending on whether the transition is an electric or magnetic multipole, as well as the initial and final state of the photon, the matrix element changes. It is possible to calculate the matrix elements if we assume the transition is due to a single proton that changes from one shell-model state to another. The decay probability for electric transitions are shown in Equation 2.13 whilst the probability for magnetic transitions are represented in Equation 2.14. Both equations are dependent on the energy of the photon in units of MeV, with the decay probabilities given in units of s^{-1}.

$$\lambda(EL) \approx \frac{8\pi(L+1)}{L[(2L+1)!!]^2}\frac{e^2}{4\pi\epsilon_0\hbar c}\left(\frac{E_\gamma}{\hbar c}\right)^{2L+1}\left(\frac{3}{L+3}\right)^2 cR^{2L} \tag{2.13}$$

$$\lambda(ML) \approx \frac{8\pi(L+1)}{L[(2L+1)!!]^2}\frac{e^2}{4\pi\epsilon_0\hbar c}\left(\frac{E_\gamma}{\hbar c}\right)^{2L+1}\left(\frac{\hbar}{m_p c}\right)^2\left(\mu_p-\frac{1}{L+1}\right)^2\left(\frac{3}{L+3}\right)^2 cR^{2L-2} \tag{2.14}$$

In the case of the magnetic transitions stemming from single proton excitations, the probability is also dependent on the magnetic moment of the proton, μ_p, as well as the mass of the proton, m_p. The results of these equations are summarized for a few values of L in Table 2.1.

Table 2.1: Tabulating the Weisskopf estimates for L between 1 and 5 for both electric and magnetic transitions. The unit for λ is in s^{-1} and E_γ is in MeV.

L	$\lambda(EL)$	$\lambda(ML)$
1	$1.03 \times 10^{14} A^{2/3} E_\gamma^3$	$3.15 \times 10^{13} E_\gamma^3$
2	$7.28 \times 10^{7} A^{4/3} E_\gamma^5$	$2.24 \times 10^{7} A^{2/3} E_\gamma^5$
3	$3.39 \times 10^{1} A^{2} E_\gamma^7$	$1.04 \times 10^{1} A^{4/3} E_\gamma^7$
4	$1.07 \times 10^{-5} A^{8/3} E_\gamma^9$	$3.27 \times 10^{-6} A^{2} E_\gamma^9$
5	$2.40 \times 10^{-12} A^{10/3} E_\gamma^{11}$	$7.36 \times 10^{-13} A^{8/3} E_\gamma^{11}$

The transition probabilities calculated under the assumption of single proton excitation are called Weisskopf estimates, and are useful as a reference against experimental transition rates — reaction rates close the the Weisskopf estimates suggest the character of the transition to be from a single particle excitation. If a transition rate is many orders of magnitude smaller than its Weisskopf estimate, it can be assumed there is a poor match-up of initial and final wave functions which is slowing the transition. Similarly, if the transition rate was significantly larger than the Weisskopf estimate, we might guess that more than one nucleon is responsible for the transition [9].

In addition, the transition probabilities are much larger for lower multipolarities, while electric radiation is more likely to occur than magnetic transitions given the same multipolarity.

2.4 Fusion Evaporation Reactions

The population of high-spin states in neutron deficient nuclei can be accomplished using fusion evaporation reactions. These reactions are induced by firing a projectile nucleus, at energies around 3 MeV to 5 MeV per nucleon, at a target nucleus. The two nuclei fuse and the energy from the reaction forms a highly excited intermediate state called the compound nucleus, which also loses its "memory" of the projectile and target nuclei [19]. The compound nucleus gains its energy and angular momentum from the projectile, which had to overcome the Coulomb barrier for the fusion process. The intermediate state quickly de-excites by evaporating subatomic particles such as protons, neutrons, and alpha particles which leave behind a corresponding recoil nucleus. For example, the $N = Z$ compound nucleus ^{36}Ar evaporating 2 neutrons forms a ^{34}Ar nucleus. In most cases, neutron emission is favoured due to the Coulomb barrier. This is not necessarily the case for very neutron deficient nuclei where high neutron separation energies suppress neutron emission and therefore emission of protons and alpha particles are preferred. The recoil nucleus then further de-excites by emitting γ rays which are used to study the nucleus. The γ-ray emission dominates the process as energies approach the yrast line, which are a series of states that have the lowest excitation energy for a given angular momentum.

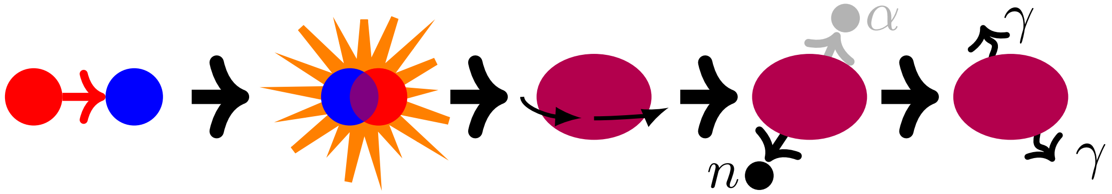

Figure 2.5: During a fusion evaporation reaction, the beam nucleus impacts the target nucleus, which then fuse to form a highly excited compound nucleus. The compound nucleus then evaporates other subatomic particles such as neutrons and charged particles. Finally, the compound nucleus emits γ rays as it decays to its ground state.

The compound nucleus' energy, E_{ex}, is given by Equation 2.15.

$$E_{ex} = E_{cm} + Q_{fus} \tag{2.15}$$

Here E_{cm} is the center of momentum energy of the system shown in Equation 2.16, whilst Q_{fus} is the change in binding energy of the system after the fusion of the beam and target nuclei. The center of momentum energy is shown in Equation 2.16.

$$E_{cm} = E_B - E_R \tag{2.16}$$

Where E_B is the energy of the beam nucleus and E_R being the energy of the recoil nucleus. The change in binding energy, Q_{fus}, is given in Equation 2.17.

$$Q_{fus} = c^2(m_T + m_B - m_{comp}) \tag{2.17}$$

Where m_T, m_B and m_{comp} correspond with masses for the beam, target, and compound nucleus respectively. The total process takes around 1 ns to complete from fusion to observing γ rays.

2.5 Reaction Cross Sections

The reaction cross section, σ, illustrates the probability of a nuclear reaction occurring as an area and can be defined in Equation 2.18:

$$\sigma = \frac{N}{i_{beam}\delta_{target}\Delta t\varepsilon}, \tag{2.18}$$

where N is the number of counts observed, typically taken as the sum of all intensities feeding the ground state in units of particles/counts, δ_{target} being the thickness of the target in mg per cm^2 and converted to particles per cm^2 depending on target material, i_{beam} being the current of the beam in pnA, with 1 particle nanoampere being 6.24×10^9 particles/s, and Δt being the duration of the experiment. In addition, the term ε represents the efficiency for the detector array, such as γ-ray detectors and charged particle detectors. Typically σ is expressed in terms of barns, where 1 barn is equivalent to 10^{-28} m^2, and larger reaction cross sections correspond to more probable reactions. It should be noted that the “thickness” δ_{target} can be converted from a one dimensional thickness, d, as well as the density of the material, ρ. The result is shown in Equation 2.19.

$$\delta_{target} = \rho d \tag{2.19}$$

Chapter 3

Literature Review on A=34 Nuclei Around the N=Z Line

3.1 Motivating the Study of A=30-40 Nuclei

Studies of fp and sd shell nuclei have at times indicated interesting insights into isospin symmetry around the $N = Z$ line. Around $A = 35$, studies into the isospin doublet ^{35}Ar and ^{35}Cl have identified isospin mixing effects as well as a nuclear force contribution to isospin symmetry breaking [20, 12]. The studies of such isospin symmetry breaking effects center around comparing the intensities of transitions between analogue states of mirror nuclei as well as examining their MED. Typical uses of the shell model in this mass range tend to utilize both the sd and fp shells for the valence space.

Several experiments of $A = 34$ nuclei also try to constrain the errors on the reaction rates $^{33}\mathrm{S}(p,\gamma)^{34}\mathrm{Cl}$ and $^{33}\mathrm{Cl}(p,\gamma)^{34}\mathrm{Ar}$ which are used in isotopic abundance calculations [21]. These reactions are often tied to physically measurable quantities, such as isotopic ratios.

3.2 Literature on A=34 Nuclei

The two most recent studies on ^{34}Cl were by: Bisoi *et al.* in 2014 [2] and Van Der Poel *et al.* [22]. The latter paper utilizes results from a $^{31}\mathrm{P}(\alpha,\mathrm{n}\gamma)^{34}\mathrm{Cl}$ reaction at $E(\alpha) = 11.7 - 16.3\,\mathrm{MeV}$ as well as a $^{24}\mathrm{Mg}(^{12}\mathrm{C},\,\mathrm{pn}\gamma)^{34}\mathrm{Cl}$ reaction using an $E(^{12}\mathrm{C}) = 32 - 35\,\mathrm{MeV}$ at an intensity of 80 nA for its results. The ^{24}Mg target was 380 µg/cm^2 thick with a gold backing with a thickness of 25 µm, whilst the ^{31}P target ranged from $100 - 380$ µg/cm^2 in thickness, depending on whether the experiment was run for threshold measurements or lifetime measurements, all with thick gold backing. The detector setup consisted of a Compton-suppression spectrometer and a central High Purity Germanium (HPGe) detector with an additional four lithium drifted germanium (Ge(Li)) detectors for coincidence measurements. The level scheme of ^{34}Cl is observed up to 10.6 MeV, which is very close to the neutron separation energy $S_n = 11.5\,\text{MeV}$. Lifetimes for nine of the levels in ^{34}Cl were measured. Enough data was collected such that angular correlations and angular distributions are used to establish energy levels in addition to their spin and parity.

Delving into specific transitions and notable issues, the beam and target combination of the ^{24}Mg(^{12}C, pnγ)^{34}Cl reaction lent itself to contamination from channels other than the *pn* channel. This was mentioned when examining the 1935-keV transition. Further gating from coincidence data place transitions from ^{31}P at 1928-keV as well as ^{33}S at 1932-keV. The contaminant peaks derived from short lived energy levels in their respective nuclei, confining analysis of the 1935-keV transition in ^{34}Cl to coincidence measurements.

The more recent work of Bisoi *et al.* ^{27}Al(^{12}C,α n γ)^{34}Cl used a beam energy of $E(^{12}C) = 40\,\text{MeV}$. The target utilized in the experiment had a thickness of 0.5 mg/cm^2 with gold backing 10 mg/cm^2 thick. The experiment was run using the multi-detector array of 15 Compton-suppressed HPGe clover detectors. The level scheme was filled up until 10 631 keV, similar to the work discussed prior. Spins and parities of the energy levels are assigned from Directional Correlations from Oriented states (DCO) ratios based on detector configuration, and polarization asymmetry was measured to determine if a transition was electric or magnetic in nature using integrated polarization –directional correlation from oriented nuclei (IPDCO) ratios. Lifetimes and limits on lifetimes were placed on 6 energy levels using Doppler Shift Attenuation Method (DSAM). The lifetimes were extracted from matrices with γ rays detected at 157° or 65° on one axis, and 90° on the other axis, using line shape analysis.

With respect to other $A = 34$ nuclei, the energy level of 2158 keV of $T_3 = 0$ ^{34}Cl was assigned $J^\pi = 2^+$ and $T = 1$ based on the 2_1^+ and $T = 1$ state of $T_3 = -1$ ^{34}S found at 2127 keV. This is also comparable to the 2091-keV 2_1^+ energy level in ^{34}Ar. Comparisons to ^{36}Cl were also considered in assigning the 7699-keV energy level's spin and parity, although shell model considerations were ultimately used in the final tentative assignment of the level as 7^+. Further examination using large-basis shell-model calculations on both the positive and negative parity states helped determine the microscopic nature of the energy levels as well as place spins and parities on some energy levels. The shell model calculations used a valence space consisting of the *sd* and *fp* shells for both protons and neutrons, whilst utilizing an inert ^{16}O core or in some cases, a ^{28}Si core.

Sulfur 34 was examined in the work of Mason *et al.* [1] using ^{24}Mg(^{16}O, α 2pγ)^{34}S at a bombarding energy of 70 MeV. It was conducted at the Laboratori Nazionali di Legnaro utilizing a 400 µg/cm^2 target, as well as a 750 µg/cm^2 target with 15 mg/cm^2 of ^{197}Au backing for lifetime measurements. Detection of γ rays is achieved using the GASP spectrometer, which consists of an array of 40 Compton-suppressed HPGe detectors and a multiplicity filter of 80 BGO scintillators. Channel selection was achieved using the 4π solid angle charged particle detector ISIS, which consists of 40 ΔE – E silicon telescopes.

Energies up to 16.6 MeV were observed. Similarly the yrast states are extended up to 10^+ at 13.34 MeV for positive parities and 9^- at 13.32 MeV for negative parities. Lifetimes of the energy levels was also established using DSAM. Spin states were assigned using angular distributions as well as R_{ADO} ratios. Experimental results were also compared to theoretical shell model calculations for both positive and negative parity states. These models made use of both the *sd* and *fp* shells as the valence space, with considerations of an inert ^{28}Si core as well as where $d_{5/2}$ is included in the valence space. The latter is based on a Monte Carlo shell model with additional interactions to form the SPDF-M interaction.

Argon 34 has been studied by T.K. Alexander *et al.* [23] as well as a more recent study conducted at Argonne National Laboratory [24]. The former experiment bombards a ^{3}He implanted 250 µm thick Au foil with a 80-MeV ^{32}S beam resulting in a ^{3}He(^{32}S,n)^{34}Ar reaction. Three lithium drifted germanium detectors monitored γ rays in coincidence with a liquid scintillator used to tag neutrons. The experiment primarily established the lifetimes of the first two 2^+ states in ^{34}Ar, as well as their experimental matrix elements. The matrix elements also highlight a divergence from theoretical matrix elements provided to the author from private communication.

The Argonne experiment utilized a ^{12}C(^{24}Mg, 2nγ)^{34}Ar reaction with a 95-MeV magnesium beam. The target was a self supported 200 µg/cm^2 carbon target, and was conducted in 2018. The tracking of γ rays was accomplished using the GRETINA array comprised of twelve modules. The γ rays were put in coincidence with mass number $A = 34$ and charge state 13+ on the focal plane of the Fragment Mass Analyzer (FMA).

Both studies establish the presence of a 2091-keV $2^+_1 \rightarrow 0^+$ feeding the ground state, which is taken as the analogous transition to the $2^+_1 \rightarrow 0^+$ 2127-keV transition^{34}S and serves as a point of comparison. Other transitions compared with the mirror ^{34}S include the $2^+_2 \rightarrow 2^+_1$ 1198-keV transition as well as the $4^+_1 \rightarrow 2^+_1$ 2552-keV, both from ^{34}Ar. Energies up to 5 MeV were observed in the Argonne experiment, and uncertainties for the ^{33}Cl(p,γ) reaction are reduced. In another work based on the same experiment, it noted that shell model calculations differed significantly from the excitation energies observed experimentally for the $T = 1$ $A = 34$ mirror pair. Comparisons of MED against ^{34}S, ranging from -57 keV to +418 keV, were largely predictable, with the notable case of odd parity states having large MED's. There were also further constraints on the $\delta^{33}S/^{32}S$ and $\delta^{34}S/^{32}S$ ratios.

There is some motivation to further study ^{34}Ar based off comparisons between available data on the MED between ^{34}S and ^{34}Ar and shell model calculations [25]. Similar comparisons for the TED between the $A = 34$ triplet between sulfur, chlorine, and argon can be done as well. Due to the limited data available on ^{34}Ar at the time of writing the proposal, the Legnaro experiment aimed to expand the level scheme of argon to the 4^+ state and beyond.

Chapter 4

Experiment

The experiment to populated excited states of ^{34}Ar was conducted utilizing the facilities at the Laboratori Nazionali di Legnaro. The experimental setup consists of GALILEO to detect γ rays, EUCLIDES at the center to detect charged particles, and the Neutron Wall at the forward angles to tag neutrons.

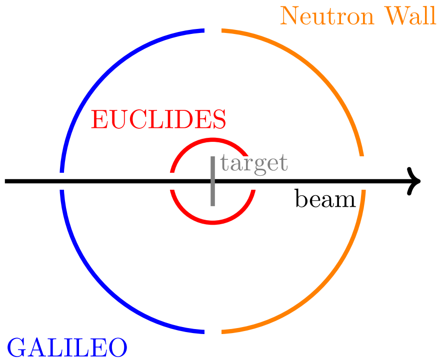

Figure 4.1: Schematic of detector arrays. The target would be located in the centre of the EUCLIDES ball.

4.1 Germanium Detectors for γ-Ray Detection

The γ-ray energies are recorded utilizing High Purity Germanium (HPGe) detectors.

Semiconductor detectors function thanks to the presence of the depletion layer at the p-n junction. At its core, such a detector registers a signal when a particle or γ ray deposits its energy in the depletion layer, creating electrons and holes which then need to be collected. To create a strong signal, or indeed any signal at all, the electrons and holes formed must be collected before they recombine within the semiconductor. As such, a strong reverse bias is placed on the semiconductor to accelerate the signal carrying electrons and holes towards the edge of the semiconductor where they are collected by electrodes.

The presence of the depletion layer is a defining characteristic of semiconductor detectors, and increasing its size effectively increases the size of the detector. Using HPGe allows for larger and larger depletion layers, as the latter's length d can be calculated as shown in Equation 4.1:

$$d = \left(\frac{2\epsilon V}{eN}\right)^{\frac{1}{2}}, \tag{4.1}$$

where e is the electronic charge, ϵ is the dielectric constant, V is the reverse bias voltage applied, and importantly, N is the net concentration of impurities in the bulk semiconductor [17]. Thus, the more pure the material, the larger the depletion layer. This allows for the depletion layer to be almost as large as the detector itself.

The primary reason we utilize germanium detectors for detecting γ rays is their excellent energy resolution, where the full width half max of a 1.333 MeV peak can be measured on the scale of 1 keV [17]. This intrinsic resolution is usually calculated as:

$$\sigma^2 = F\epsilon E_\gamma, \tag{4.2}$$

where F is the Fano factor, which is 0.08 in germanium, ϵ is the 2.96 eV of energy required to produce an electron-hole pair in germanium, and E_γ being the energy of the source γ ray. The Fano factor can be interpreted as the deviation of the process from a Poisson distribution perhaps expected with the number of charge carriers being produced for each γ-ray event.

A mixture of the previously mentioned properties of large reverse bias voltages to fully collect the charge carriers in addition to the large depletion layer make for a large amount of statistics for each γ-ray event.

4.2 Scintillators for Compton Suppression

The Compton suppression shields used in this experiment are composed of Bismuth Germanate (BGO). The shields are scintillators, which can be distinguished from semiconductor detectors by the larger bandgaps present: germanium being 0.7 eV [26] and BGO being 4.20 eV [27].

As Compton events add to background, the usefulness of the Compton suppression shields cannot be understated. In the experiment described in this work, the BGO (Bismuth Germanate) shields identified Compton scattered γ-ray events by looking for coincidences between the shields and the HPGe detectors. The coincidences are then removed to suppress the background in spectra.

In a scintillator, the γ ray once again produces electrons and holes in equal amounts. Instead of simply recombining, scintillators have a number of recombination centers in the forbidden gap between the conduction and valence band, which the electrons can drop into. If this excited state has an allowed transition to let the electron back to the valence band, it will do so whilst emitting a photon.

This photon has the notable characteristic of usually being within the visible range of the electromagnetic spectrum, making the use of photomultiplier tubes (PMTs) viable to collect the signal from the initial event. In addition, the intermediate recombination centers allow the photon to have a different energy from the band gap, thus suppressing the number of self-absorption events if the recombination centers were not present.

The high density and large atomic number of BGO allows for a highly efficient detector, which is a key characteristic in Compton suppression, where efficiency of γ-ray detection is preferred over energy resolution. In contrast, HPGe detectors have an atomic number of 32 compared to bismuth's 83, whilst producing larger detectors of the required semiconductor purity to make detectors becomes increasingly difficult. As a result, the HPGe detectors used are less efficient, and more suited for their high energy resolution, which is discussed further on.

4.3 GALILEO

The detection of γ rays is handled by the GALILEO array, a set of 25 Compton suppressed HPGe detectors taken from the older GASP array [28]. Germanium has become to be one of the most useful tools for γ-ray detection. Their ability for excellent energy resolution, approaching 1.7-2.3 keV at 1332 keV, allows discrimination of transitions very close in energy [17]. For the experiment, the array was arranged into a configuration of 5 HPGe detectors at a ring 152° from the beam, 5 at 129°, 5 more at 119°, and 10 detectors in the 90° ring. This ensures a coverage of a solid angle $\sim 2\pi$. Each germanium crystal is 72 mm in diameter and 80 mm in length. The 90° ring is located 25 cm from the target position while all other rings are placed 22.5 cm from the target. Each detector is surrounded by a BGO anti-Compton shield in order to improve the peak-to-total ratio for spectra. GEANT4 simulations place the total efficiency of the system at 2.4% for 1332-keV γ rays. The intrinsic FWHM of the detector array at 1332 keV is given around 3.1 keV [25].

4.3.1 Calibration and Alignnment

To take advantage of the energy resolution possible by the HPGe detectors, energy calibration must be completed. Four different standard radioactive sources consisting of: ^{60}Co,

Figure 4.2: GALILEO array with the 90° ring on display. BGO Compton suppression shields are clearly visible [29].

^{133}Ba, ^{137}Cs, and ^{152}Eu, were used for energy calibration and efficiency determination. The calibration covered energy ranges from 81 keV - 1408 keV. In each detector, the uncalibrated peaks in the spectra from each detector was fit with a Gaussian function, with the centroid then extracted. The resulting centroids are then plotted against the known energies of the calibration sources to be fit with a 6$^{\text{th}}$ order polynomial. The results of the calibration can be seen in Figure 4.3, which also show the energy alignment of the HPGe detectors. The limited energy range of the calibration and the lower detector efficiency at higher energies results in an inability to characterize peaks over 3 MeV.

The possibility of this nonlinear response of the detectors changing throughout the experiment is present, and the γ-ray transitions of ^{34}Cl (491 keV) and ^{34}S (2561 keV) were examined over all runs due to their relative isolation in energy and high statistics in their respective energy ranges. Notably, detector 16 found within the 90 °ring drifted significantly. A program was written to monitor the detector's drift and reestablishes the calibration step to suggest new parameters for the 6$^{\text{th}}$ order polynomial. The other detectors used were mostly stable throughout the experiment and further reapplications of the calibration were unnecessary between runs.

4.3.2 Efficiency

The efficiency of germanium detectors must be obtained to establish the intensities of observed γ rays. The efficiency curve is produced using the same four radioactive sources used

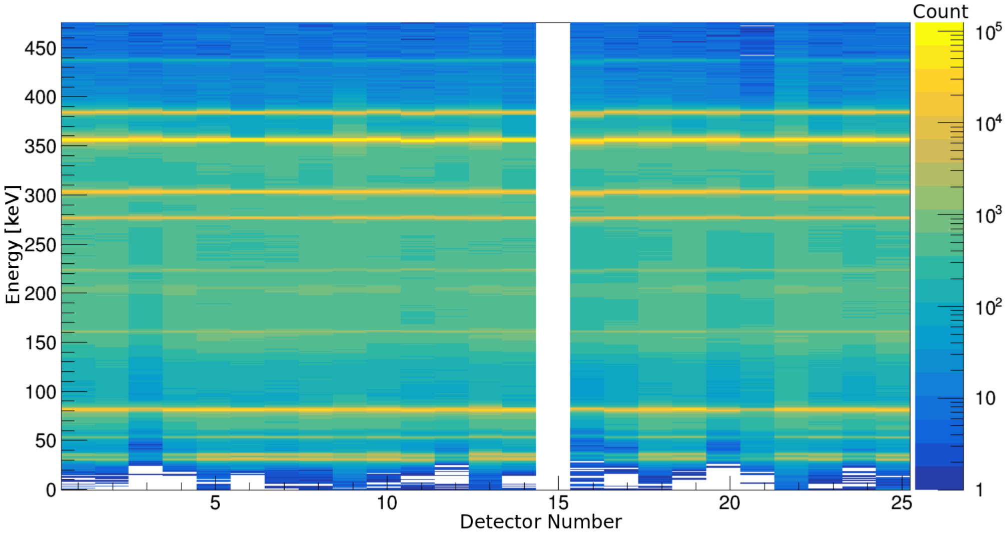

Figure 4.3: Demonstrating an example of a calibrated and aligned detectors' spectra of ^{133}Ba. The different GALILEO detectors are numbered on the x-axis.

in the calibration step. Peaks of known energy and branching ratios are fit with a Gaussian function and given an arbitrary efficiency ε as shown in Equation 4.3.

$$\varepsilon(E) = \frac{A(E)}{BR(E)} \tag{4.3}$$

The arbitrary efficiency ε is characterized by: $A(E)$, the area given by the Gaussian fit, and $BR(E)$ being the branching ratio of the peak at energy E. Although activities for the sources were listed, a small clerical error in the ^{152}Eu source lists the activity at 396 kBq in 2010 whilst being measured at 467 kBq in 2015. Similar errors were encountered with ^{60}Co and the other sources used in the calibration failed to paint a consistent portrait of the absolute efficiencies. For this reason as well as the lack of high energy peaks, arbitrary relative efficiencies are used and deemed sufficient for this analysis. The relative efficiency for each source was then scaled accordingly to establish a trend, before an 6^{th} order polynomial was fit between $\ln(\varepsilon(E))$ and $\ln(E)$ in Equation 4.4 where a_i are the fit parameters. The results are shown in Figure 4.4 plotted as the efficiency against the energy, instead of the natural logarithms of both.

$$\ln(\varepsilon(E)) = \sum_{i=0}^{6} a_i \left(\ln(E)\right)^i \tag{4.4}$$

It should be noted that absolute efficiencies based of the curve constructed are approximated based off data from $\gamma - \gamma$ coincidences from the radioactive sources, and these efficiencies are used later on in Section 5.9 and beyond.

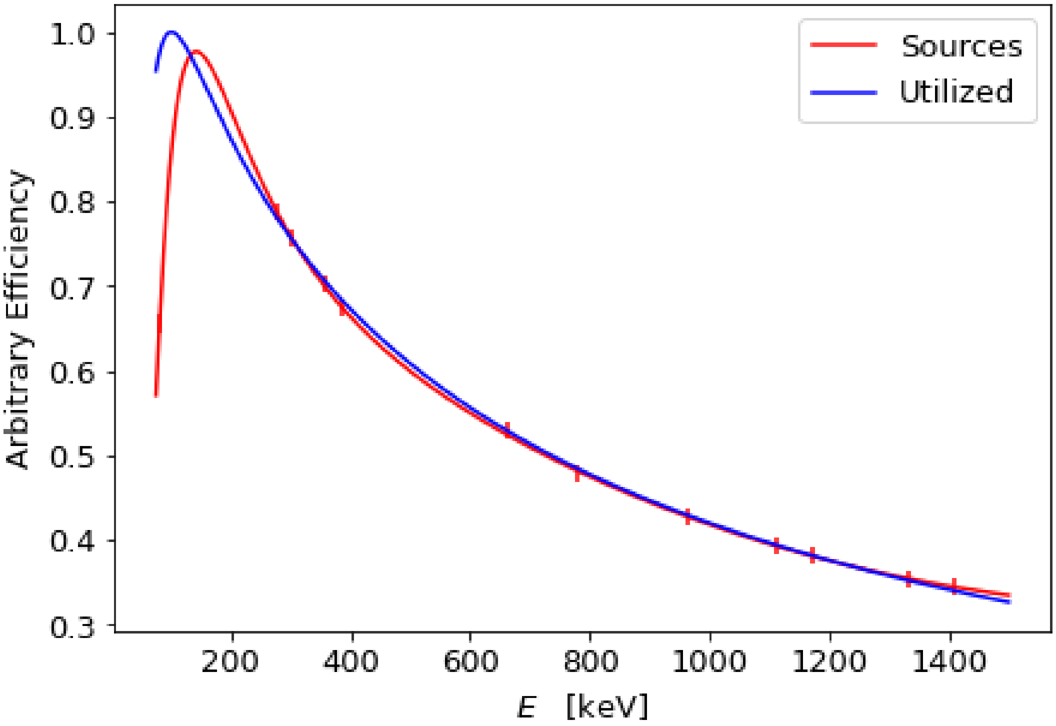

Figure 4.4: The arbitrary efficiency curve fit is shown in red when done from: ^{60}Co, ^{133}Ba, ^{137}Cs, ^{152}Eu sources. After discussions with collaborators, the blue curve was simulated courtesy of Dr. Alain Goasduff and used for the rest of the analysis, as transitions higher in energy than those used in the original efficiency curve were observed [30].

4.4 EUCLIDES

In addition to γ rays, the nature of a fusion evaporation experiment necessitates the use of a particle detector system. To detect charged particles, the EUCLIDES array was used. EUCLIDES is a ball detector composed of 38 silicon ΔE – E telescope detectors situated in the center of the entire GALILEO array. The ball itself houses 38 detectors, each with a surface area of $\sim 10\,\mathrm{cm}^2$, with beam in and beam out positions left empty, providing ~80% of 4π solid angle coverage [31]. In the forward angles, 5 detectors are further segmented into 4 pieces each to cope with the higher count rates possible. The detector system is evaluated at 35% efficiency for α particles and 60% efficiency for protons [32] although this value varies with the reaction kinematics.

The purpose of the ΔE – E telescope detectors is to discriminate between charged particles based on their energies [32]. Each telescope detector houses a thin $\sim 100\,\mu\mathrm{m}$ layer of a silicon

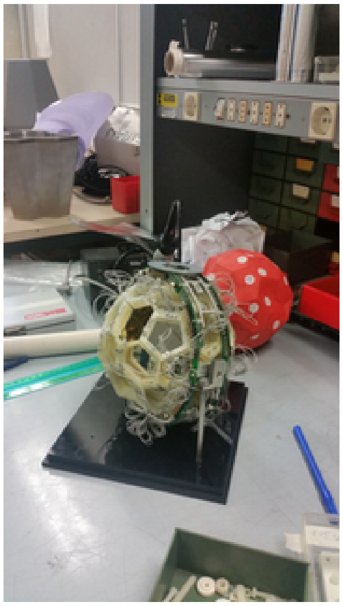

Figure 4.5: EUCLIDES detector system being setup on a workbench for rough scale [29].

detector, as well as a thick ~ 1000 µm layer of a silicon. Charged particles thus deposit some of their energy in the thin layer, whilst depositing the rest of their energy and coming to a rest in the thick layer behind.

Lighter charged particles particles, for example, would be detected at lower energies, whilst depositing a narrow spectrum of energy within the thin ΔE layer. On the other hand, larger charged particles deposit more energy overall. An example of this behaviour is shown later by plotting a matrix of ΔE and E events in Figure 5.5, where the heavier α particles are found at higher energies than the lighter protons p.

4.5 Detecting Neutrons with Liquid Scintillators

As the case with BGO Compton suppression shields, the focus of the Neutron wall is not on energy resolution, but in this case falls on efficiency of detecting neutrons as well as timing.

Liquid scintillators are filled with fluid typically composed of organic molecules dissolved in an appropriate solvent [17]. The solution then undergoes prompt fluorescence upon interaction with neutrons. The fluorescence is then captured by photomultiplier tubes to be converted to an electrical signal. Utilizing liquid scintillators has the benefit of more cost effective, larger scintillators than solid plastics whilst the liquid nature of them minimizes damage due to radiation. In addition, the organic molecules allows for faster timing characteristics compared to the BGO shields around GALILEO detectors. The presence of hydrogen in organic liquid scintillators allows for efficient neutron detection as the latter can lose up to all its energy in a single collision with a hydrogen nucleus. The presence of high atomic mass numbers in scintillators is less ideal as the absorbing material absorbs less energy the higher the mass number is shown in Equation 4.5,

$$E_R \Big|_{max} = \frac{4A}{(1+A)^2} E_n \ , \tag{4.5}$$

where $E_R|_{max}$ is the maximum possible energy of the recoil (absorber) nucleus with mass number A, and E_n is the energy of the incoming neutron [17].

4.6 Neutron Wall

The compound nucleus produced in fusion evaporation experiments emit both charged particles and neutrons. Seeing as the channel of interest is $2n$, the neutron wall was used to tag neutrons. The neutron wall is a hemisphere on the forward angles opposite the GALILEO array. It is composed of 15 liquid scintillators covering $\sim \pi$ of solid angle [33]. The detectors are filled with Bicron BC501A as the scintillating fluid. The detectors closest to the center are viewed by a Philips XP4312B photomultiplier tube (PMT) whilst the rest use Philips XP4512PA.

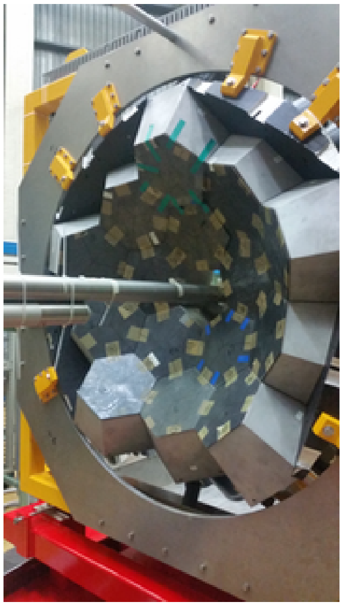

Figure 4.6: Neutron Wall hemisphere on display. EUCLIDES and GALILEO are not pictured [29].

Unlike the other two arrays, measuring energy is not the aim of the neutron wall: the focus is squarely on detecting as many neutrons as possible. Due to the low cross section of neutrons with materials, this goal is harder than in the other detectors. The total efficiency of the setup for a single neutron ranges from $\varepsilon = 25\% - 30\%$ as given in the proposal for the experiment [25]. Given the importance of tagging multiple neutron events, n-γ discrimination is done utilizing several parameters: zero-crossover (ZCO), time-of-flight (TOF) and the charge-integrated anode signal (QVC) [34]. The ZCO is the parameter associated with isolating neutron events from γ rays based on the the different decay time of pulses generated in the liquid scintillator. This is accomplished using a Constant-Fraction Discriminator (CFD), which sums the measured pulse of the event multiplied by a factor χ and a delayed inverse of the original signal. The point where this summed signal crosses the x-axis becomes the ZCO channel, and is independent of the amplitude of the summed pulse; it is purely dependent on the shape of the pulse. The resulting spectrum for ZCO is shown in Figure 4.7. The TOF is produced with reference to the end of the RF signal from the cyclotron and the constant fraction time using the CFD, effectively measuring the time from when a γ ray or neutron is emitted from the nucleus to being detected by the neutron wall. By the nature, neutrons and photons reach the detector at different speeds allowing some manner of discrimination, which is demonstrated in Figure 4.8. Alignment of the TOF is important for the neutron wall, and is shown in Figure 4.9. The QVC is the parameter proportional to charge collected within the PMT and examines energy deposited in each detector.

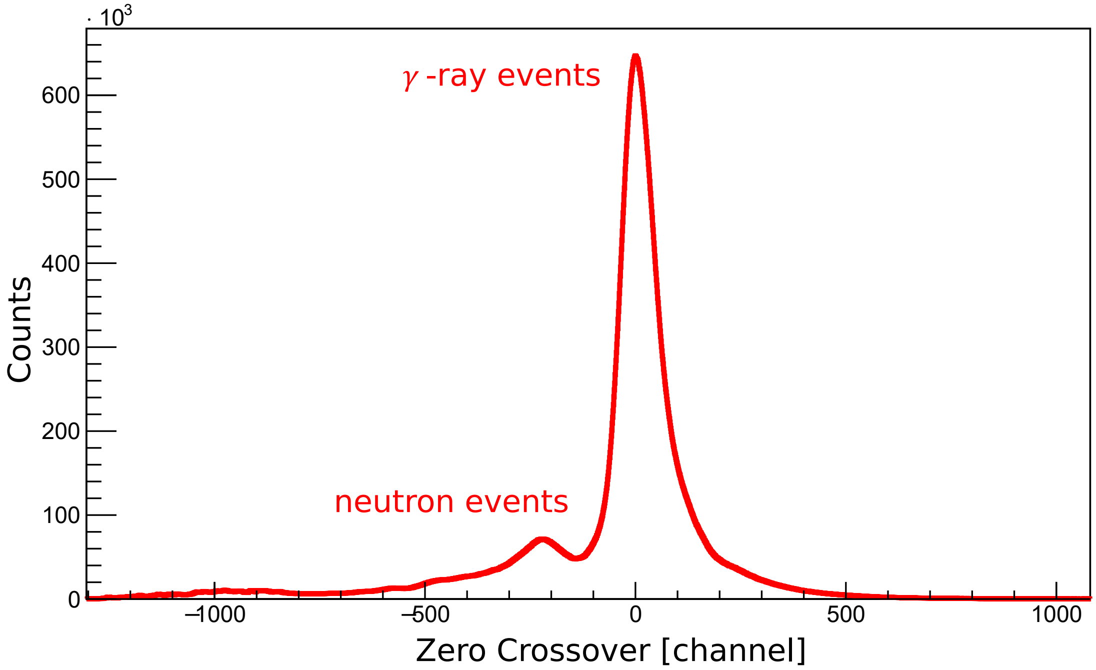

Figure 4.7: Events in the larger peak on the right are associated with γ rays, whilst the broader peak to the left is associated with neutrons events, allowing discrimination between the two types of events.

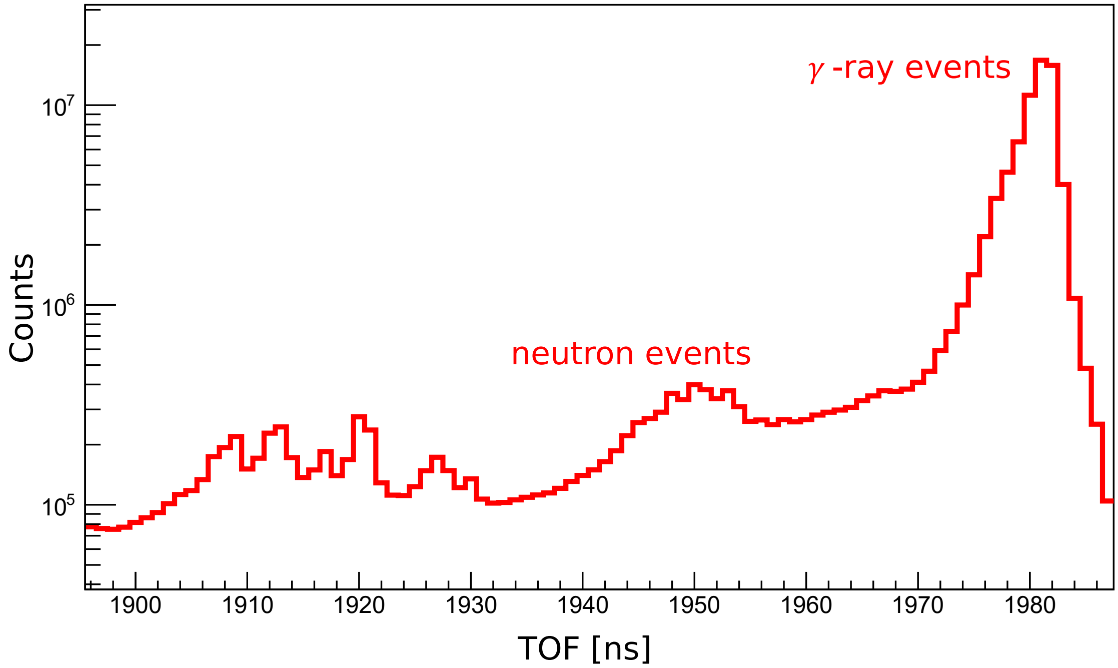

Figure 4.8: Larger TOF channel signals are associated with γ rays, whilst the broader peak to the left is associated with neutrons, which in turn provides a way to separate neutron wall events into neutron events and γ-ray events.

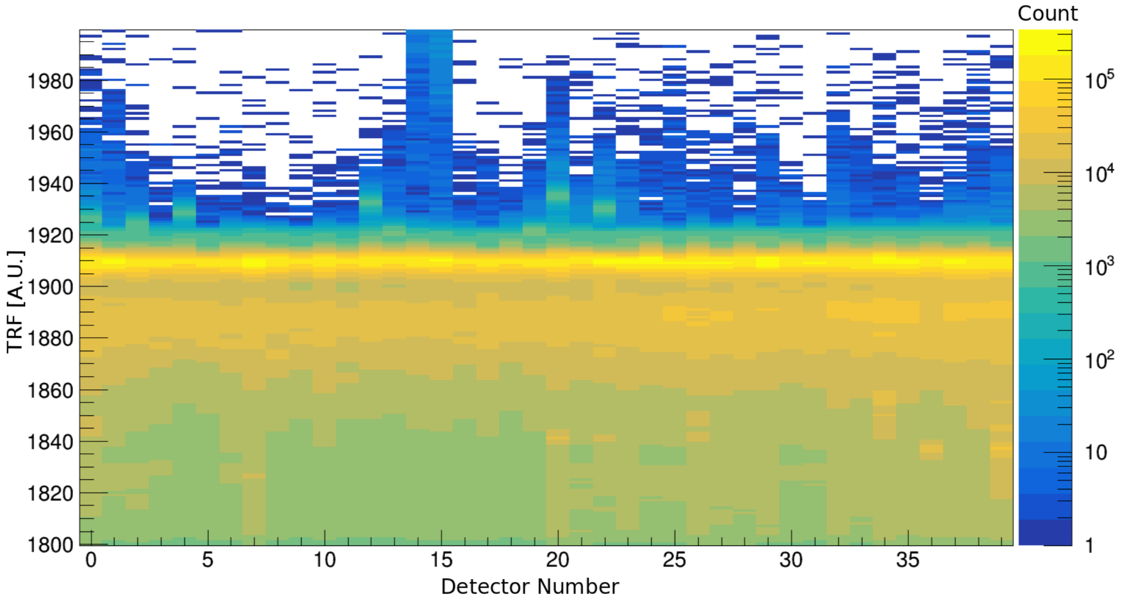

Figure 4.9: Alignment of the TRF, a label for the TOF between each neutron wall detector when associated with the RF signal from the cyclotron. The intense peak between channels must be aligned with each other for accurate neutron particle gates.

Table 4.1: PACE4 calculations run using 100,000 events to show cross sections of different channels opened in this work using the facilities at the LNL with a 35 MeV ^{12}C beam on ^{24}Mg target.

Z	**N**	**A**	**Percent of Events** [%]	**Cross-section** [mb]
18	17	^{35}Ar	0.472	4.51
17	18	^{35}Cl	0.673	6.43
18	16	^{34}Ar	0.022	0.21
17	17	^{34}Cl	13.7	131
16	18	^{34}S	9.96	95.3
17	16	^{33}Cl	0.01	0.0956
16	17	^{33}S	5.75	55
15	18	^{33}P	0.309	2.95
16	16	^{32}S	3.79	36.2
16	15	^{31}S	2.94	28.1
15	16	^{31}P	51	487
15	15	^{30}P	0.068	0.65
14	16	^{30}Si	0.012	0.115
14	14	^{28}Si	10.9	104
13	14	^{27}Al	0.487	4.66

4.7 Experimental Setup

The experiment was a fusion evaporation reaction: ^{12}C(^{24}Mg,2n)^{34}Ar using a 35 MeV ^{12}C beam with an average rate of 8 pnA to populate the high spin states of ^{34}Ar. PACE4, a program used for simulating fusion evaporation experiments using Monte Carlo methods, was used with 100,000 events to estimate that the ^{34}Ar channel would have a reaction cross section of 0.21 mb out of a total of 955 mb for the entire reaction, as shown in Figure 4.1. In comparison, the strongest channel in the reaction, αp, has a cross-section of 487 mb. The self-supported ^{24}Mg targets are 0.5 mg/cm^2 thick and placed at the center of the entire array. Given the average rate of the beam, thickness of the target, and PACE4 calculations, 126 ^{34}Ar nuclei are expected every second before accounting for detector efficiencies. The experiment was run over the course of a week in October 2015, which should yield more than 76 million events over the run of the experiment.

4.8 Contamination of Spectra with Oxygen Associated Channels

The magnesium target utilized had the possibility of being oxidized during transfer into the vacuum chamber, and thus peaks associated with an oxygen target were monitored. During the experiment, a 439-keV peak associated with ^{12}C(^{16}O,αp)^{23}Na was observed over the runs. This reaction had a comparable 1000 mb cross section, although the channel itself is closer to 348 mb. As a result, online peak fitting comparing the 439-keV ^{23}Na peak was compared to the 461 keV ^{34}Cl peak from the *pn* channel to ensure the contamination of the oxygen related peaks did not overwhelm the spectra. If the peak area ratio between the 439-keV peak to 461-keV peak exceeded 0.4 for a run, the magnesium target was changed. As a result, four different magnesium targets were used, and isolating the resulting spectra from channels associated with oxygen was an easy task.

Chapter 5

Analysis

The analysis presented in this work was performed using custom scripts provided by LNL using the ROOT toolkit [35]. Level schemes were constructed from matrices of particle gated $\gamma - \gamma$ coincidences.

This chapter discusses the analysis of the data from the experiment in 2015, culminating in the search for transitions associated with the $2n$ reaction channel recoil nucleus: ^{34}Ar. A summary of the nuclei and their corresponding reaction channels discussed in this chapter are highlighted in Figure 5.1. Doppler corrections must be considered for the γ rays, as they are emitted whilst the recoil nuclei are in flight. Kinematic reconstruction of events associated with charged particles was possible, and allowed for γ-ray spectra with better resolved peaks compared to when an average Doppler correction was applied. The process of constructing coincidences between charged particle events, neutrons, and γ rays is also covered. This includes drawing particle gates for both neutron wall data and EUCLIDES data. During the course of this analysis, a newly observed γ-ray transition was observed in ^{34}S, which was associated with the $2p$ reaction channel, whilst one newly observed energy level and one newly observed γ-ray transition were found in ^{34}Cl, which was associated with the pn reaction channel. There is also a discussion of common contaminant channels, and some of the problems encountered when looking at reaction channels associated with α particles. Comparisons are also drawn with a more recent experiment conducted at Argonne National Labs which successfully observed γ ray transitions associated with ^{34}Ar. Finally, there is a discussion on the reaction cross section observed over the course of the experiment discussed in this work, with an upper limit for the production of ^{34}Ar being established.

5.1 Doppler Corrections

Fusion evaporation experiments result in the recoil nuclei being studied in-flight while emitting γ rays. This motion results in the Doppler shift of the γ rays, making the measurement

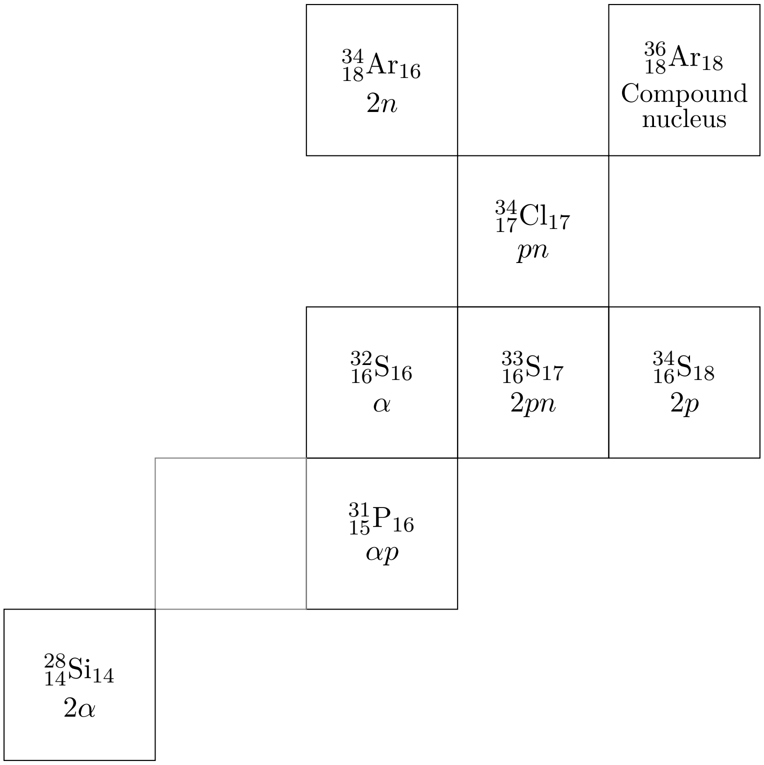

Figure 5.1: Truncated chart of nuclides highlighting nuclei discussed in this chapter with their corresponding reaction channel during the experiment.

of accurate energies for transitions complicated. Fortunately, it is known that the energy of a Doppler shifted photon with energy E_γ emitted from a source travelling at a speed v_s is given by:

$$E_{observed} = E_\gamma \frac{\sqrt{1-\beta^2}}{1-\beta\cos\theta}, \tag{5.1}$$

where $\beta = \frac{v_s}{c}$ is the velocity of the γ-ray emitting nucleus expressed as a ratio of the speed of light, c, $E_{observed}$ is the energy of the photon observed in the lab frame, and θ is the angle between the direction of travel of the source and the emitted photon [36]. From the detector's known geometry, it is possible to reconstruct the energy of a γ ray observed by an HPGe detector at a known angle from the axis of the nuclei's direction of motion.

5.1.1 Kinematic Reconstruction of Doppler Shifted Events

To fully understand the trajectory of the nuclei, the fusion evaporation reaction can be rewritten as a conservation of momentum between the reactants and products. In this context, it is important to find the momentum of the reactants first, which would be the compound nucleus formed when the beam fuses with the target. Given the non-relativistic velocities of the beam, it is possible to use Equation 5.2 to solve for the momentum, p, of the compound nucleus.

$$\mathbf{p}(^{12}C) + \mathbf{p}(^{24}Mg) = \mathbf{p}(^{36}Ar) \tag{5.2}$$

It is possible to find the speed of the beam nuclei through Equation 5.3 given the energy of the beam E,

$$v = \sqrt{\frac{2E}{m}}. \tag{5.3}$$

Knowing the ^{24}Mg target is stationary whilst the ^{12}C projectiles has an energy of 35 MeV resulting in a ^{36}Ar compound nucleus with a speed of $v_{36Ar} = 0.02638c$. From here, the velocity of the compound nucleus is known as it is directed along the beam axis, which is denoted as the $\hat{z}$ axis.

To achieve an event-by-event Doppler correction, it is necessary to determine the momentum of the γ-ray emitting nucleus. As before, it is useful to look at the conservation of momentum of the reaction denoted in Equation 5.4:

$$\mathbf{p_{comp}} - \mathbf{p_{particle}} = \mathbf{p_{recoil}} \tag{5.4}$$

$$\begin{bmatrix} \gamma_{\mathbf{comp}}\mathbf{m_{comp}} \\ 0 \\ 0 \\ \beta_{\mathbf{comp}}\mathbf{m_{comp}}\gamma_{\mathbf{comp}} \end{bmatrix} - \begin{bmatrix} \gamma_{\mathbf{particle}}\mathbf{m_{particle}} \\ \beta_{\mathbf{x,particle}}\mathbf{m_{particle}}\gamma_{\mathbf{particle}} \\ \beta_{\mathbf{y,particle}}\mathbf{m_{particle}}\gamma_{\mathbf{particle}} \\ \beta_{\mathbf{z,particle}}\mathbf{m_{particle}} \end{bmatrix} = \begin{bmatrix} \gamma_{\mathbf{recoil}}\mathbf{m_{recoil}} \\ -\mathbf{p_{x,particle}} \\ -\mathbf{p_{y,particle}} \\ \beta_{\mathbf{recoil}}\mathbf{m_{recoil}}\gamma_{\mathbf{recoil}} \end{bmatrix}, \tag{5.5}$$

where the reactant would be the compound nucleus represented by $\mathbf{p_{comp}}$ and the products would be the particle and the recoil nucleus. Equation 5.5, which is written in natural units, examines solving for the 4-momentum of the recoil nucleus as it occurs within the data sorting code. The information for the particle is gathered from charged particle events detected by EUCLIDES. Within the calculated 4-momentum, the speed of the recoil nuclei β_{recoil} is then used in the Doppler correction of the γ-ray detected in the same 1.2 μs coincidence window. Construction of the particle-γ coincidence events is discussed further in Section 5.3.1.

(a) Schematic showing the extreme case where the ^{12}C nucleus reacts at the end of the target, resulting in considering stopping powers of ^{12}C in ^{24}Mg.

(b) Schematic where the compound nucleus ^{36}Ar is formed at the start of the target instead, such that the stopping powers being considered are of ^{36}Ar in ^{24}Mg.

Figure 5.2

The neutron wall is not sensitive to neutron kinetic energies, so event-by-event kinematic reconstruction is not possible. Here, an average value of β was determined empirically to best reproduce the known transition energies as shown in Figure 5.4. Consequently, spectra associated with neutron particle gates have poorer energy resolution.

5.1.2 Stopping Power Within the Target

To properly obtain γ-ray energies, it is necessary to consider the energy loss of the projectile within the target material. To consider such effects, the stopping power of a ^{12}C beam or ^{36}Ar compound nucleus on a 0.5 mg/cm^2 ^{24}Mg self-supporting target was calculated using the program Stopping and Range of Ions in Matter (SRIM) [37]. Two extreme scenarios are calculated for the beam: the case where the compound nucleus is formed at the end of the target, or at the beginning of the target. From examining these cases, we can use the worse of the two with respect to the slowdown of the compound nucleus to see if Doppler corrections will be affected in a significant manner.

The two cases are schematically shown in Figure 5.2 (not to scale). In the case of the compound nucleus being formed at the end of the target, the energy loss of the ^{12}C projectile as it travels through the full thickness of the target is considered. SRIM lists the electronic stopping power of a 35-MeV ^{12}C beam in the 0.5 mg/cm^2 target at 2.967 MeV/(mg/cm^2). Over the thickness of the target, the energy of the beam is consequently reduced by 1.484 MeV resulting in the velocity of the compound nucleus to be $v_{36Ar} = 0.02581c$, or 2.1 % less than the original projectile. In this scenario, the beam energy is reduced to 33.52 MeV from which a PACE4 calculation can be done. The reduction in beam energy from the original 35-MeV ^{12}C beam on ^{24}Mg results in a reduction of the reaction cross section of ^{34}Ar from 0.2 mb to 0.1 mb, or a factor of two.

The other extreme case would be where ^{36}Ar is formed at the start of the target and loses energy traversing through the target. The heavier ^{36}Ar ions traversing through the same ^{24}Mg target result in a stopping power of 16.93 MeV/(mg/cm^2), and 8.456 MeV of the compound nuclei energy is lost. The large energy loss is reflected in the speed $v_{36Ar} = 0.01385c$, or 47 % less than if stopping powers were not considered at all. Using this case, the resulting error on the Doppler corrected γ-ray energy is ~ 1 %. For a 1-MeV peak, this contributes at least 10-keV to the width of the peak.

It is important to note that the estimates here are illustrative since they assumed a static stopping power over the length of the target. Realistically, as the beam nuclei slows within the target, the stopping power increases resulting in a larger contribution to the error of the Doppler corrected γ-ray energies measured and by extension the width of the peaks. Simulations based on these considerations could theoretically be written, but were not applied in this specific work due to time constraints. The formation of the compound nucleus also takes place throughout the volume of the target, and is not necessarily confined to just the front or rear of the target.

5.1.3 Empirically Assigned Compound and Recoil Nuclei Velocities

Although it is possible to calculate the velocity of the compound nucleus through Equation 5.3, Doppler corrected γ-ray spectra using the calculated velocity of $\beta_{36Ar} = 0.02638$ does not result in accurate energies for known transitions. To remedy this, it is best to start by expanding Equation 5.1 around $\beta = 0$ to get Equation 5.6:

$$\frac{E_{observed}}{E_\gamma} \approx \beta \cdot (\cos\theta) + 1, \tag{5.6}$$

where $\frac{E_{observed}}{E_\gamma}$ is the ratio between the observed energy of the γ ray and the energy of the γ ray in the centre of mass frame. By evaluating a number of measured γ-ray transitions relative to their known transition energies as a function of the cosine of detector angles, it is possible to fit experimental data to Equation 5.6. This was done as shown in Figure 5.3, where the ratio $\frac{E_{observed}}{E_\gamma}$ was fit to the cosine of the corresponding detector angles $\cos\theta$, leaving the velocity of the compound nucleus, β, corresponding to the slope of the fit.

The result of fitting the transitions was an average velocity of the γ-ray source, the recoil nucleus, $\beta = 0.0224(3)$, which was the value used in further data analysis where kinematic reconstruction was not possible.

It should be noted that for channels where kinematic reconstruction is applied, the velocity of the compound nucleus is required, not the velocity of the recoil nucleus. The velocity of the compound nucleus was established by comparing the energies of transitions with the more general Doppler correction, with some test value β_k used for the kinematic reconstruction. This process is shown for ^{34}S in Figure 5.4.

Taking the variance from the energy of the fitted peaks into account, it was found that $\beta_k = 0.0231(5)$.

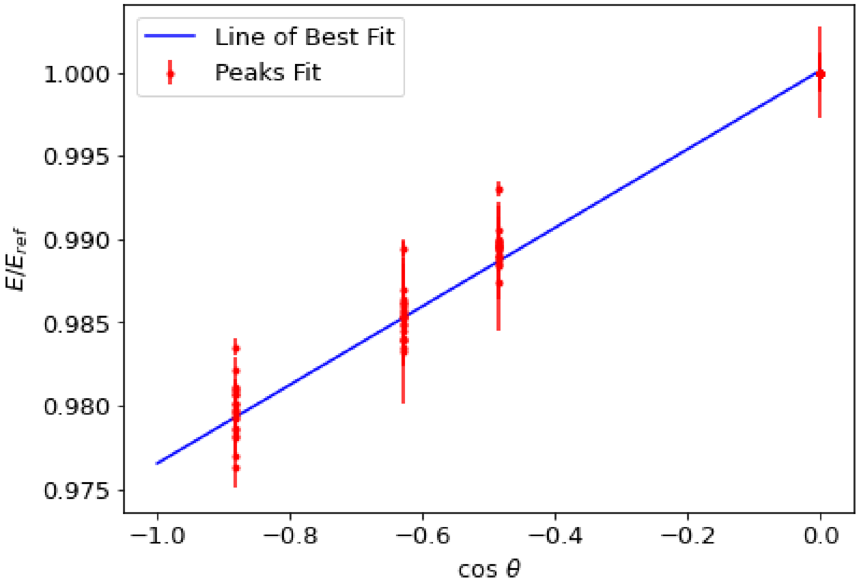

Figure 5.3: Experimentally observed transitions are normalized to their literature energy E_{ref} and plotted against the cosine of their detector angle $\cos\theta$. The slope of the fit corresponds to the average β, the average velocity of the recoil nucleus emitting the γ rays.

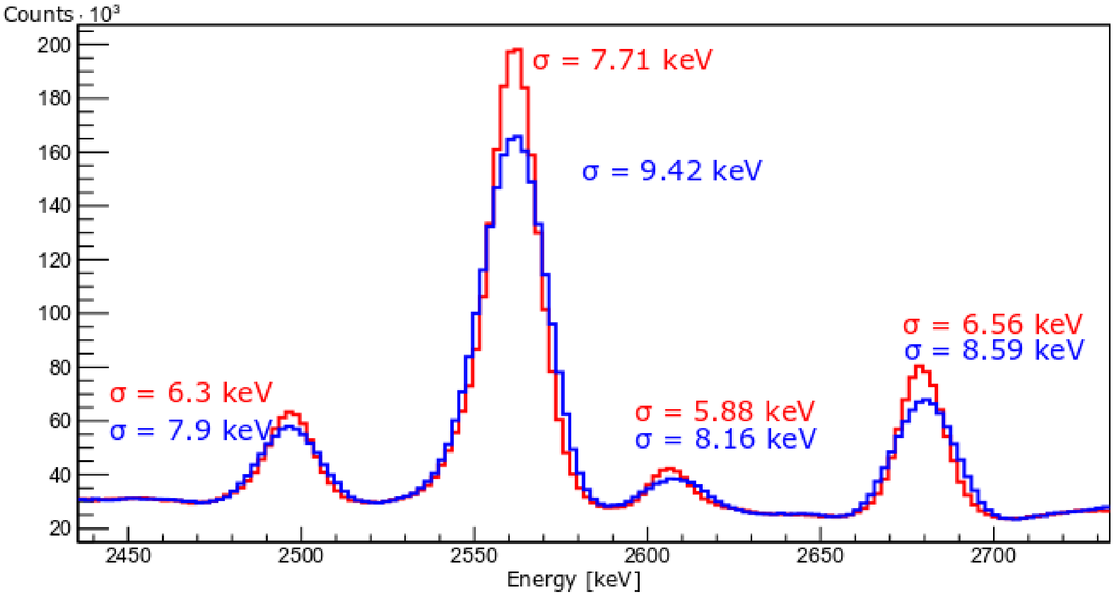

Figure 5.4: Comparison of peak widths and relative positions between kinematic reconstruction spectrum ($\beta_k = 0.0231$) and averaged Doppler corrections ($\beta = 0.0224$) on the $2p$ channel associated with ^{34}S. This ensures that the two values used for the recoil and compound nucleus velocities are consistent. The much narrower peaks produced from the kinematic reconstructions are also highlighted by comparing the standard deviation for each fit, σ.

5.2 Peak Widths with Doppler Corrections

As covered in Section 4.1 the intrinsic width of HPGe detectors around 1.3 MeV is given as $\sigma = 1.3\,\text{keV}$. However, under fusion evaporation experiments with multiple detectors, the peaks are shifted and broadened due to the Doppler effect. The total deviation of the Doppler broadened peaks, σ_T, can be given as in Equation 5.7:

$$\sigma_T^2 = \sigma_I^2 + \sigma_\Omega^2 + \sigma_{det}^2 + \sigma_\beta^2, \tag{5.7}$$

where σ_I is the intrinsic deviation of the peak from the HPGe detector as discussed in Section 4.1, σ_θ representing the error associated with the assumption recoil nuclei follow the beam axis, σ_{det} is associated with the detector opening angle, and σ_β is the error from the velocity of the recoil nucleus. The latter value, in turn, relies on the error of the detector solid angle Ω as well as the error of the recoil nucleus' velocity β. The total deviation of a transition at 1.3 MeV is measured to be $\sim 5\,\text{keV}$, much larger than the intrinsic deviation.

5.3 Particle Gating

5.3.1 Charged Particle Gates

Charged particle gates are not directly necessary for the $2n$ channel, since the evaporated neutrons are not detected by EUCLIDES, but are important nonetheless when looking at other channels. By analyzing well known reaction channels to the experiment, it is possible to verify the integrity and accuracy of the experimental setup and event-by-event Doppler corrections before turning to the $2n$ channel. For example, the pn channel producing ^{34}Cl has a reaction cross section of 133 mb. At three orders of magnitude larger than the reaction channel for ^{34}Ar, confirming the transitions and intensities observed in previous examinations of ^{34}Cl is a relatively simple task and will give the user confidence in their observations of the weaker $2n$ channel.

To create charged particle gates, E $-\Delta$E matrices are created for each EUCLIDES detector as discusses in Section 4.4. Particle gates for each run could be created/"drawn", but seeing as the matrices on a series of runs on the same target did not vary in a meaningful way, particle gates were drawn for each target and applied to all relevant runs. With the matrices constructed, "banana gates" were drawn along characteristic features on the matrices, as shown in Figure 5.5. The matrices are populated according to the energy deposited in the ΔE layer of the detector on the y-axis, and the E stopping layer on the x-axis. All particle events within a given banana gate are attributed to a specific fusion evaporation event being detected in a single EUCLIDES detector according to these energies. The more energetic α particles are found at the top portion of the matrix compared to the protons which deposit

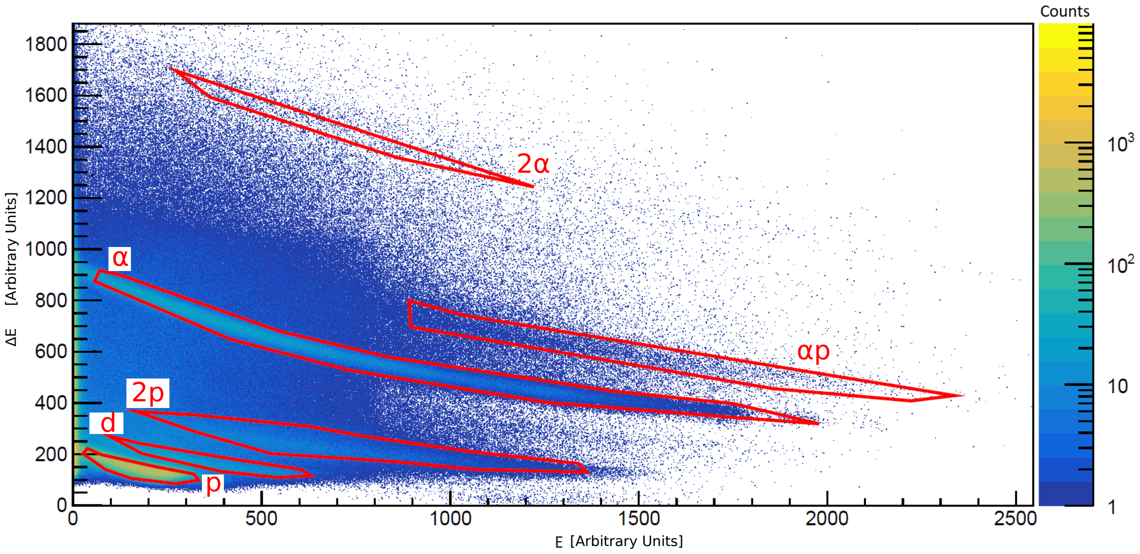

Figure 5.5: Demonstration of particle gates being drawn around charged particle events detected by EUCLIDES. This matrix is constructed using one run on one of the detectors in the forward angles of EUCLIDES.

and have less energy. Any γ rays observed in prompt time coincidence with any particles in these gates are then assigned to these channels. The two dimensional gates applied to the EUCLIDES detectors produce γ-ray spectra corresponding to the relevant reaction channel.

Although the charged particle gates isolate specific reaction channels, contaminants are still observed. The strongest channel from the experiment, ^{31}P, has a strong presence in the form of a 1266-keV $3/2^+ \rightarrow 1/2^+$ transition.

5.3.2 Neutron Gates

The nucleus of interest, ^{34}Ar, is associated with the $2n$ channel, thus introducing the need for the Neutron Wall, which was briefly discussed in Section 4.6. Similar to how EUCLIDES is used to generate charged particle gates, a comparable process is utilized for isolating γ rays associated with neutron events. In the case of the neutrons, it is more useful to examine ZCO-TOF matrices to differentiate neutron events from other signals as shown in Figure 5.6. The characteristic ZCO peak for neutrons is broader and offset from other light signals detected by the liquid scintillators, with the latter peak being more sharply centered around 0. Gates are then drawn around the characteristic peaks of the matrix.

The neutron gates allow for observations of reaction channels such as pn ^{34}Cl, $1n$ ^{35}Cl, and $2n$ ^{34}Ar.

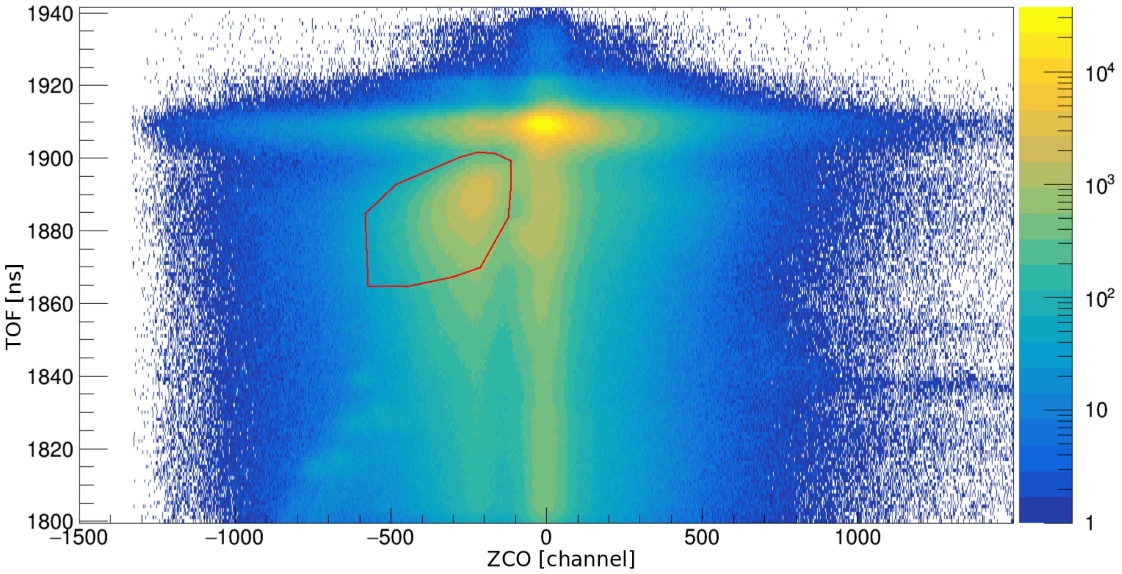

Figure 5.6: Demonstration of gating around neutron events shown in red. Notice the broad, off center nature of the neutron peak in comparison to the photopeak which is centered around ZCO = 0.

5.4 Coincidence Method

To build the level schemes, coincidences between γ rays were examined within each channel. A $\gamma-\gamma$ coincidence matrix is populated when two γ rays are detected within 400 ns of each other. The schematic shown in Figure 5.7 serves to illustrate two such γ rays part of the same cascade, and when detected within the narrow coincidence window, can be attributed as being emitted from the same nucleus.

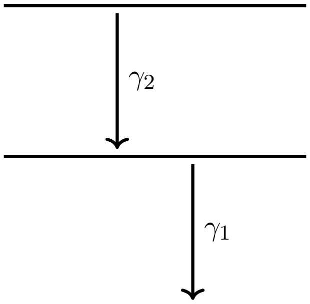

Figure 5.7: Demonstration of a cascade formed by the γ ray γ_2 feeding γ_1. Any two γ-rays detected within the coincidence window are used to populate the $\gamma-\gamma$ coincidence matrix, and are considered to be in coincidence.

Analysis of these $\gamma-\gamma$ matrices allow the identification of cascades of γ-ray transitions for the channel of interest, and further validates the experimental setup when comparing data with previously reported results as shown in Table 5.2 and Table 5.3.

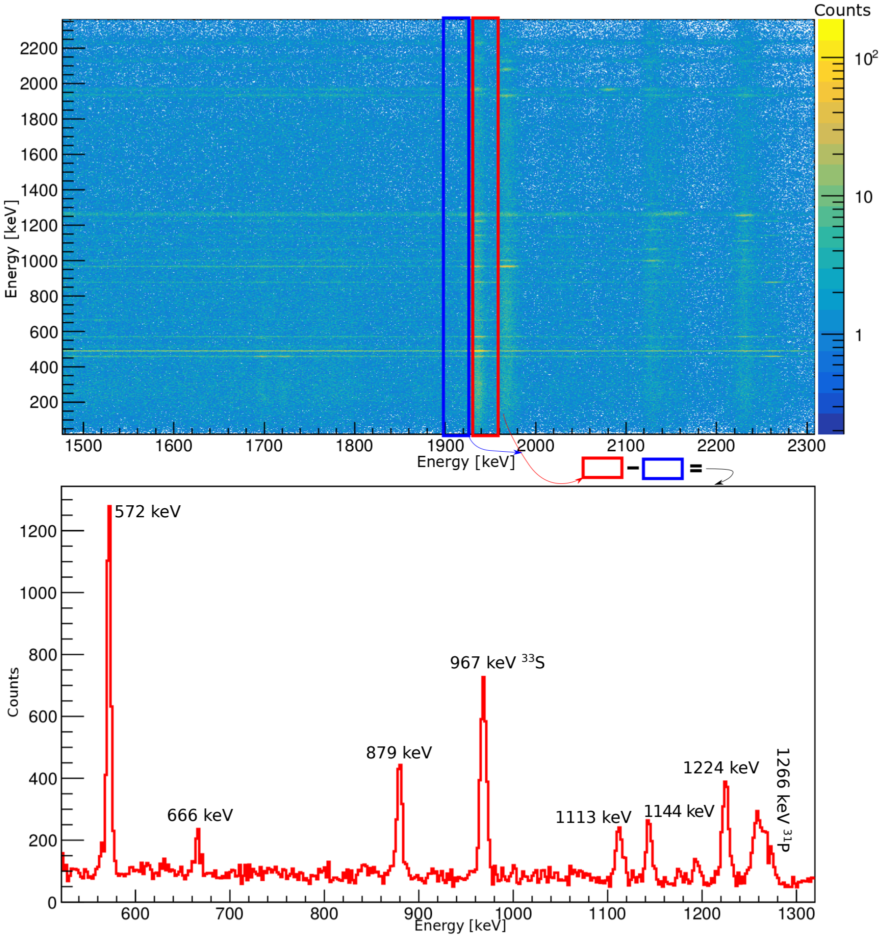

Figure 5.8: An example of a γ-ray spectrum particle gated on the *pn* channel with a gate drawn around the coincident 1935-keV transition and background subtraction applied is shown below the $\gamma - \gamma$ coincidence matrix used to construct it.

A schematic of how the γ-ray gates are drawn is shown in Figure 5.8. First, a projection across the transition of interest is shown by the red box. The second projection is marked by the blue box and is used as a "background" slice to remove coincidences with Compton scattering events from higher energy transitions. The resulting γ-ray spectrum is shown on the bottom of the figure, where it is possible to identify γ rays originating from energy levels up to 7250-keV excitation energy.

Interestingly, contamination is still present at times despite the application of both: particle gates to isolate specific reaction channels, combined with specific energy gates corresponding to nuclei produced from those reaction channels in the $\gamma - \gamma$ matrices. This is, more often than not, due to the large intensity of contaminants in the channels after particle gating, and the fact that a lot of the contaminant peaks are close in energy to many intense transitions in the channels of interest. As an example, Figure 5.9 showcases such contamination as the 2128-keV transition from ^{34}S overlaps with a broad ^{31}P-based 2148-keV transition.

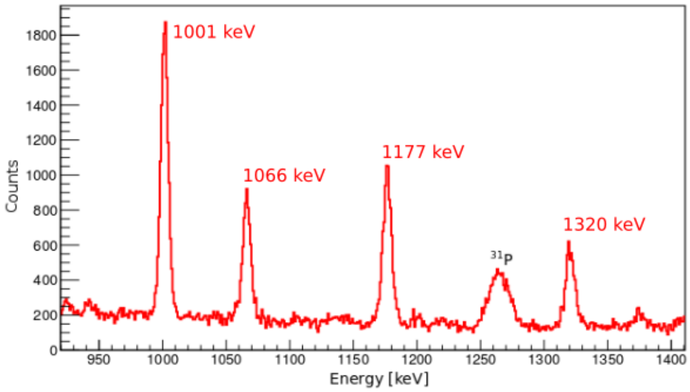

Figure 5.9: Background subtracted γ-ray spectrum particle gated on the $2p$ channel gated around the 2128-keV transition in ^{34}S highlghting the strong presence of ^{31}P due to the γ-ray gate drawn overlapping with a very broad ^{31}P-based 2148-keV transition. Known ^{34}S transitions are labelled with their energies.

5.5 Particle Gated Spectra

Spectra for a specific particle channel are built from any observed γ-ray event coincident with a specific particle gate. As an example, an event is attributed to the decay of ^{34}Cl when one γ ray is observed in coincidence with a EUCLIDES event associated with a single proton and a neutron wall event. Due to the high count rate of the ^{31}P channel, it is a recurring contaminant across many spectra identifiable with the 1266-keV peak. When looking at $2p$ particle gated γ rays, events associated with ^{31}P can be misidentified in quantities up to 130(5) % relative to the correctly identified ^{34}S events; ^{31}P contaminants are found in quantities comparable to the expected ^{34}S due to the high calculated reaction cross-section of ^{31}P. Another prominent and recurring contaminant is ^{33}S with a calculated cross-section of 55 mb and contaminant peaks: 841-keV, 967-keV, and 1967-keV recurring the most. A discussion on contamination in various particle gates can be found in Appendix B.

To validate that the experiment setup and analysis suite, two well studied channels were examined: ^{34}S and ^{34}Cl. The level schemes are shown in Figure 5.11 for ^{34}S and Figure 5.12 for ^{34}Cl.

5.5.1 ^{34}S — $2p$ Reaction Channel

Over the course of the experiment, energy levels up to 11810 keV were populated when examining the ^{34}S spectrum. Populated by the evaporation of $2p$, this is an excellent resource for confirming that the kinematic reconstruction of the fusion evaporation events is working properly. The level scheme is highlighted in Figure 5.11 with the associated list of transitions in Table 5.1 where they are compared with the work of Mason *et al.* [1]. When compared with the ENSDF file for ^{34}S [38], many of the same energy levels are populated with comparable branching ratios from each energy level as shown in Table 5.2. One new transition is tentatively assigned through $\gamma - \gamma$ coincidence and more information on this transition can be examined in Section 5.6.

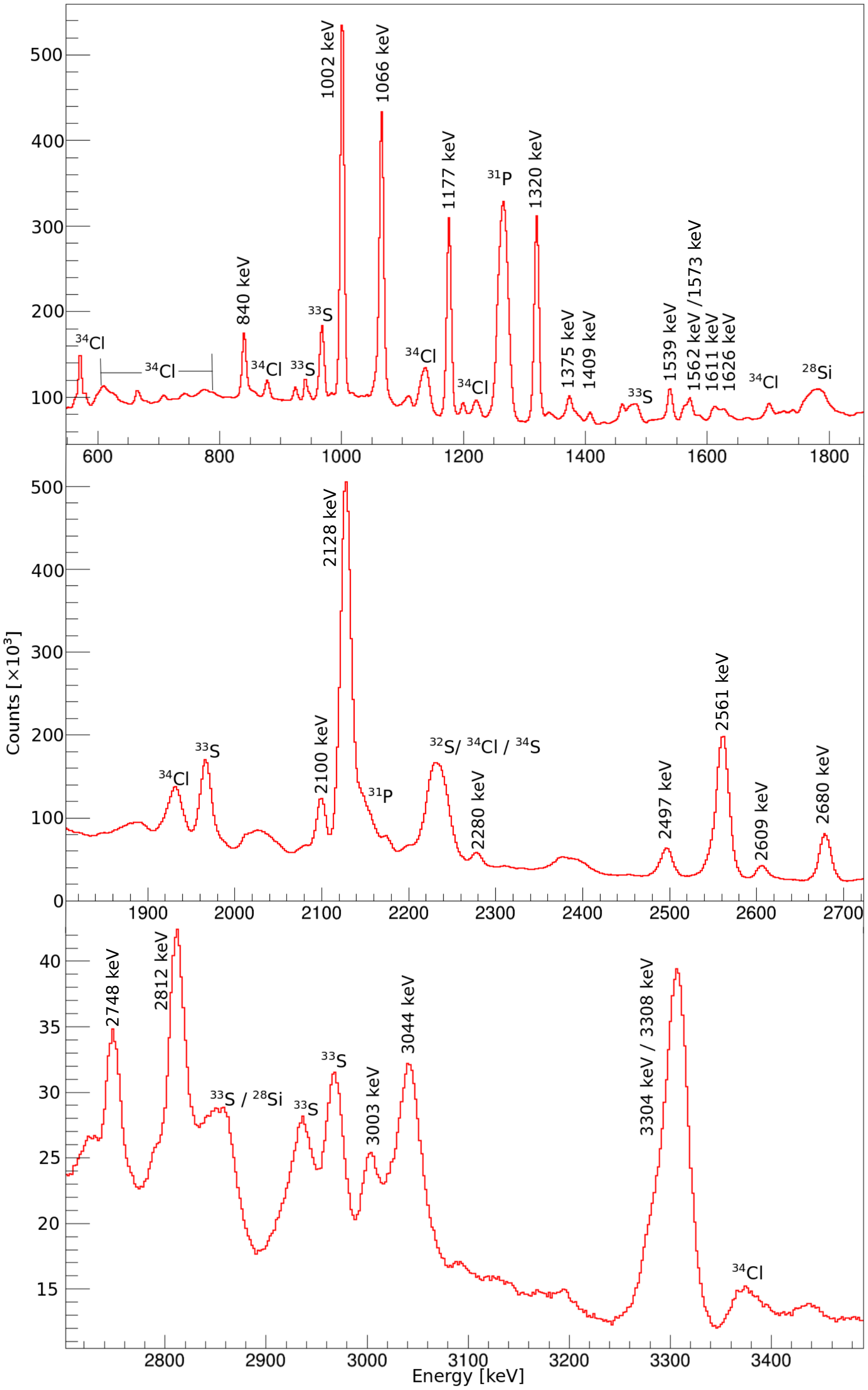

Figure 5.10: Particle gated γ-ray spectrum for ^{34}S concatenated from the entire experiment gated on $2p$ channel. There are contaminants visible throughout the spectrum. All labelled peaks are confirmed with Nuclear Data Sheets [38]. Unlabelled peaks are either contaminant peaks or heavily contaminated, making it difficult to identify its origin i.e. multiple contaminant peaks of various sources.

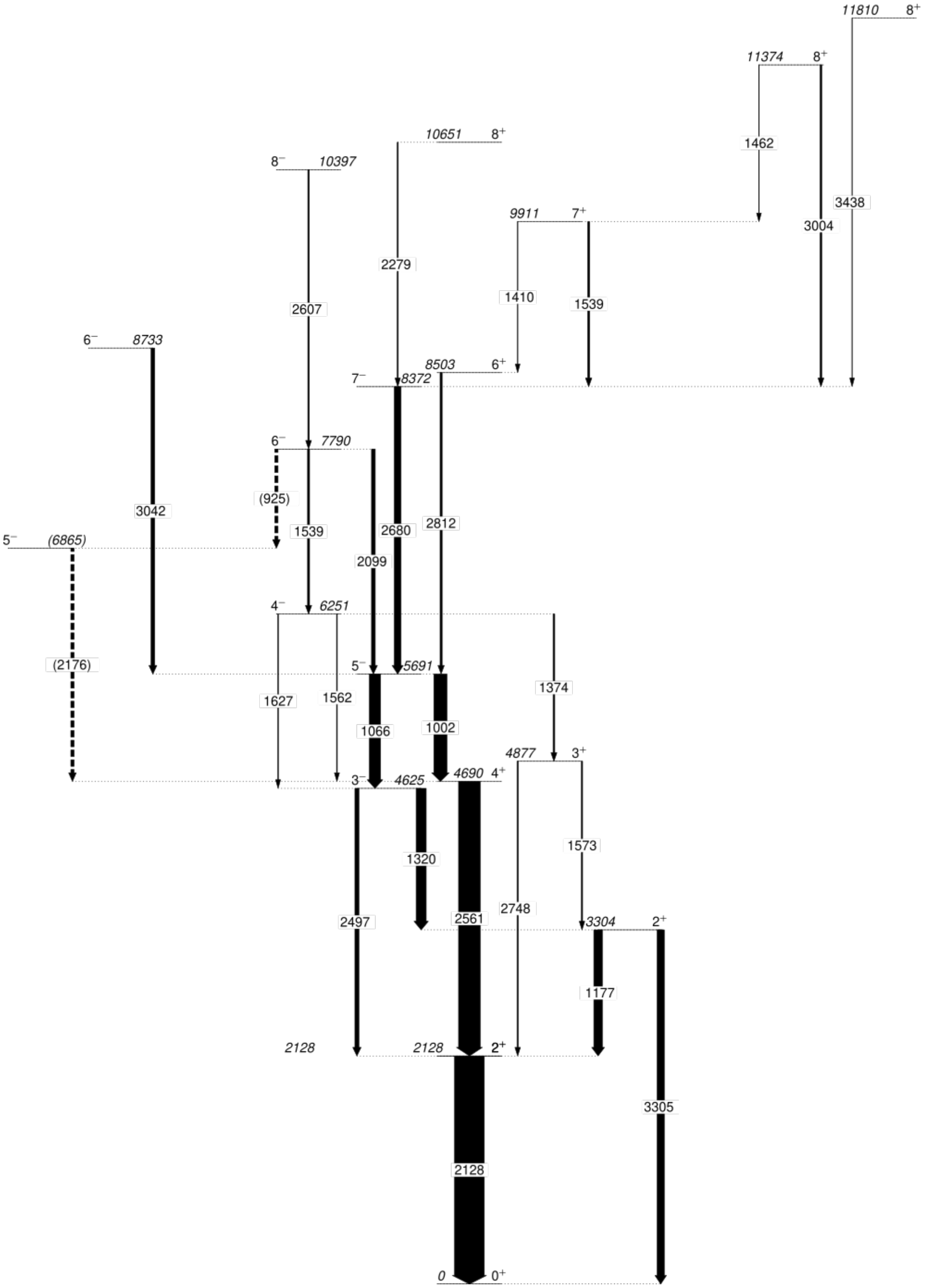

Figure 5.11: Partial level scheme of observed transitions in ^{34}S including transitions identified in this work. Transition intensities are proportional to the width of the arrows. Transitions denoted with dashed lines were observed using the coincidence method, and the placement of the 925-keV transition is discussed in Section 5.6

Table 5.1: Transitions from the $2p$ gated γ-ray spectra are shown. Due to the highly contaminated nature of the intense 2128-keV, highlighted with *, a comparison to Mason *et al.* is done by normalizing the relative intensity of the 2561-keV transition to 67.5% as in Reference [1]) . Transitions highlighted in red fail to replicate the results in the previous work, highlighting possible differences in the population of energy levels.

Transition	$\mathbf{E_{transition}}$ **[keV]**	$\mathbf{I_{Exp}}$ [%]	I_{Lit} [%]
$\mathbf{5^- \rightarrow 4^+}$	1001.6(3)	41(4)	42(4)
$\mathbf{5^- \rightarrow 3^-}$	1066.5(4)	34.8(10)	35(4)
$\mathbf{2_1^+ \rightarrow 2^+}$	1176.6(15)	27(3)	22(2)
$\mathbf{3^- \rightarrow 2^+}$	1320.4(3)	31(8)	27(3)
$\mathbf{4^- \rightarrow 3^+}$	1374.5(7)	5(3)	2.8(6)
$\mathbf{7^+ \rightarrow 6^+}$	1409.5(8)	1.32(8)	2.1(6)
$\mathbf{8_1^+ \rightarrow 7^+}$	1461.6(5)	1.3(3)	3.7(8)
$\mathbf{6^- \rightarrow 4^-}$	1538.9(8)	6.1(5)	5.0(10)
$\mathbf{4^- \rightarrow 4^+}$	1561.6(3)	2.3(10)	2.9(6)
$\mathbf{3^+ \rightarrow 2_1^-}$	1572.7(5)	3.6(2)	3.2(7)
$\mathbf{4^- \rightarrow 3^-}$	1627.3(12)	1.9(2)	1.3(3)
$\mathbf{6^- \rightarrow 5^-}$	2099.1(16)	11.5(12)	27(3)
$\mathbf{2^+ \rightarrow 0^+}$	2128.0(9)	93(13)*	100
$\mathbf{8^+ \rightarrow 7^-}$	2279.3(10)	3.2(5)	4.7(10)
$\mathbf{3^- \rightarrow 2^+}$	2497.0(7)	12.4(10)	12.3(12)
$\mathbf{4^+ \rightarrow 2^+}$	2561.0(7)	67.5	68(7)
$\mathbf{8^- \rightarrow 6^-}$	2607.0(10)	4.6(10)	7.1(10)
$\mathbf{7^- \rightarrow 5^-}$	2680.4(11)	21(4)	30(3)
$\mathbf{3^+ \rightarrow 2^+}$	2748.5(9)	3.7(10)	3.6(8)
$\mathbf{6^+ \rightarrow 5^-}$	2812.0(10)	6.3(5)	7.7(14)
$\mathbf{8^+ \rightarrow 7^-}$	3004(3)	4.8(14)	4.1(8)
$\mathbf{6_1^- \rightarrow 5^-}$	3042(2)	10(20)	3.1(7)
$\mathbf{2_1^+ \rightarrow 0^+}$	3305(3)	22(4)	17.8(18)
$\mathbf{8_2^+ \rightarrow 7^-}$	3437.6(8)	1.0(2)	1.5(6)

Table 5.2: Comparison of γ-ray branching ratios from energy levels observed in ^{34}S against literature values [38].

$\mathbf{E_{initial}}$ **[keV]**	$\mathbf{J_i}$	$\mathbf{E_{final}}$ **[keV]**	$\mathbf{J_f}$	$\mathbf{E_{transition}}$ **[keV]**	**I [%]**	$\mathbf{I_{NNDC}}$ **[%]**
4624.6(10)	$\mathbf{3^-}$	3304.0(10)	$\mathbf{2_1^+}$	1320.4(3)	100	100
		2128.1(9)	$\mathbf{2^+}$	2497.0(7)	33(3)	41(6)
4877.0(10)	$\mathbf{3^+}$	3304.0(10)	$\mathbf{2_1^+}$	1572.3(4)	86(5)	80(12)
		2128.1(9)	$\mathbf{2^+}$	2748.5(9)	100	100
5691.1(10)	$\mathbf{5^-}$	4689.5(10)	$\mathbf{4^+}$	1001.6(3)	100	100
		4624.6(10)	$\mathbf{3^-}$	1066.5(4)	76(4)	83(13)
6251.2(10)	$\mathbf{4^-}$	4877.0(10)	$\mathbf{3^+}$	1374.5(7)	52(3)	46(15)
		4689.5(10)	$\mathbf{4^+}$	1561.6(3)	100	100
7790.1(12)	$\mathbf{6^-}$	6251.2(10)	$\mathbf{4^-}$	1538.9(8)	15(2)	19(5)
		5691.1(10)	$\mathbf{5^-}$	2099.1(16)	100	100

5.5.2 ^{34}Cl — *pn* Reaction Channel

To validate that the neutron wall functions as intended, γ rays associated with the decay of ^{34}Cl are studied as it is one of the more populous channels that utilizes both neutron coincidences as well as charged particle coincidences. The γ-ray spectra corresponding to this reaction channel validates both particle detector arrays and serves as another step in confirming every detector works before moving on to less intense channels. Energy levels associated with ^{34}Cl are observed up to 11 MeV. The measured branching ratios are compared with the ENSDF for ^{34}Cl, from which the experimental results were determined to be within agreement as shown in Table 5.3. One new transition at 2288 keV was observed decaying from a new energy level at 10093 keV. Due to the complexity of the level scheme of ^{34}Cl, there was often a lack of statistics to confirm relative intensities using $pn-\gamma$ coincidences like in the case of ^{34}S. In addition, there was no experiment with a broadly comparable setup. As such, the relative branching ratios are used to verify the validity of this reaction channel.

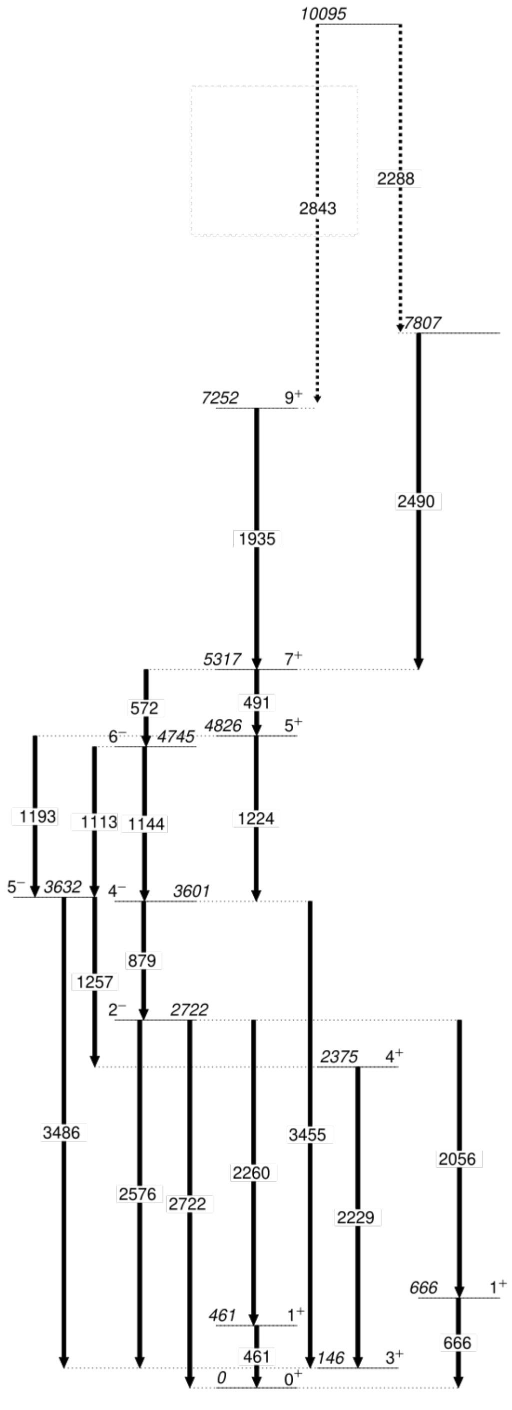

Figure 5.12: Level scheme of observed transitions in ^{34}Cl. Transitions are primarily those highlighted in Table 5.3. Intensities are not highlighted in the level scheme due to contamination for many transitions. Transitions denoted by dashed lines are the previously unreported 2288-keV transition, and the 2843-keV transition which was reassigned above the 1935-keV transition as discussed in Section 5.6.

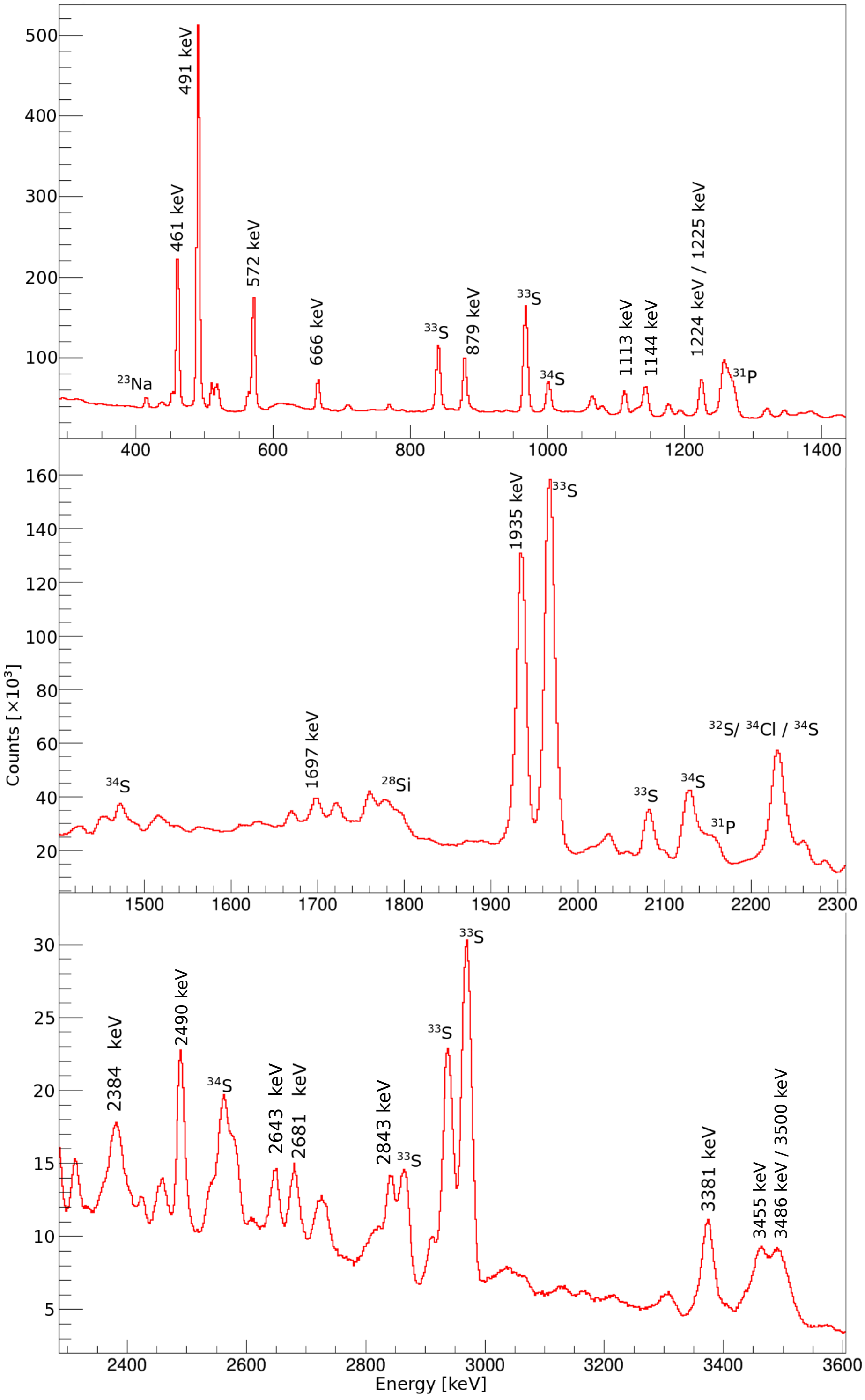

Figure 5.13: Particle gated γ-ray spectrum for ^{34}Cl from all the runs over the experiment's run. All labelled peaks are confirmed with Nuclear Data Sheets [38].

Table 5.3: Comparing branching ratios of γ rays from energy levels observed in ^{34}Cl against known values [38]. Transitions and energy levels were verified using the coincidence method described in Section 5.4.

$\mathbf{E_{initial}}$ **[keV]**	$\mathbf{J_i}$	$\mathbf{E_{final}}$ **[keV]**	$\mathbf{J_f}$	$\mathbf{E_{transition}}$ **[keV]**	**I [%]**	$\mathbf{I_{NNDC}}$ **[%]**
2721.7(8)	$\mathbf{2^-}$	665.8(8)	$\mathbf{1^+_1}$	2056.0(11)	15.9(18)	16(9)
		461.2(8)	$\mathbf{1^+}$	2260.4(7)	100	100
		145.9(12)	$\mathbf{3^+}$	2575.1(9)	43(2)	39.1(11)
		0	$\mathbf{0^+}$	2721.7(16)	29(2)	32.9(14)
3632.2(12)	$\mathbf{5^-}$	2375.1(17)	$\mathbf{4^+}$	1257(2)	100	100
		145.9(12)	$\mathbf{3^+}$	3486(2)	73(8)	84(5)
4745(1)	$\mathbf{6^-}$	3632.2(10)	$\mathbf{5^-}$	1112.8(3)	77(4)	84(7)
		3601.0(10)	$\mathbf{4^-}$	1144.1(3)	100	100
5316.2(12)	$\mathbf{7^+}$	4825.6(11)	$\mathbf{5^+}$	491.1(3)	100	100
		4745.0(10)	$\mathbf{5^+}$	571.9(5)	33.2(11)	35.0(11)
10094.1(15)		7806.6(13)		2288.0(5)	37(5)	-
		7251.8(13)	$\mathbf{9^+}$	2842.8(8)	100	-

5.6 Establishing Newly Observed Transitions

New transitions were observed in both ^{34}S and ^{34}Cl using $\gamma - \gamma$ coincidences.

Using these $\gamma - \gamma$ matrices, the 6$^-$→5$^-$ 925 keV in ^{34}S was placed in coincidence with the 4$^+$→2$^+$ 2561-keV transition as well as the 5$^-$→4$^+$ 2176-keV transition as shown in Figure 5.14 whilst not being present in the ^{34}Cl gated spectra with a cascade containing similar transition energies.

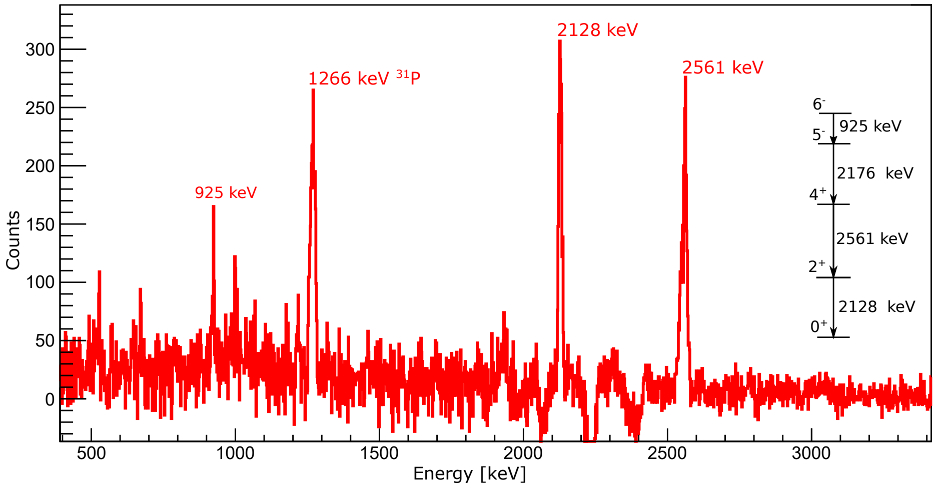

Figure 5.14: A gate on the 5$^-$→4$^+$ 2176 keV as well as the $2p$ channel highlighting the 925-keV transition.

In a similar vein, the newly identified ^{34}Cl transitions are observed after trying to verify the 2843-keV transition observed by Bisoi *et al.* [2]. However the 2843-keV transition is clearly visible in Figure 5.15 when gating on the 1935-keV transition which suggests a new placement of the transition. As such the transition is moved and a new energy level assigned. When gating on the 2490-keV transition, a new 2288-keV γ-ray transition is observed as shown in Figure 5.16. The latter transition is tentatively placed at the same 10093-keV energy level that feeds the aforementioned 2843-keV transition.

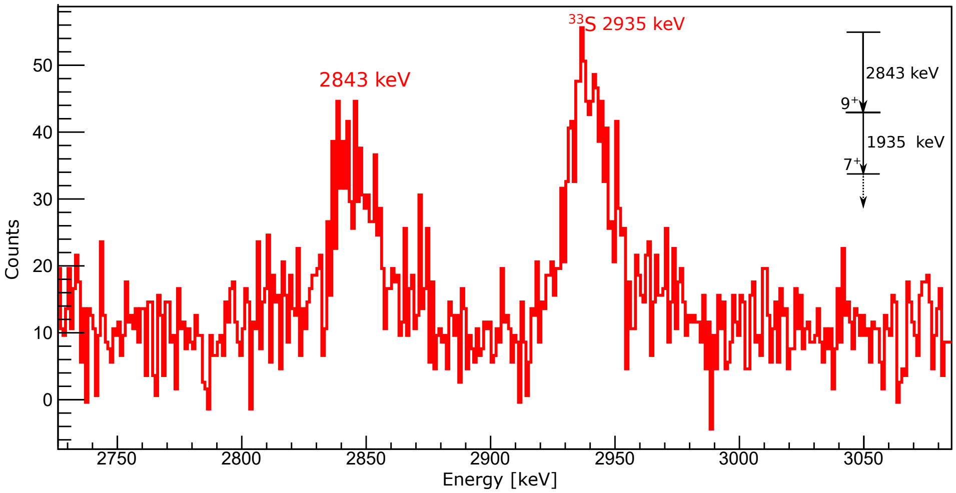

Figure 5.15: Gating on the 1935-keV transition and the *pn* channel to highlight the observed 2843-keV peak which should not be present within this gate according to the work of Bisoi *et al.*[2]. The 2935-keV transition is a possible contaminant from ^{33}S, although other gates in the *pn* channel also show the same peak without any other contaminant peaks.

5.7 Alpha Channels

Examining the coincidences between EUCLIDES and GALILEO proved fruitful for the $2p$ channel. However, there are some problems when examining coincidences between α particles and γ rays. With an estimated cross-section of 104 mb for the 2α channel associated with ^{28}Si and 36.2 mb for the 1α channel associated with ^{32}S, gating on α particles should prove just as fruitful as trying to observe transitions for ^{34}S and ^{34}Cl.

The $4^+ \rightarrow 2^+ \rightarrow 0^+$ transitions for ^{28}Si are clearly visible in the 2α channel. As a matter of fact, both the 1779-keV $2^+ \rightarrow 0^+$ transition as well as the 2838-keV $4^+ \rightarrow 2^+$ transition often appear as contaminants in other spectra. Unfortunately, the efficiency of the GALILEO γ-ray detectors beyond 3 MeV becomes increasingly small whilst the majority of transitions in ^{28}Si are higher in energy, serving to complicate building a level scheme for ^{28}Si due to the low statistics from $\gamma - \gamma$ matrices.

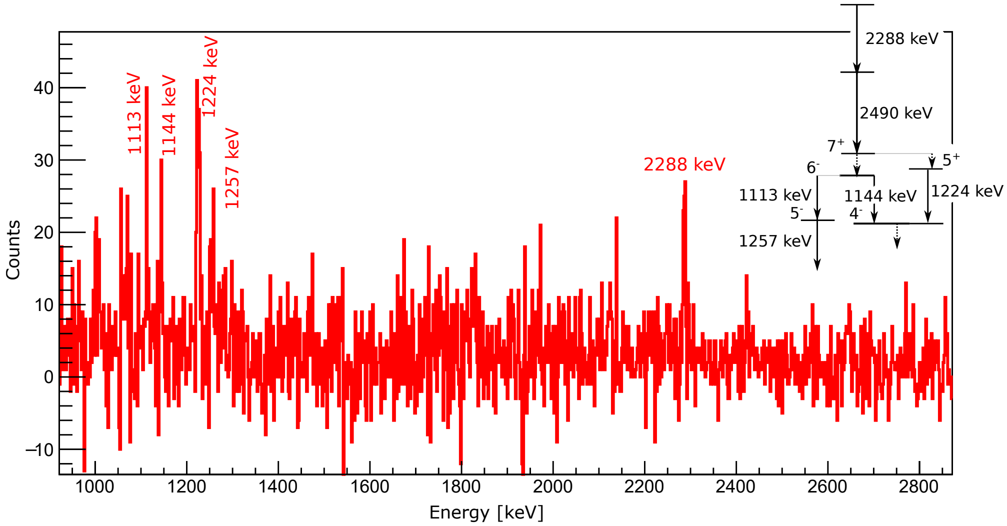

Figure 5.16: A gate is drawn on the 2490-keV transition and the *pn* channel: a 2288-keV transition is observed that has not been placed.

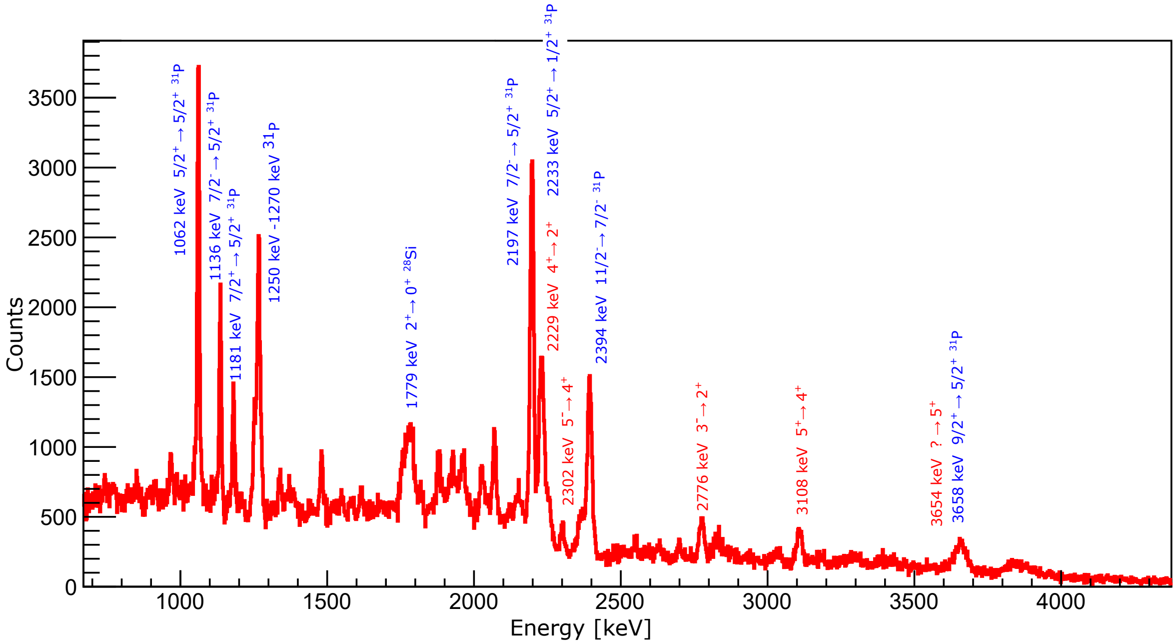

Figure 5.17: Coincidence γ-ray spectrum gated on the 2230-keV doublet and the 1α gate. All transitions in red correspond to known ^{32}S nuclei, whilst every transition in blue are contaminant peaks present.

Focusing on the α channel associated with ^{32}S, a gate can be applied to the 2230-keV $2^+ \rightarrow 0^+$ transition, although intensity information is less useful in this case as it shares the same gate as the 2229-keV $4^+ \rightarrow 2^+$ transition [39] due to the inability of the GALILEO detectors to isolate the two transitions. As shown in Figure 5.17, contamination peaks that appear before can be exacerbated when multiple transitions correspond to the applied energy gate. In this case, not only is the $4^+ \to 2^+$ transition from ^{32}S found at 2229 keV, but transitions from ^{31}P and ^{34}Cl have energies consistent with the applied energy gate. In contrast, a gate on the 2776-keV $3^- \to 2^+$ transition shown in Figure 5.18 shows much less contamination as the 2776-keV transition is well isolated.

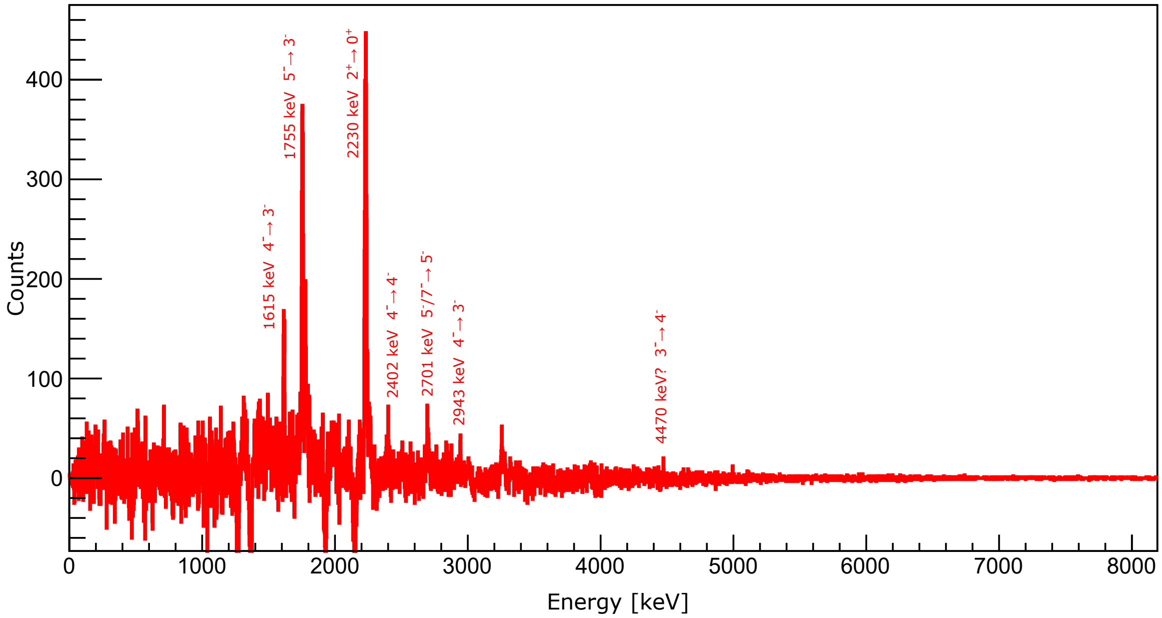

Figure 5.18: Coincident γ-ray spectrum gating on the 2776-keV transition and the 1α particle gate. Contamination is heavily suppressed when no contaminant channels share the same transition energy as the gate of interest.

It was not possible to completely isolate specific reaction channels from other channels which were strongly produced using only the gated applies to the EUCLIDES detector. However, for reaction channels which were produced with sufficient statistics, it was possible to examine the channels by further including γ-γ coincidences, as evidenced in Section 5.5.1 and 5.5.2.

5.8 Neutron Channels

The level schemes reproduced in ^{34}S and ^{34}Cl confirms the validity of the kinematic reconstruction. This confidence with the event-by-event kinematic reconstruction can then be translated to an averaged Doppler correction to use on the neutron channels as discussed in Section 5.1.3.

The limitations of the low cross section of the channel of interest become apparent when examining neutron-gated γ-ray spectra. When overlapping spectrum from the pn channel with the neutron channels, the peaks observed are almost identical as shown in Figure 5.19. This can be taken a step further, examining the $2^+ \to 0^+$ transition for ^{34}Ar given at 2091 keV [23]. Given that this transition is strong in the ^{34}S mirror nucleus, the intensity should be similarly pronounced in ^{34}Ar. However, when looking at the particle gated spectrum in Figure 5.20, the known energy of the transition is buried under a ^{33}S peak $9/2^+ \to 5/2^+$ given at 2082 keV. Similarly, no transitions listed on the NNDC for ^{34}Ar are present [38].

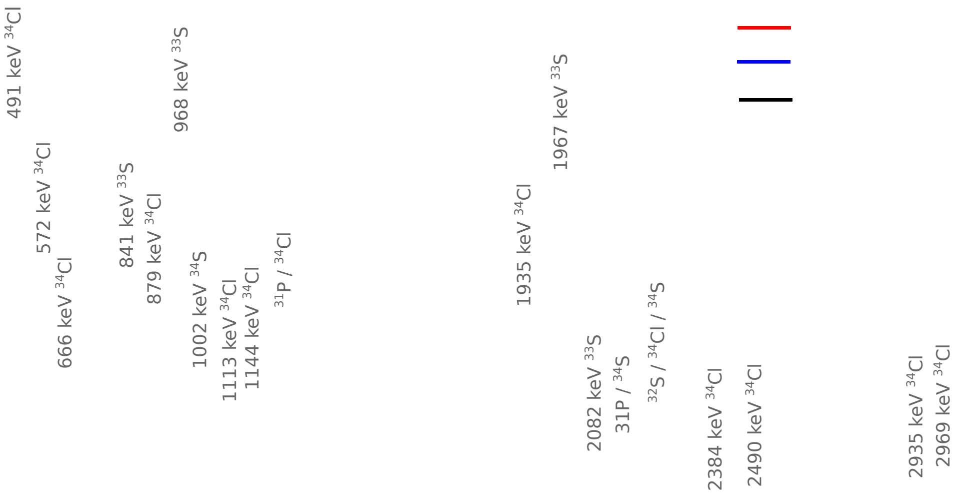

Figure 5.19: Comparison of the pn (shown in blue) channel as well as the $2n$ (shown in red) channel and a more general subtraction (shown in black) of the full spectrum to remove all proton and alpha events.

Further attempts to identify transitions in ^{34}Ar are performed using $\gamma-\gamma$ coincidences. Here an energy gate is applied at the energy of the $2^+ \to 0^+$ transition in ^{34}Ar. The matrix used is based on a general subtraction of the neutron channel using the charged particle channels, as this yielded about an order of magnitude more counts without any noticeable loss of data on transitions. From the original $2n$ gated spectrum, charged particle spectra are scaled to match the 1967-keV contaminant transition, associated with ^{33}S, in the neutron gated

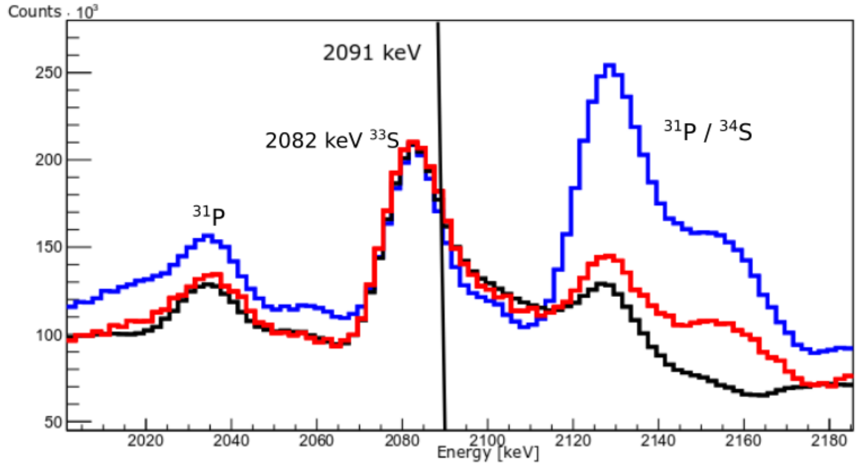

Figure 5.20: The comparison of the particle gated spectra of *pn* (shown in blue), $2n$ (shown in red), and the general subtraction (shown in black) zoomed in around where the expected ^{34}Ar $2^+ \rightarrow 0^+$ transition is expected to be. This last general subtraction is discussed further in the text.

spectrum and then subtracted from the neutron gated spectrum. As many of the peaks are large, the process can be overdone resulting in a spectrum with purely negative peaks that may bury the transitions of interest, so some discretion was used to limit the subtractions such that no negative peaks are highly visible as shown in the black spectrum of Figure 5.20. The same set of subtractions is then applied to the neutron-gated γ-γ coincidence matrix, and the gate around 2091-keV transition is created.

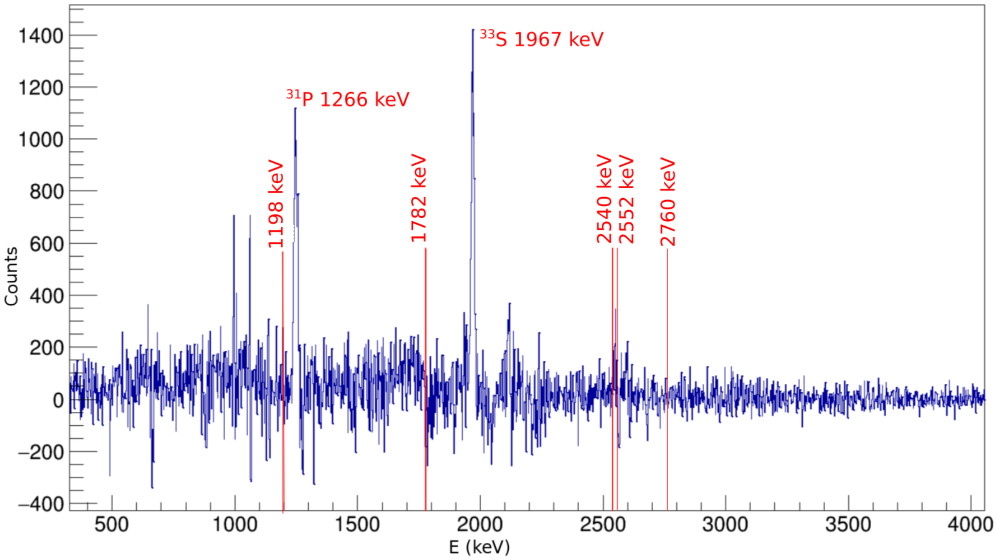

Figure 5.21: A γ-ray spectrum based on general subtraction gated around 2091 keV with background subtracted showcasing lack of known ^{34}Ar transitions. Peaks shown are common contaminants from ^{33}S and ^{31}P.

The result of this gate is shown in Figure 5.21. Highlighted in red are transitions found in ^{34}Ar coincident with the 2091-keV transition [38]. Given that none of the transitions expected are present and that the peaks seen correspond with ^{33}S, finding any transitions of ^{34}Ar would be relegated to guess work.

5.8.1 Comparison to Separate Experiment at Argonne

Although it was not possible to identify transitions corresponding to ^{34}Ar in this work, a recent experiment at Argonne National Labs did isolate ^{34}Ar in sufficient quantities to obtain spectroscopic results. This was done using the reaction ^{24}Mg(^{12}C,2n)^{34}Ar using a 95 MeV ^{24}Mg beam, which is the reverse kinematics case of the one conducted in this work. We can begin to compare the two reactions by examining the Q value, which is shown in Equation 5.8:

$$Q = (m_r - m_p)c^2 \tag{5.8}$$

where m_r is the total rest mass of reactants and m_p is the total rest mass of the products. As the target/beam combination is the same in both experiments, as well as the compound nucleus produced, the Q value for the reactions are identical. A comparison of the reaction mechanisms as calculated using PACE4 is shown in Table 5.4.

Using PACE4, the calculated reaction cross section for ^{34}Ar is approximately three times larger for the projectile and target combination used in the Argonne experiment compared to this work. The experiment at Argonne, which employed a ^{24}Mg beam at 95 MeV bombarding a ^{12}C target produces a compound nucleus, ^{36}Ar, with an excitation energy of 48 MeV. This is larger than the 39.6-MeV excitation energy produced from the ^{12}C beam at 35 MeV bombarding a ^{24}Mg target that was employed in this work. Consequently, this higher excitation energy contributes to the higher calculated reaction section for the Argonne experiment. The 0.2 mg/cm^2 ^{12}C target combined with the 15 pnA beam current [24] also produced a higher production rate of ^{34}Ar events when using PACE4 calculations for the reaction cross sections, compared with the 0.5 mg/cm^2 ^{24}Mg target and 8 pnA beam current used in Legnaro. Furthermore, the experiment by Reference [24] utilized the Argonne Fragment Mass Analyzer, which enabled the authors to isolate $A = 34$ nuclei from the other reaction channels. Finally, the comparatively larger detection efficiency of GRETINA – the efficiency given for GALILEO at 1.3 MeV is 1.9% versus the 10% efficiency at the same energy for GRETINA in use at Argonne – it is entirely possible that a mixture of running at low energies and the lower efficiency result in ^{34}Ar being obscured in the 2015 experiment. A summary of the comparisons discussed is shown in Table 5.5.

Table 5.4: PACE4 calculations run using 100000 events to show cross sections of different channels opened in the Argonnne experiment with a 95 MeV ^{24}Mg beam on ^{12}C target. Compared to Table 4.1, which is summarized in the last column, the overall reaction cross section is similar, whilst the reaction cross section for producing ^{34}Ar is notably higher when using the setup at Argonne.

Z	**N**	**A**	**Percent of Events Argonne** [%]	**Cross-section Argonne** [mb]	**Cross-section LNL** [mb]
18	18	^{36}Ar	0.0037	0.04	-
18	17	^{35}Ar	0.0443	0.479	4.51
17	18	^{35}Cl	0.03	0.324	6.43
18	16	^{34}Ar	0.0775	0.837	0.21
17	17	^{34}Cl	3.5	48.6	131
16	18	^{34}S	2.73	29.5	95.3
17	16	^{33}Cl	0.367	3.97	0.0956
16	17	^{33}S	18.2	197	55
15	18	^{33}P	1.19	12.8	2.95
16	16	^{32}S	0.44	4.75	36.2
16	15	^{31}S	4.03	43.5	28.1
15	16	^{31}P	29.3	317	487
15	15	^{30}P	10.2	111	0.65
14	16	^{30}Si	3.25	35.1	0.115
14	15	^{29}Si	0.184	1.98	-
14	14	^{28}Si	12.4	134	104
14	13	^{27}Si	0.164	1.77	-
13	14	^{27}Al	12.8	138	4.66
12	12	^{24}Mg	0.0173	0.187	-

Table 5.5: Summary of the comparison between the experimental setup at Argonne National Laboratory and at Laboratori Nazionali di Legnaro. The experiment at Argonne managed to produce ^{34}Ar events in larger amounts when considering PACE4 calculations, highlighted by the production rate of ^{34}Ar, $N(^{34}\text{Ar})$, as well as having a higher detection efficiency for such events.

	Argonne	**LNL**
Experiment	^{12}C(^{24}Mg,2n)^{34}Ar	^{24}Mg(^{12}C,2n)^{34}Ar
Beam Energy	95 MeV	35 MeV
Target Thickness	0.2 mg/cm^2	0.5 mg/cm^2
Channel Selection	FMA + Ionization Chamber	Si telescopes + Neutron wall
ϵ_γ(1332 **keV**)	10 %	1.9 %
PACE4 $\sigma(^{34}\mathbf{Ar})$	0.84 mb	0.21 mb
$E_{ex}(^{36}\mathbf{Ar})$	48 MeV	40 MeV
$N(^{\mathbf{34}}\mathbf{Ar})$	789 s^{-1}	132 s^{-1}
Run Time	140 hours	116 hours

5.9 Establishing Lower Detection Limit for ^{34}Ar Peak Intensities

The observation of the $2^+ \rightarrow 0^+$ 2091-keV transition from ^{34}Ar could not be determined with any degree of certainty in this work. To illustrate, the singles spectrum for the $2n$ channel associated with ^{34}Ar is shown in Figure 5.22, where transitions from contaminants are used to define a lower detection limit. To observe the 2091-keV transition from ^{34}Ar, the intensity of the peak should be on the order of 10^4 and would be similar to the nearby 2082-keV contaminant transition from ^{33}S, which was observed with 4.69×10^4 counts.

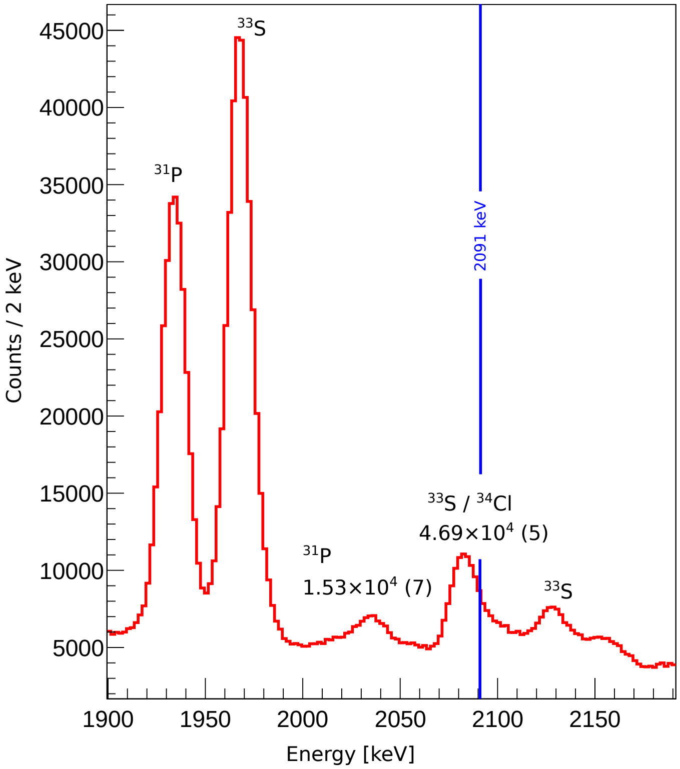

Figure 5.22: The $2n$ gated spectrum highlighting the location of the $2^+ \rightarrow 0^+$ 2091-keV transition of ^{34}Ar. Contaminants from other channels heavily populate the $2n$ channel such that no ^{34}Ar transition is seen.

The experiment at Legnaro was conducted using a 35-MeV ^{12}C beam with an average intensity, i_{beam}, of 8.42 pnA over a time period, Δt, of 116 hours and 26 minutes (4.192×10^5 seconds). The ^{24}Mg target thickness, δ_{target}, is given as $0.5\,\text{mg/cm}^2 = 1.253 \times 10^{19}\,\text{atom} \cdot \text{cm}^{-2}$. The efficiency of GALILEO, $\epsilon_\gamma(E_i)$, was 1.41(2) % at 2091 keV from measured efficiency curves, whilst the efficiency of the Neutron Wall, ϵ_n, was measured as 19.3(16)%. The reaction cross section of the $2n$ channel calculated by PACE4, $\sigma_{2n}^{\text{PACE4}}$, is 200 μb. An assumption

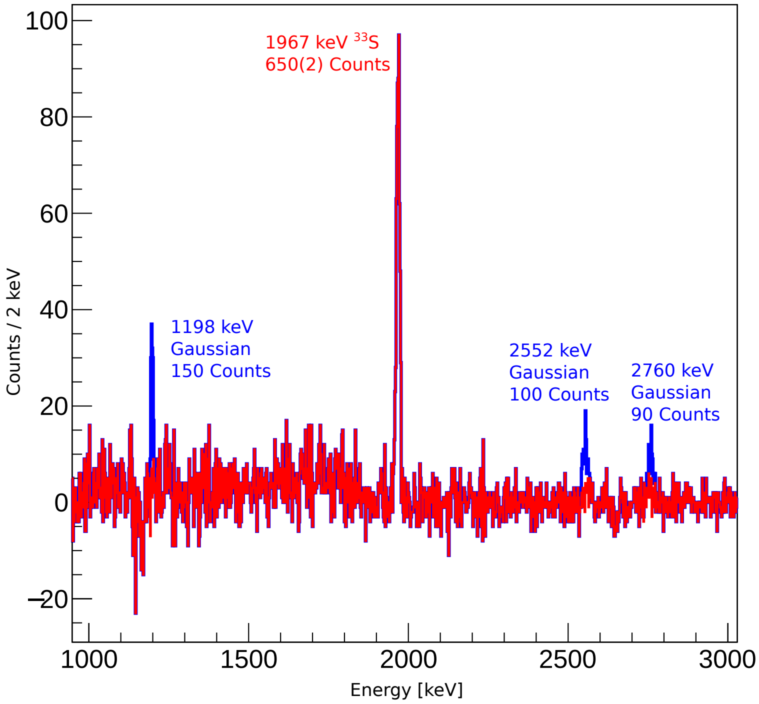

Figure 5.23: The experimental γ-ray spectrum, shown in red, gated on the $2n$ channel as well as around the location of the 2091-keV transition, is plotted with the locations of several feeding transitions: $2_2^+ \to 2_1^+$ 1198-keV, $4^+ \to 2_1^+$ 2552-keV, and $3^+ \to 2_1^+$ 2760-keV, highlighted. A Gaussian is drawn, in blue, around each transition energy to estimate how many counts are needed for the peak to be visible above the background.

was also made that the 2091-keV transition is the only one that feeds the ground state of ^{34}Ar. The estimated intensity of the 2091-keV peak, N, is calculated in Equation 5.9.

$$\begin{aligned} N &= \sigma i_{beam} \delta_{target} \Delta t \epsilon_\gamma(E_i) \epsilon_n^2 \\ &= \sigma_{2n}^{(\text{PACE4})}(8.42\text{ pnA})(1.253 \times 10^{19}\,\text{cm}^{-2})(116\,\text{h})(0.01409)(0.193)^2 \\ &= (2 \times 10^{-28}\,\text{cm}^2)(5.255 \times 10^{10}\,\text{s}^{-1})(1.253 \times 10^{19}\,\text{cm}^{-2})(4.192 \times 10^5\,\text{s})(0.01409)(0.193)^2 \\ &= 2.9 \times 10^4 \text{ counts} \end{aligned} \tag{5.9}$$

The 2.9×10^4 counts estimated for the 2091-keV peak in the $2n$ channel should be comparable to the 4.69×10^4 counts in the 2082-keV peak from ^{33}S. Figure 5.22 does not show any significant peak at 2091 keV. Although the 2082-keV peak has a pronounced tail, suggesting a possible weak 2091-keV transition, a gate placed around 2091 keV reveals a spectrum with peaks characteristic to ^{33}S, without any trace of ^{34}Ar, as shown in Figure 5.23.

Equation 5.9 can also account for particle gated $\gamma - \gamma$ coincidence data. In the case of the $2n$ channel, additional considerations are required for: the efficiency of GALILEO at the coincident γ-ray energy, $\epsilon_\gamma(E^{(gate)})$, the relative intensity of the transitions feeding the energy level of the gated transition, I_{rel}, as well as an correction factor of $\epsilon_{\gamma-\gamma}$ to reflect that a γ-ray coincident event cannot be detected in the same detector. All of these factors are reflected in Equation 5.10.

$$N = \sigma i_{beam} \delta_{target} \Delta t I_{rel} \epsilon_\gamma(E_i) \epsilon_\gamma(E^{(gate)}) \epsilon_n^2 \epsilon_{\gamma-\gamma} \tag{5.10}$$

The relative efficiency uses γ-ray intensities from Ref. [24], with an upper bound error of $I_{rel} = 1$, signifying it is the sole transition feeding the energy of the gated transition, and a lower bound of $I_{rel} = 0.1$ as an estimate. The attenuation factor is given using $\epsilon_{\gamma-\gamma} = 24/25$ as the GALILEO detector array is comprised of 25 detectors. A summary of these calculations is shown in Table 5.6 for γ-ray events that should feed the 2091-keV 2_1^+ energy level in ^{34}Ar. Each coincident γ-ray event should be populated with at least 30 counts in the gated spectrum.

Table 5.6: Predicted intensities of ^{34}Ar transitions directly feeding the 2091-keV transition are shown in the fifth column, with the corresponding efficiency of GALILEO at that energy and the relative intensity taken from Ref. [24]. The last column contains the 2σ limit based off fits of the energy bins around each transition discussed in Appendix A.

Transition	**Energy [keV]**	ϵ_γ[%]	I_{rel}	**Counts** N	2σ **Limit**
$2_2^+ \to 2_1^+$	1198	2.03(2)	0.51	290^{+280}_{-240}	50
$4^+ \to 2_1^+$	2552	1.23(2)	0.34	120^{+230}_{-40}	71
$3^+ \to 2_1^+$	2760	1.16(2)	0.16	50^{+270}_{-20}	91

A gate placed around the location of the 2091-keV transition, shown in Figure 5.23, was placed to estimate the lower limit of detection within the gated projection. Gaussians with Full Widths at Half Maximums (FWHM) typical in the energy range are drawn using ROOT around transitions that feed the 2_1^+ 2091-keV energy level, with all three transitions chosen for their prominence in this gate according to the work of Kennington *et al.* [24]. A summary of the three transitions chosen is shown in Table 5.7. Compared with Table 5.6, it is likely that at least the 1198-keV peak would have been prominent, and the absence of the transition suggests ^{34}Ar was not produced in observable quantities in this experiment.

5.10 Measuring and Comparing Reaction Cross Sections from Experiment

Rearranging Equation 5.9 for σ allows the measurement of reaction cross sections from experimental data. The total number of a nuclei produced is determined using the sum of

Table 5.7: Summary of Gaussians drawn using ROOT's `FillRandom()` function around transition energies directly feeding the 2091-keV transition

Transition	**Energy [keV]**	**FWHM [keV]**
$2_2^+ \rightarrow 2_1^+$	1198	9
$4^+ \rightarrow 2_1^+$	2552	17
$3^+ \rightarrow 2_1^+$	2760	19

all γ-ray transitions which directly populate the ground state of a given nucleus, whilst correcting for both γ-ray and particle detector efficiencies. Three nuclei were selected: ^{31}P (αp channel) [40], ^{33}S ($2pn$ channel) [41], and ^{34}S ($2p$ channel) [1]. The nuclei were chosen due to their large predicted reaction cross sections for the given reaction mechanism and relatively simple ground-state feeding patterns with well separated energies and minimal background contamination. In addition, the peaks were fit without any specific GALILEO, EUCLIDES, or Neutron Wall coincidences. There is an added benefit in that bypassing particle detector coincidences also bypasses any error stemming from the efficiencies of EUCLIDES or the Neutron Wall. With this in mind, we will modify Equation 5.9 to ignore the efficiencies of the two particle detectors in Equation 2.18.

In addition to singles spectra, we can once again modify Equation 2.18 to account for particle gated spectra, gated around coincident γ rays with similar parameters. However, to fully account for all events feeding the transition shown in the γ-ray gate, the number of counts must represent all transitions directly feeding the gate. Equation 2.18 is thus modified to account for the attenuation factor $\epsilon_{\gamma-\gamma}$ as well as specifying $\epsilon_\gamma(E^{(gate)})$ to be the efficiency of GALILEO at the energy of the gating transition. In addition, the number of counts in a peak, $N(E_i)$, must be considered with the corresponding efficiency of GALILEO at that energy, $\epsilon_\gamma(E_i)$. The particle gated spectra also require the specific detector efficiencies of the particle gate, $\epsilon_{\alpha pn}$, which are listed on the top row of Table 5.8. The reaction cross section for a gate is thus shown in Equation 5.11. To find the total cross section for a reaction that is comparable to PACE4 calculations, a sum of each reaction cross section for a γ-ray transition that directly feeds the ground state is required, as shown in Equation 5.12. Example spectra used to calculate the cross sections for ^{34}S are shown in Figures 5.24 and 5.25.

$$\sigma^{(gate)} = \frac{1}{i_{beam}\delta_{target}\Delta t \epsilon_\gamma(E^{(gate)})\epsilon_{\gamma-\gamma}\epsilon_{\alpha pn}} \left(\sum_i \frac{N(E_i)}{\epsilon_\gamma(E_i)} \right) \tag{5.11}$$

$$\sigma = \sum_i \sigma_i^{(gate)} \tag{5.12}$$

Table 5.8: Particle detector efficiencies at Legnaro are listed in the first row. The efficiencies of the ^{34}Ar experiment, its proposal, and a ^{116}Ba experiment conducted around the same time [42] are also discussed later in this text. The latter experiment observed low efficiencies with the Neutron Wall.

Exp	ϵ_p [%]	ϵ_α [%]	ϵ_n [%]
LNL ^{34}Ar	31(2)	17(2)	19(2)
Proposal	60	35	20
LNL ^{116}Ba	28(4)	24(2)	~1.5

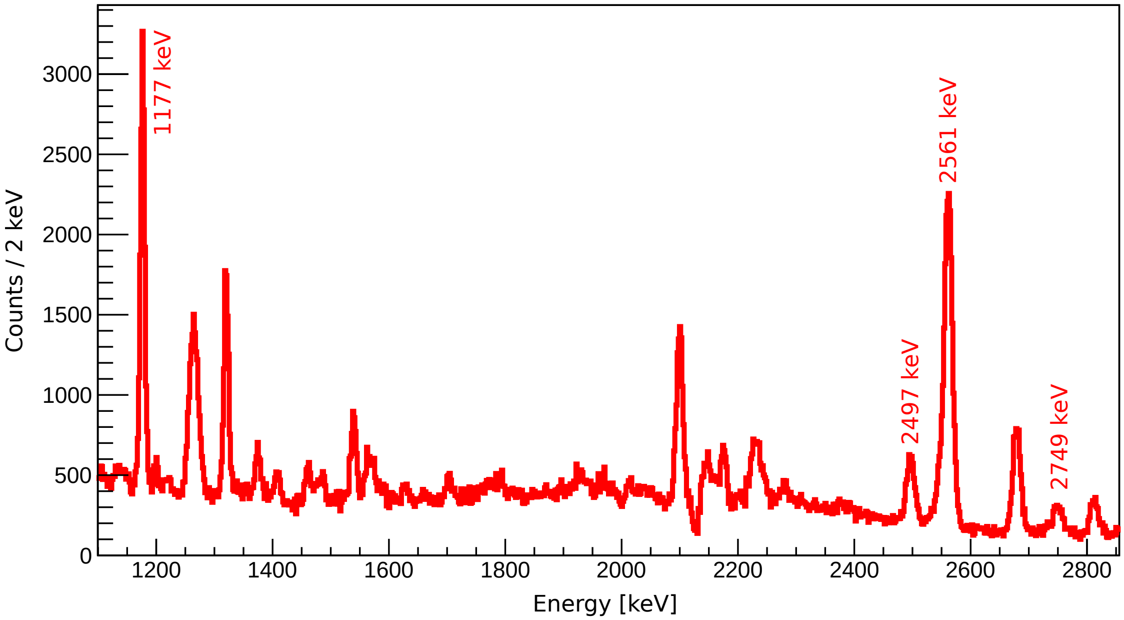

Figure 5.24: Gamma-ray spectrum constructed from the $2p$ channel gated around the $2_1^+ \to 0^+$ 2128-keV transition in ^{34}S. Transitions feeding 2128-keV level are labelled above. The intensities of these transitions are used in calculating reaction cross sections.

Comparisons between measured reaction cross sections and those obtained from PACE4 calculations, are shown in Table 5.9. The upper limit of detection for ^{34}Ar is given at 91 μb. This upper limit was established with a 2σ limit based on fitting the spectrum around expected transitions in Figure 5.23 and using Equations 5.11 and 5.12 to produce the associated reaction cross section. A summary of the 2σ limits is shown in the last column of Table 5.6, and a discussion on how 2σ limits were calculated can be found in Appendix A. The 2σ limit for the 2760-keV transition was chosen as it produces the highest reaction cross section. Overall, the experimentally obtained reaction cross sections were, on average, 14% of those calculated by PACE4.

Detector efficiencies are also examined to determine if the experimental setup deviates from what is expected. The proposal assumes the absolute γ-ray efficiency as 3.6% at 1332 keV,

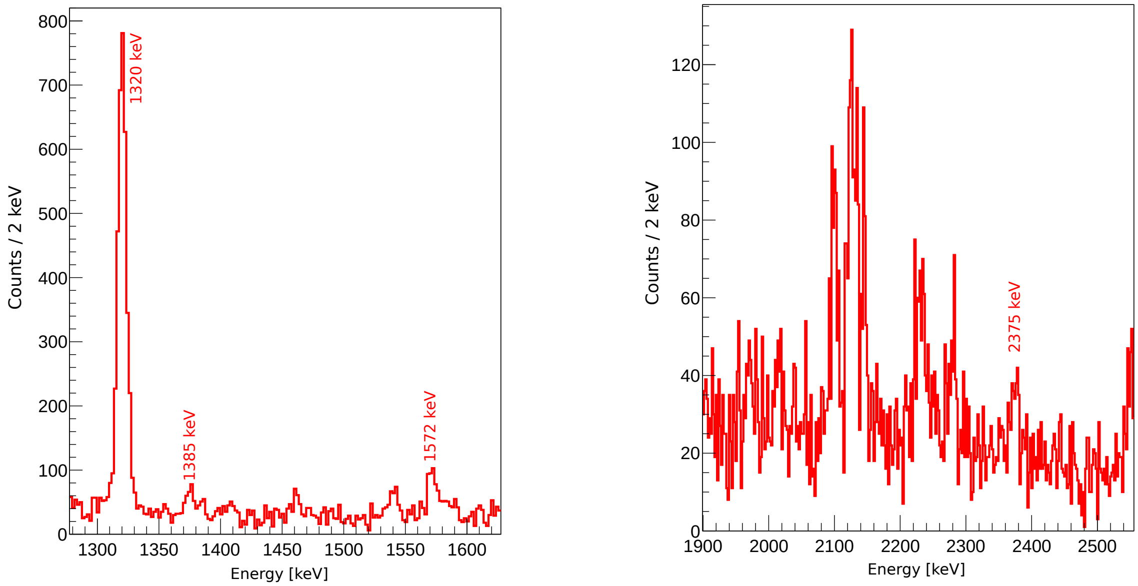

Figure 5.25: Gamma-ray spectrum constructed from the $2p$ channel gated around the $2^+_2 \rightarrow 0^+$ 3304-keV transition in ^{34}S. Transitions feeding 3304-keV level are labelled above. The intensities of these transitions are used in calculating reaction cross sections.

Table 5.9: Reaction cross sections for the experiment are compared with PACE4 calculations. The reaction cross sections from Legnaro are notably an order of magnitude lower than those predicted in singles and particle gated coincidence spectra.

		γ singles	$\alpha pn - \gamma - \gamma$
^{A}**X**	**σ PACE4 [mb]**	**σ Exp [mb]**	**σ Exp [mb]**
^{31}P	487	36(16)	25(8)
^{34}S	95.3	10(3)	9(2)
^{33}S	55	5.5(2)	-
^{34}Ar	0.21	-	< 0.091

which is higher compared to the measured experimental efficiency of 1.9% at 1332 keV. The particle detection efficiencies are also be compared in Table 5.8. The efficiencies of the detectors at Legnaro are not used in the calculation of the cross section from singles spectra for Table 5.9, but help reveal if any aspect of the experiment was unexpected. Although conditions are different, all values are within an order of magnitude and fail to be the sole contribution to the cross section discrepancy. The efficiency for neutron detection is low in the ^{116}Ba experiment, due to an issue with the detector and was not a cause of concern for the ^{34}Ar experiment.

Chapter 6

Conclusion

The study of mirror nuclei along the $N = Z$ line is important to investigate the behaviour of mirror symmetry in nuclei. The $A = 34$ nuclei presents itself as a good opportunity to explore this topic, with symmetry breaking contributions to the nuclear force being a particular point of interest. Theoretical shell model calculations have pointed to the $A = 34$ mirror nuclei as a possible region where current models do not match with available experimental data. To do such comparisons, the MED and TED for the nuclei are needed, relying on experimental data on transitions from ^{34}S, ^{34}Cl, and ^{34}Ar. Although ^{34}S and ^{34}Cl have been subject to extensive experimental study, ^{34}Ar is more experimentally challenging to access, and would benefit from additional study into its higher energy levels.

The experiment discussed in this work made use of the facilities available at the LNL, utilizing the GALILEO setup consisting of: an array of 25 Compton-suppressed HPGe detectors in concert with the EUCLIDES light charged particle Si telescope detectors as well as the neutron wall consisting of liquid scintillators. Conducted in 2015, a 35-MeV ^{12}C beam and a ^{24}Mg target was used to produce ^{34}Ar via the $2n$ channel through a fusion evaporation reaction. Before the analysis of the $2n$ channel, well studied reaction channels isolated by EUCLIDES were analyzed to verify the event-by-event kinematic reconstructions as well as the Doppler corrections.

The experiment conducted in October of 2015 was proposed with the aim of producing ^{34}Ar in sufficient quantities to observe its high spin states. Through the process of verifying that the experimental setup worked as intended—other nuclei including: ^{34}Cl, $^{32\text{-}34}$S, ^{31}P, and ^{28}Si were observed via γ-ray decay of energy levels with excitation energies up to 11 MeV—a new transition was observed in ^{34}S whilst a new transition and energy level was observed in ^{34}Cl. The issue of contamination between reaction channels was widely observed, where in certain cases like in the reaction channel associated with ^{34}S, there were as many ^{31}P nuclei detected as there were ^{34}S nuclei. Unfortunately, ^{34}Ar was not observed, with the presumably strong $2^+ \rightarrow 0^+$ being buried in a ^{33}S peak even after using the Neutron Wall and $\gamma - \gamma$ gating. The 2σ limit from particle gated $\gamma - \gamma$ coincidences suggest ^{34}Ar was produced in quantities less than 91 μb, which is much less than the 210 μb predicted from PACE4 calculations. The predicted reaction cross section for the experiment was still lower than the 837 μb obtained from PACE4 for the recently conducted experiment at Argonne which also aimed to produce ^{34}Ar. When compared with the experiment at Argonne, the differences in experiment kinematics and the lower efficiency of the γ-ray detectors at Legnaro might explain why the analysis of experimental data in this work failed to observe the $2n$ channel.

Further analysis of the ^{34}Ar channel is likely to be more fruitful with higher beam energies, as well as utilizing the reverse kinematic reactions used in the Argonne experiment. The GALILEO array's lower efficiency could be overcome using additional detectors from the old GASP array placed in the location of the neutron wall, thus sacrificing neutron channel discrimination for γ-ray efficiency. Conversely, the performance of the neutron wall could be improved, although as of the time of writing, there are no firm suggestions from the author on how this is achieved. In addition, developing methods for angular distribution analysis for the experimental setup would be useful for assigning these states. Although the experiment conducted fell short of its main aim, the lessons learned about the performance of experimental set up which is beneficial in developing proposals for future experiments.

Bibliography

[1] P. Mason, N. Mărginean, S. M. Lenzi, M. Ionescu-Bujor, F. Della Vedova, D. R. Napoli, T. Otsuka, Y. Utsuno, F. Nowacki, M. Axiotis, D. Bazzacco, P. G. Bizzeti, A. Bizzeti-Sona, F. Brandolini, M. Cardona, G. de Angelis, E. Farnea, A. Gadea, D. Hojman, A. Iordachescu, C. Kalfas, Th. Kröll, S. Lunardi, T. Martínez, C. M. Petrache, B. Quintana, R. V. Ribas, C. Rossi Alvarez, C. A. Ur, R. Vlastou, and S. Zilio. High spin structure of ^{34}S and the proton-neutron coupling of intruder states. *Phys. Rev. C*, 71:014316, Jan 2005.

[2] Abhijit Bisoi, M. Saha Sarkar, S. Sarkar, S. Ray, D. Pramanik, R. Kshetri, Somnath Nag, K. Selvakumar, P. Singh, A. Goswami, S. Saha, J. Sethi, T. Trivedi, B. S. Naidu, R. Donthi, V. Nanal, and R. Palit. High spin spectroscopy in ^{34}cl. *Phys. Rev. C*, 89:024303, Feb 2014.

[3] S.S. Zumdahl and S.A. Zumdahl. *Chemistry*. Cengage Learning, 2013.

[4] Alejandro Sonzogni and Benjamin Shu. Interactive chart of nuclides.

[5] J. J. Sakurai and Jim Napolitano. *Modern Quantum Mechanics*. Cambridge University Press, 2 edition, 2017.

[6] K. Heyde. *Basic Ideas and Concepts in Nuclear Physics: An Introductory Approach, Third Edition (Series in Fundamental and Applied Nuclear Physics)*. CRC Press, 3 edition, 7 2004.

[7] Maria Goeppert Mayer and J. Hans D. Jensen. *Elementary Theory of Nuclear Shell Structure*. John Wiley and Sons, Inc., 1955.

[8] R. A. Dunlap. *An Introduction to the Physics of Nuclei and Particles*. Thomson/Brooks-Cole, 2003.

[9] Kenneth S. Krane. *Introductory Nuclear Physics*. Wiley, 3 edition, 10 1987.

[10] K. K. Seth. Charge symmetry and charge independence. In Hans Volker Klapdor, editor, *Weak and Electromagnetic Interactions in Nuclei*, pages 619–629, Berlin, Heidelberg, 1986. Springer Berlin Heidelberg.

[11] K.L.G. Heyde. *The Nuclear Shell Model*. U.S. Government Printing Office, 1994.

[12] J. Ekman, D. Rudolph, C. Fahlander, A. P. Zuker, M. A. Bentley, S. M. Lenzi, C. Andreoiu, M. Axiotis, G. de Angelis, E. Farnea, A. Gadea, Th. Kröll, N. Mărginean,

T. Martinez, M. N. Mineva, C. Rossi-Alvarez, and C. A. Ur. Unusual isospin-breaking and isospin-mixing effects in the A = 35 mirror nuclei. *Phys. Rev. Lett.*, 92:132502, Apr 2004.

[13] C. Andreoiu, M. Axiotis, G. de Angelis, J. Ekman, C. Fahlander, E. Farnea, A. Gadea, T. Kröll, S.M. Lenzi, N. Mărginean, T. Martinez, M.N. Mineva, C. Rossi Alvarez, D. Rudolph, and C.A. Ur. First identification of excited states in ^{59}Zn. *Eur. Phys. J. A*, 15(4):459–462, 2002.

[14] J. Ekman, D. Rudolph, C. Fahlander, R.J. Charity, W. Reviol, D.G. Sarantites, V. Tomov, R.M. Clark, M. Cromaz, P. Fallon, A.O. Macchiavelli, M. Carpenter, and D. Seweryniak. The A = 51 mirror nuclei ^{51}Fe and ^{51}Mn. *The European Physical Journal A - Hadrons and Nuclei*, 9(1):13–17, Oct 2000.

[15] S M Lenzi and R Lau. A systematic study of mirror and triplet energy differences. *Journal of Physics: Conference Series*, 580(1):012028, 2015.

[16] R.D. Evans. *The Atomic Nucleus.* McGraw-Hill, Inc., 1955.

[17] G. Knoll. Radiation detection and measurement. *New York, John Wiley and Sons, Inc., 1979. 831 p.*, 01 2000.

[18] O. Klein and Y. Nishina. Über die streuung von strahlung durch freie elektronen nach der neuen relativistischen quantendynamik von dirac. *Zeitschrift für Physik*, 52:853, 1929.

[19] H. Ejiri and M. J. A. Voigt. *Gamma-ray and Electron Spectroscopy in Nuclear Physics.* Clarendon Press, 1989.

[20] F. Della Vedova, S. M. Lenzi, M. Ionescu-Bujor, N. Mărginean, M. Axiotis, D. Bazzacco, A. M. Bizzeti-Sona, P. G. Bizzeti, A. Bracco, F. Brandolini, D. Bucurescu, E. Farnea, A. Iordachescu, S. Lunardi, T. Martínez, P. Mason, R. Menegazzo, B. Million, D. R. Napoli, M. Nespolo, P. Pavan, C. Rossi Alvarez, C. A. Ur, R. Venturelli, and A. P. Zuker. Isospin symmetry breaking at high spin in the mirror nuclei ^{35}Ar and ^{35}Cl. *Phys. Rev. C*, 75:034317, Mar 2007.

[21] Christian Iliadis, Art Champagne, Jordi Jose, Sumner Starrfield, and Paul Tupper. The effects of thermonuclear reaction-rate variations on nova nucleosynthesis: A sensitivity study. *The Astrophysical Journal Supplement Series*, 142(1):105–137, sep 2002.

[22] C.J. Van Der Poel, G.A.P. Engelbertink, H.J.M. Aarts, D.E.C. Scherpenzeel, H.F.R. Arciszewski, and B.C. Metsch. High-spin states in 34cl. *Nuclear Physics A*, 373(1):81 – 108, 1982.

[23] T.K. Alexander, G.C. Ball, D. Horn, J.S. Forster, I.V. Mitchell, and H.-B. Mak. Lifetime measurements of levels in ^{34}Ar: Isoscalar and isovector matrix elements for E2 analogue transitions. *Nuclear Physics A*, 444(2):285 – 302, 1985.

[24] A. R. L. Kennington, G. Lotay, D. T. Doherty, D. Seweryniak, C. Andreoiu, K. Auranen, M. P. Carpenter, W. N. Catford, C. M. Deibel, K. Hadyńska-Klęk, S. Hallam, D. E. M. Hoff, T. Huang, R. V. F. Janssens, S. Jazrawi, J. José, F. G. Kondev, T. Lauritsen, J. Li, A. M. Rogers, J. Saiz, G. Savard, S. Stolze, G. L. Wilson, and S. Zhu.

Search for nova presolar grains: γ-ray spectroscopy of ^{34}Ar and its relevance for the astrophysical ^{33}Cl(p,γ) reaction. *Phys. Rev. Lett.*, 124:252702, Jun 2020.

[25] C. Andreoiu, R.A.E. Austin, B. Bastin, D. Bazzacco, G. Benzoni, A. Boso, F. de Oliveira, A. Gadea, F. Garcia, A. Goasduff, J. Grebosz, K. Hadynska, G. Jaworski, Y. Jaganathen, P.R. John, S.M. Lenzi, J. Mabiala, T. Marchi, B. Melon, R. Menegazzo, D. Mengoni, A. Nannini, D. Napoli, C.M. Petrache, J.L. Pore, F. Recchia, M. Rocchini, E. Sahin, M. Siciliano, D. Testov, and J.J. Valiente-Dobon. Exploring excited states in 34^{Ar}. *LNL Annual Report 2015*, 242:31, 2015.

[26] Charles Kittel. *Introduction to Solid State Physics*. Wiley, 8 edition, 2004.

[27] Gerald Earle Jellison, Jr, S. Auluck, David J Singh, and Lynn A Boatner. Optical properties of bismuth germanate (bgo). *Journal of Applied Physics*, 701(1), 1 2010.

[28] Calin A Ur. Perspectives for the gamma-ray spectroscopy at lnl: the galileo project. *Journal of Physics: Conference Series*, 366(1):012044, 2012.

[29] F.H. Garcia. Photograph. *Private Communication*, 2 2018.

[30] A. Goasduff. Efficiency curve. *Private Communication*, 11 2018.

[31] D. Testov, D. Mengoni, Ciro Boiano, P. Cocconi, Philipp R. John, R. Isocrate, G. de Angelis, D. Bazzacco, A. Boso, F. Calaon, Alain Goasduff, L. Grassi, Katarzyna Hadyńska-Klęk, Grzegorz Jaworski, S. Lenzi, S. Lunardi, R. Menegazzo, D.R. Napoli, L. Ramina, F. Recchia, D. Rosso, M. Scarcioffolo, M. Siciliano, J.J. Valiente-Dobón, and P. Zatti. The first physical campaign of the euclides si-ball detector coupled to galileo gamma-ray spectrometer. *LNL Annual Report 2015*, 242:105, 2015.

[32] D. Testov, D. Mengoni, Alain Goasduff, A. Gadea, R. Isocrate, Philipp R. John, D. Bazzacco, Ciro Boiano, A. Boso, P. Cocconi, J.A. Dueñas, F.J. Egea, L. Grassi, Katarzyna Hadyńska-Klęk, Grzegorz Jaworski, S. Lunardi, R. Menegazzo, D. Napoli, and J. Valiente-Dobón. The 4π highly-efficient light-charged-particle detector euclides, installed at the galileo array for in-beam γ γ -ray spectroscopy. *The European Physical Journal A*, 55, 04 2019.

[33] Ö. Skeppstedt, H.A. Roth, L. Lindström, R. Wadsworth, I. Hibbert, N. Kelsall, D. Jenkins, H. Grawe, M. Górska, M. Moszyński, Z. Sujkowski, D. Wolski, M. Kapusta, M. Hellström, S. Kalogeropoulos, D. Oner, A. Johnson, J. Cederkäll, W. Klamra, J. Nyberg, M. Weiszflog, J. Kay, R. Griffiths, J. Garces Narro, C. Pearson, and J. Eberth. The euroball neutron wall – design and performance tests of neutron detectors. *Nuclear Instruments and Methods in Physics Research Section A: Accelerators, Spectrometers, Detectors and Associated Equipment*, 421(3):531 – 541, 1999.

[34] Alberto Lonardi. *The neutron wall detector coupled to GALILEO γ-ray array for the study of proton-rich nuclei.* PhD thesis, Universit‘a degli Studi di Padova, 2015.

[35] Rene Brun, Fons Rademakers, Philippe Canal, Axel Naumann, Olivier Couet, Lorenzo Moneta, Vassil Vassilev, Sergey Linev, Danilo Piparo, Gerardo GANIS, Bertrand Bellenot, Enrico Guiraud, Guilherme Amadio, wverkerke, Pere Mato, TimurP, Matevž Tadel, wlav, Enric Tejedor, Jakob Blomer, Andrei Gheata, Stephan Hageboeck, Stefan

Roiser, marsupial, Stefan Wunsch, Oksana Shadura, Anirudha Bose, CristinaCristescu, Xavier Valls, and Raphael Isemann. root-project/root: v6.18/02, August 2019.

[36] Alasdair Macleod. Redshift and energy conservation, 2004.

[37] James Ziegler, M.D. Ziegler, and J. Biersack. The stopping and range of ions in mater. *Nuclear Instruments and Methods in Physics Research Section B: Beam Interactions with Materials and Atoms*, 268:1818–1823, 06 2010.

[38] Ninel Nica and Balraj Singh. Nuclear data sheets for a = 34. *Nuclear Data Sheets*, 113(6):1563 – 1733, 2012.

[39] Christian Ouellet and Balraj Singh. Nuclear data sheets for a = 32. *Nuclear Data Sheets*, 112(9):2199 – 2355, 2011.

[40] M. Ionescu-Bujor, A. Iordachescu, D. R. Napoli, S. M. Lenzi, N. Mărginean, T. Otsuka, Y. Utsuno, R. V. Ribas, M. Axiotis, D. Bazzacco, A. M. Bizzeti-Sona, P. G. Bizzeti, F. Brandolini, D. Bucurescu, M. A. Cardona, G. de Angelis, M. De Poli, F. Della Vedova, E. Farnea, A. Gadea, D. Hojman, C. A. Kalfas, Th. Kröll, S. Lunardi, T. Martínez, P. Mason, P. Pavan, B. Quintana, C. Rossi Alvarez, C. A. Ur, R. Vlastou, and S. Zilio. High spin structure and intruder configurations in ^{31}P. *Phys. Rev. C*, 73:024310, Feb 2006.

[41] S. Aydin, M. Ionescu-Bujor, G. Tz. Gavrilov, B. I. Dimitrov, S. M. Lenzi, F. Recchia, D. Tonev, M. Bouhelal, F. Kavillioglu, P. Pavlov, D. Bazzacco, P. G. Bizzeti, A. M. Bizzeti-Sona, G. de Angelis, I. Deloncle, E. Farnea, A. Gadea, A. Gottardo, N. Goutev, F. Haas, T. Huyuk, H. Laftchiev, S. Lunardi, Tz. K. Marinov, D. Mengoni, R. Menegazzo, C. Michelagnoli, D. R. Napoli, P. Petkov, E. Sahin, P. P. Singh, E. A. Stefanova, C. A. Ur, J. J. Valiente-Dobón, and M. S. Yavahchova. High-spin states and lifetimes in ^{33}S and shell-model interpretation in the $sd-fp$ space. *Phys. Rev. C*, 96:024315, Aug 2017.

[42] Nicola Kelly. *Gamma-ray spectroscopy of neutron-deficient nuclei in the A < 120 mass region.* PhD thesis, University of the West of Scotland, 2019.

Appendix A

2 Sigma Limits to Establish Upper Limit on Reaction Cross Section

A.1 Establishing a Baseline Intensity

The purpose of establishing the 2σ limit is setting an upper limit for what is visible against the flat background. To do so, we pick a set of bins (energies) where we expect to see a peak/signal. We then fit that background by summing the counts within those bins. This process is highlighted as region A in Figure A.1. For the purposes of this analysis, we also fit an equal amount of bins around A on either the left side, L, or right side, R as shown in Figure A.1. The overall intensity is thus shown in Equation A.1.

$$N = A - \frac{R+L}{2} \tag{A.1}$$

A.2 Finding the Error

The error, σ_N, associated with the intensity N is given in Equation A.3

$$\sigma_N^2 = \left(\frac{\partial N}{\partial A}\right)^2 \sigma_A^2 + \left(\frac{\partial N}{\partial R}\right)^2 \sigma_R^2 + \left(\frac{\partial N}{\partial L}\right)^2 \sigma_L^2 \tag{A.2}$$

$$\sigma_N = \sqrt{\sigma_A^2 + \frac{\sigma_R^2 + \sigma_L^2}{4}} \tag{A.3}$$

The individual errors depend on the fitting function chosen. In the case of γ-ray spectroscopy, we expect our peaks to behave as Gaussians, and have errors $\sigma_a = \sqrt{a}$ where a is the number of counts within the fit area. We define the 2σ limit as $N + 2\sigma_N$, and the result is shown in Equation A.5.

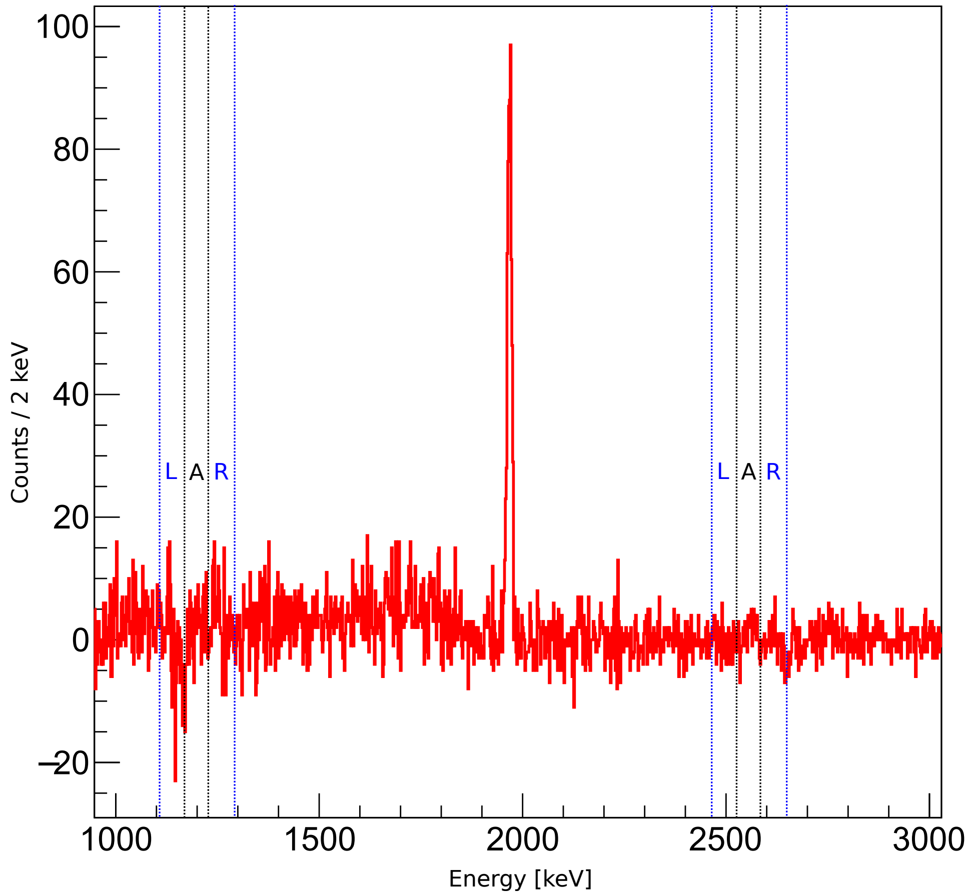

Figure A.1: A γ-ray spectrum with the regions, A, highlighted where we wish to evaluate the 2σ limit. To do so, the regions of equal energy width L and R on either side of A. For this particular γ-ray spectrum, the regions A correspond with transitions at 1198 keV and 2552 keV.

$$\sigma_N = \sqrt{A + \frac{R+L}{4}} \tag{A.4}$$

$$N + 2\sigma_N = A - \frac{R+L}{2} + 2\sqrt{A + \frac{R+L}{4}} \tag{A.5}$$

For reference, the same spectra shown in Figure A.1 with Gaussians drawn using a more stringent 3σ limit is shown in Figure A.2.

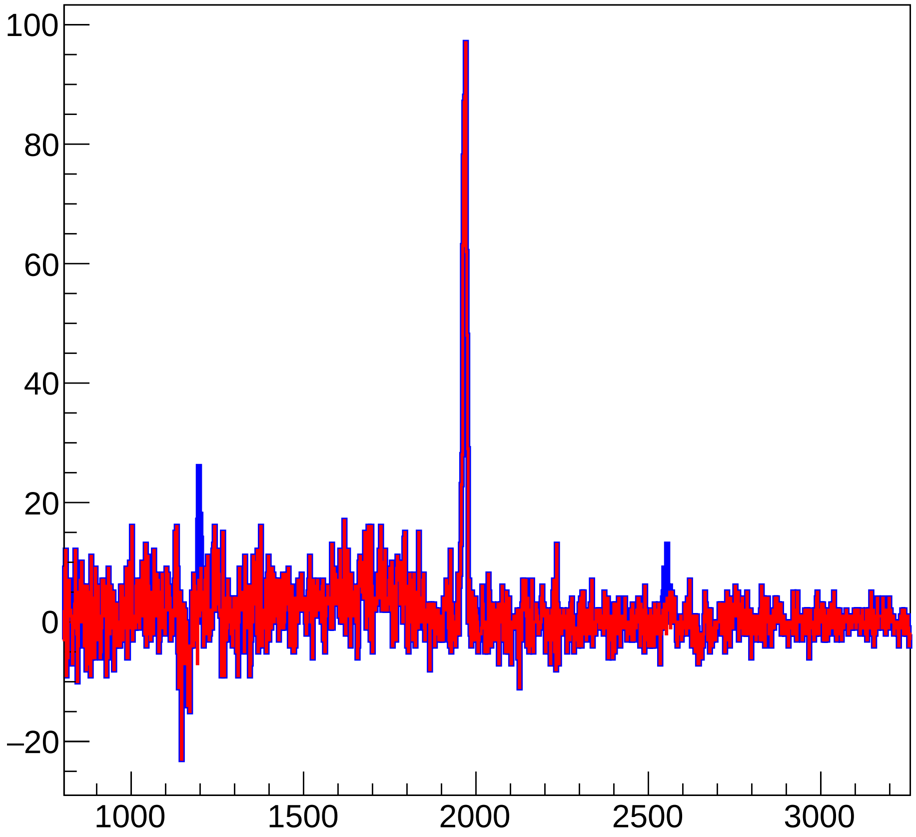

Figure A.2: Original γ-ray Spectrum and peaks with area corresponding to $N+3\sigma$ overlaid, which is more stringent than the 2σ limit. This serves to visualize what the γ-ray spectrum would look like if the transitions were observed with an intensity corresponding to the 3σ limit.

Appendix B

Contamination of Particle Gates

The topic of contamination was often discussed throughout this work, and quantification of the level of contamination was carried out using the particle gates: $2p, pn, 2pn$, and αp.

B.1 Notation

Discussions of contamination are usually conducted in the context of a contaminant peak within a reaction channel. For example, the ^{31}P nucleus is a major contaminant in the $2p$ reaction channel associated with ^{34}S, and talk of, "the nucleus ^{31}P in the $2p$ particle gate" will be brought up. To signify this, we can identify quantities like the number of γ-rays detected associated with the ^{31}P nuclei in the $2p$ particle gate will be presented as: $N_\gamma^{\alpha p:2p}$, where αp is the reaction channel associated with ^{31}P and $2p$ is the channel associated with ^{34}S. This adds visual clarity for cases like examining ^{34}S nuclei, associated with the $2p$ reaction channel, appearing in the correct $2p$ particle gate; the intensity of γ-rays detected associated with the ^{34}S nuclei detected in the $2p$ particle gate would be written as: $N_\gamma^{2p:2p}$. In addition, it is possible succinctly verbalize the latter quantity as, "the number of $2p$ in $2p$."

B.2 Quantifying Contamination Between Reaction Channels

The magnitude of contamination within a particle gate can be examined by comparing the number of contaminants, c, detected within $c : g$ against, $g : g$, the number of nuclei correctly associated with particle gate g:

$$C(c) = \sum_i \left(\frac{N_\gamma^{c:g}(E_i)}{\epsilon_\gamma(E_i)} \right) \Bigg/ \sum_j \left(\frac{N_\gamma^{g:g}(E_j)}{\epsilon_\gamma(E_j)} \right), \tag{B.1}$$

where we consider the number of counts for each γ-ray transition feeding the ground state of the nucleus, $N_\gamma(E_i)$, $\epsilon_\gamma(E_i)$ is the efficiency of GALILEO at the energy E_i, g identifies the reaction channel associated with the particle gate being applied, and c identifies the reaction channel associated with the contaminant nuclei. The ratio $C(c)$ should ideally be close to 0, and can serve as a quantification for how much contamination there is within the particle gate g. If the value of the ratio approaches 1, it can be interpreted as the contaminant and the nuclei of interest being found in comparable amounts within the particle gate g.

The ratio $C(c)$ is highlighted in Figure B.1 as a heatmap of $C(c)$ across different combination of reaction channels and contaminants. One way to interpret the heatmap is to compare numbers within the same column, to highlight the major contaminant for that channel. It should be noted that the numbers for the *pn* column are inflated due to difficulty fitting transitions feeding the 146-keV isomer state in ^{34}Cl, thus making the denominator smaller than in reality except for the case of $pn : pn$. Important highlights include the prevalence of the αp channel in contaminating the $2pn$ and especially the $2p$ particle gate, where ^{31}P associated with the αp channel was a major contaminant when analyzing ^{34}S. Other important notes of contamination include ^{33}S nuclei associated with the $2pn$ channel contaminating the *pn* particle gate when analyzing ^{34}Cl.

We can also examine contaminants relative to the contaminant's native particle gate as opposed to where it's found:

$$L(c) = \sum_i \left(\frac{N_\gamma^{c:g}(E_i)}{\epsilon_\gamma(E_i)} \right) \Bigg/ \sum_j \left(\frac{N_\gamma^{c:c}(E_j)}{\epsilon_\gamma(E_j)} \right) , \tag{B.2}$$

where everything is set up identically to Equation B.1, except for the denominator which is relative to the contaminant within its correct particle gate, rather than the particle gate the contaminant leaks into. The ratio $L(c)$ is also ideally 0, whereas a value close to 1 implies that the contaminant is found to leak to the particle gate g as often as it is found in the former's correct particle gate c. The ratio $L(c)$ can be thought of as a measure of how much the contaminant leaks into other particle gates.

The ratio $L(c)$ is visualized in Figure B.2. The rows show how much the contaminant appear in other reaction channels other than its own particle gate. The most striking of these would be the $2pn$ reaction channel associated with ^{33}S, which appear in other channels much more often than in its proper $2pn$ particle gate.

In summary, the reaction channel αp was a frequent and sizable contaminant in the $2p$ and $2pn$ particle gates as seen in Figure B.1, where ^{31}P transitions often obscured transitions of interest. When examining the ratio $L(c)$, the αp reaction channel was relatively well behaved, with the majority of transitions associated with ^{31}P staying within the αp particle gate. When looking at Table 5.9, ^{31}P was detected much more often than the other two major reaction channels highlighted. It is then likely that ^{31}P is a major contaminant mostly due to its high reaction cross section. Another major contaminant, the reaction channel $2pn$ associated with ^{33}S, had $C(c)$ ratios that were reasonable except for within the *pn* particle gate, where it was the most prominent contaminant. Upon examining $L(c)$ ratios, it is evident that ^{33}S was found more often in other particle gates than in its own $2pn$ particle gate. This also suggest that ^{33}S's role as a major contaminant is less to do with its reaction cross section and more to do with the failure of the $2pn$ particle gate in retaining most of the events associated with ^{33}S.

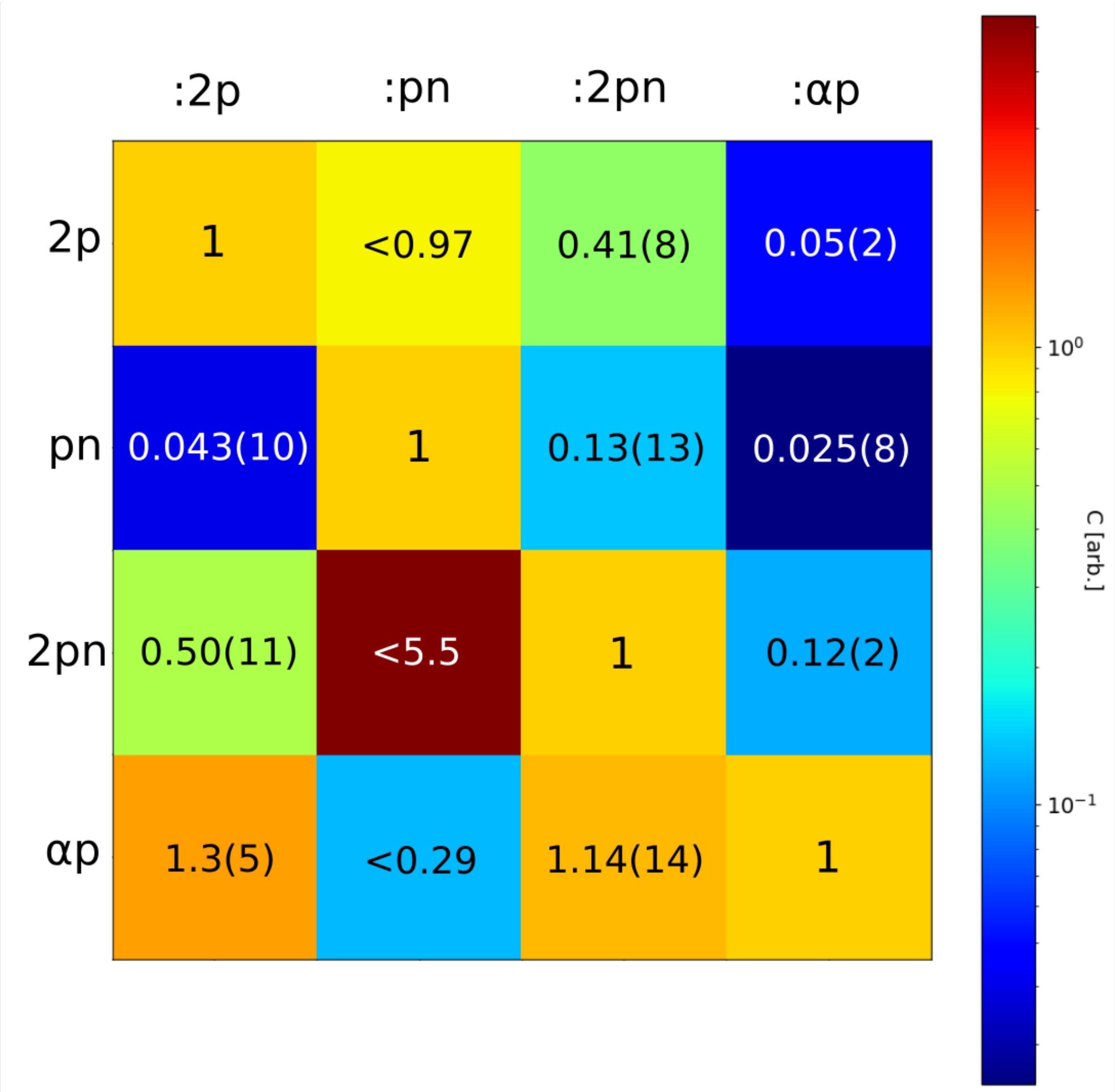

	:2p	:pn	:2pn	:αp
2p	1	<0.97	0.41(8)	0.05(2)
pn	0.043(10)	1	0.13(13)	0.025(8)
2pn	0.50(11)	<5.5	1	0.12(2)
αp	1.3(5)	<0.29	1.14(14)	1

Figure B.1: A heatmap is constructed based on the $C(c)$ ratios across four particle gates represented by the columns, and four nuclei/contaminants shown in each row. The diagonal values are 1 by definition. The pn column is artificially high compared with other columns as no transitions feeding the 146-keV isomer level in ^{34}Cl were fit due to difficulty. Notably, the prominence of αp as a contaminant is highlighted by values above 1 for the $2pn$ channel and the $2p$ channel, where it served to complicate analysis. The role of $2pn$ as a contaminant in the pn channel is also on display.

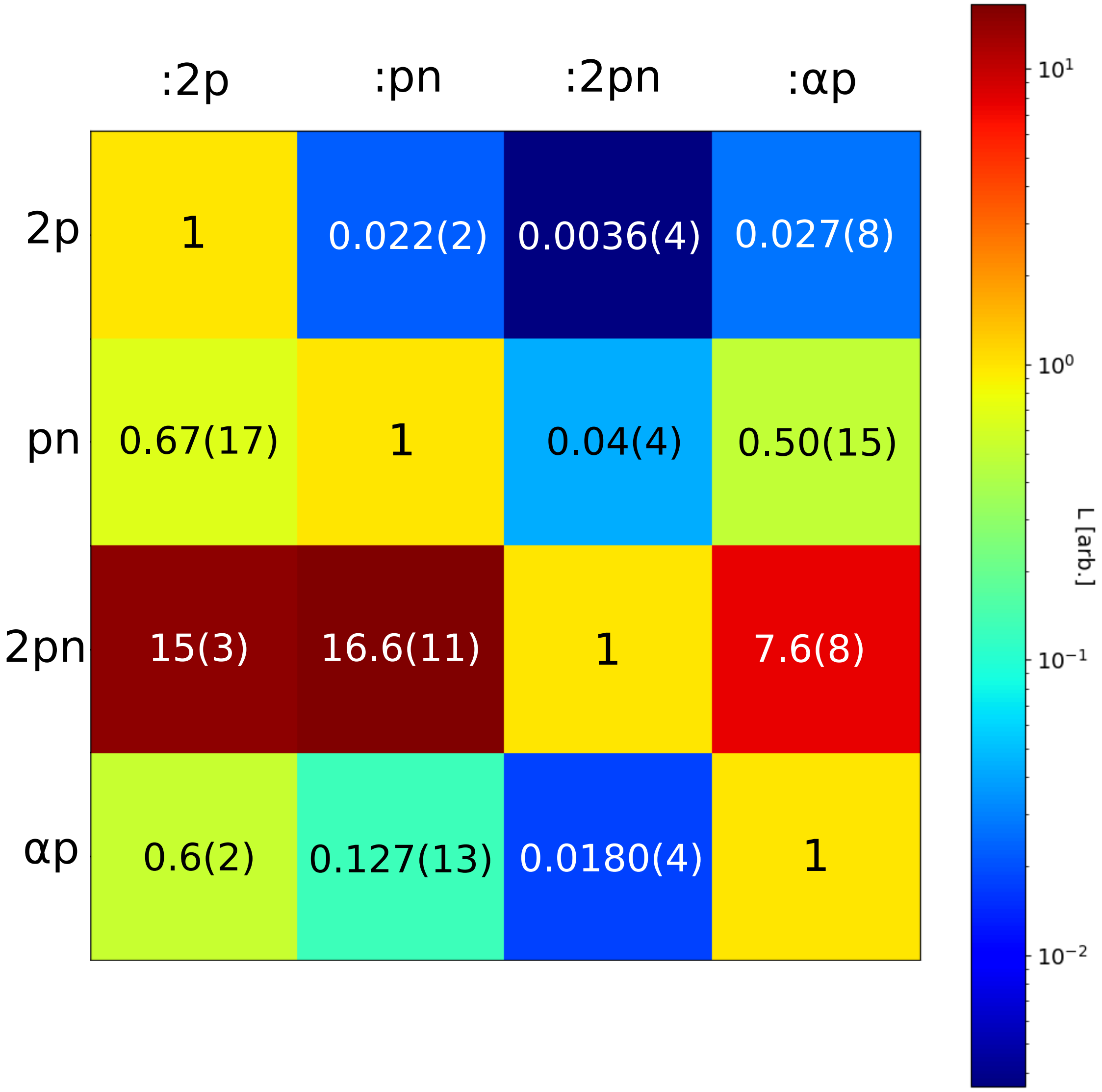

	:2p	:pn	:2pn	:αp
2p	1	0.022(2)	0.0036(4)	0.027(8)
pn	0.67(17)	1	0.04(4)	0.50(15)
2pn	15(3)	16.6(11)	1	7.6(8)
αp	0.6(2)	0.127(13)	0.0180(4)	1

Figure B.2: A heatmap is constructed based on the $L(c)$ ratios across four particle gates represented by the columns, and four nuclei/contaminants shown in each row. The diagonal values are 1 by definition. The 2pn row is very noticably large compared to other values of $L(c)$, highlighting the tendency of ^{33}S to appear in other particle gates rather than in its own $2pn$ gate.